



INSTITUTO DE FÍSICA
Universidade Federal Fluminense

Generalized Orbital Angular Momentum Symmetry in Parametric Amplification

Rafael Bellas Rodrigues

Niterói - RJ

9 de Março de 2022

Rafael Bellas Rodrigues

Generalized Orbital Angular Momentum Symmetry in Parametric Amplification

Tese apresentada à coordenação de Pós-Graduação de Física da Universidade Federal Fluminense como requisito parcial para a obtenção do Grau de Doutor em Física.

Universidade Federal Fluminense – UFF

Instituto de Física

Programa de Pós-Graduação

Supervisor: Prof. Dr. Antonio Zelaquett Khoury (IF-UFF)

Niterói - RJ

9 de Março de 2022

Ficha catalográfica automática - SDC/BIF
Gerada com informações fornecidas pelo autor

R696g Rodrigues, Rafael Bellas
Generalized Orbital Angular Momentum Symmetry in Parametric
Amplification / Rafael Bellas Rodrigues ; Antonio Zelaquett
Khoury, orientador. Niterói, 2022.
110 f. : il.

Tese (doutorado)-Universidade Federal Fluminense, Niterói,
2022.

DOI: <http://dx.doi.org/10.22409/PPGF.2022.d.13104549737>

1. Óptica Quântica. 2. Produção intelectual. I. Khoury,
Antonio Zelaquett, orientador. II. Universidade Federal
Fluminense. Instituto de Física. III. Título.

CDD -



INSTITUTO DE FÍSICA

Universidade Federal Fluminense

CURSO DE PÓS-GRADUAÇÃO EM FÍSICA

RUA GAL MILTON TAVARES DE SOUZA, SN

24210-346 – NITERÓI - RIO DE JANEIRO

TEL: (21)2629-5878 - FAX: 2629-5887

E-MAIL: cpg@if.uff.br

Ata dos trabalhos finais da Comissão Examinadora da tese de doutorado apresentada por **Rafael Bellas Rodrigues**. No nono dia do mês de março de dois mil e vinte e dois, às quatorze horas, reuniram-se de forma remota, os membros da Comissão Examinadora constituída pelos professores doutores Antonio Zelaquett Khoury (IF/UFF), Kaled Dechoum (IF/ UFF), Sandra Sampaio Vianna (UFPE), Stephen Patrick Walborn (U. Concepción) e Prof. Thiago Rodrigues de Oliveira (IF/UFF); sob a presidência do primeiro, para prova pública de apresentação de tese de doutorado intitulada "**Generalized Orbital Angular Momentum Symmetry in Parametric Amplification**", tendo em vista as exigências do Regulamento Específico do curso de Física relacionadas com a conclusão do Doutorado em Física pela Universidade Federal Fluminense. A tese foi elaborada sob a orientação do professor Antonio Zelaquett Khoury. Após a exposição do trabalho, o aluno respondeu às questões formuladas pelos integrantes da Comissão Examinadora, que apresentou parecer no sentido de aprová-lo. Para constar, foi lavrada a presente ata, que vai assinada pelos membros da Comissão Examinadora e pelo doutorando.

Niterói, nove de março de dois mil e vinte e dois.

Dr. Antonio Zelaquett Khoury

Dr. Kaled Dechoum

Dr.^a Sandra Sampaio Vianna

Dr. Stephen Patrick Walborn

Dr. Thiago Rodrigues de Oliveira

Rafael Bellas Rodrigues

Acknowledgements

Este trabalho foi escrito na língua inglesa, porém me parece mais natural escrever os agradecimentos em português. Não é fácil conseguir lembrar e agradecer a todos que me ajudaram nos últimos 4 anos, mas vou tentar. Gostaria de começar pelos meus colegas de laboratório e do instituto, que estavam ali "na luta" comigo todos os dias. O Wagner, Rafão, Braian, Magno e Arash.

O Wagner foi o primeiro a defender e sair para o pós-doutorado, mas ele sempre foi uma referência para mim desde a fase de iniciação científica. O Rafão, também conhecido como "voyeur" (não me pergunte o porquê), também foi um colega muito importante em minha formação. Tenho muita admiração e certeza que ele irá alçar grandes vôos na Física.

Sobre o Braian, Magno e Arash não tenho muito o que falar. Apenas dizer que se tornaram amigos que tenho certeza que levarei para a vida toda. Por sermos da mesma área, não tenho dúvidas que o Braian irá se tornar um Físico muito respeitado. Ao Magno e Arash ("Harum") desejo todo o sucesso para suas carreiras. Espero que consigam chegar onde almejam. Todos vocês podem contar comigo.

Gostaria de agradecer agora aos professores que foram muito importantes para a minha formação no doutorado. Meu orientador, o Prof. Zelaquett, e o Prof. Bié, mais novo professor do nosso laboratório. Bié, muito obrigado por toda sua ajuda e paciência comigo. Você foi muito importante na minha formação. Tenho certeza que você terá uma carreira brilhante como professor e pesquisador. Zela, muito obrigado por ter aceito ser o meu orientador. Você se tornou uma das maiores referências para a minha vida profissional. Mesmo após construir uma carreira sólida e respeitada mundo afora, você continua trabalhando com uma intensidade que impressiona qualquer um. Muito obrigado por toda sua dedicação e disponibilidade nesses últimos anos.

Durante a desgraçada pandemia da Covid-19, que nos levou pessoas muito amadas, iniciei, por outro lado, a experiência mais maravilhosa da minha vida. Me tornei o papai da Lizie. Escrever minha tese e cuidar de um neném recém-nascido foi um dos feitos mais difíceis que já realizei. Nesse momento, a pessoa mais importante, a qual sem ela não teria conseguido, foi a minha amada esposa,

Mariana. Meu amor, nada do que eu escrever aqui vai ser capaz de expressar a gratidão e amor que eu sinto por você. Apenas nós dois sabemos o que passamos. Ainda enfrentaremos muitos desafios na vida, mas a experiência que tivemos agora me dá certeza que venceremos todos. Muito obrigado por acreditar em mim e em nossa família. Te amo.

Por último, e não menos importante, quero agradecer a meus pais, Gustavo e Denise, e meu irmão mais velho, Mozart. O apoio de vocês desde o início da minha jornada na Física foi muito importante. Tenho muita sorte de ter nascido nesta família. Amo vocês. Nunca vou esquecer que há 10 anos cheguei para perguntar para o meu pai o que ele achava de eu começar a estudar Física. Sua reação foi a melhor possível e desde então ele sempre foi o que mais se preocupou com a minha formação. Pai, eu dedico esta tese a você.

Abstract

In this thesis we investigated interesting symmetry properties verified by the down-converted beams produced in optical parametric amplification with structured light. We show that the Poincaré sphere symmetry, previously demonstrated for first-order spatial modes, translates to a multiple Poincaré sphere structure for higher-orders. Each one of these multiple spheres is associated with a two-dimensional subspace defined by a different value of the orbital angular momentum (OAM). Therefore, the symmetry verified by first-order modes is reproduced independently in each subspace. It is also explored how the Poincaré sphere symmetry between signal and idler is affected by a pump beam carrying OAM. In this case, a Poincaré representation also applies to the pump beam and the symmetry between the down-converted modes becomes less intuitive. Those symmetry properties studied in this work can be useful for parallel control of independently correlated beams.

Keywords: Optical Parametric Oscillator - Orbital Angular Momentum - Non-linear optics.

Resumo

Nesta tese investigamos interessantes propriedades de simetria entre os feixes de luz estruturados produzidos em um processo de amplificação paramétrica ótica. Nós mostramos que tal simetria na esfera de Poincaré, já verificada para modos de primeira ordem, se evidencia também em múltiplas esferas para modos de ordem superior. Cada uma dessas esferas está associada a um subespaço de dimensão dois definido por valores opostos de momento angular orbital (MAO). Com isso, a simetria já verificada entre modos de primeira ordem é reproduzida independentemente em cada subespaço. Também exploramos como a simetria na esfera de Poincaré entre os feixes é alterada ao estruturarmos o bombeio com MAO. Neste caso, devemos também usar uma representação de esfera de Poincaré para o bombeio e a simetria entre os feixes de luz se torna menos intuitiva. As simetrias estudadas nesta tese podem ser úteis para o controle independente de feixes com correlações quânticas.

Palavras-chave: Optical Parametric Oscillator, Orbital Angular Momentum, Nonlinear optics.

List of Figures

Figure 1	– Twisted wavefront (left), intensity transverse profile (middle) and phase structure (right) of a beam with OAM of $l = +1$.	20
Figure 2	– Transverse structure of Gaussian mode (left) as well as its 3D structure (right).	23
Figure 3	– Travelling Gaussian beam in the z direction. At z_R we have the minimum radius of curvature. At z_1 the beam has a radius of $w(z_1)$ and its wavefront has a radius of curvature of $R(z_1)$.	23
Figure 4	– Different orders intensity profile of HG (a) and LG (b) modes. For HG modes $N = m + n$ and for LG modes $N = l + 2q$.	24
Figure 5	– Normalized modes superposition examples. The coefficients in the superposition is generated by Eq. (2.15).	25
Figure 6	– Analogy between the polarization sphere (a) and first-order OAM sphere (b). Any point on the sphere surface is defined by the spherical coordinates θ and ϕ .	26
Figure 7	– Third-order OAM spheres. $ l = 3$ and $q = 0$ on the poles (a). $ l = 1$ and $q = 1$ on the poles (b).	27
Figure 8	– Illustration of the basic working of a SLM. The reflected light phase structure can be arbitrary manipulated.	28
Figure 9	– Basic setup sketch to produce LG modes.	29
Figure 10	– Experimental setup of our SLM (Hamamatsu, model X10468-01).	29
Figure 11	– Illustration of an OAM beam passing through a tilted lens. In this example, the topological charge is $l = 1$, so we will have a first-order HG being produced ($n=2$ bright spots). θ_T is the tilt angle. The HG mode is observed in a distance D close to the focal length f of the lens.	30
Figure 12	– Input modes in the tilted lens (a) and its respectively outputs (b) near focal region.	30
Figure 13	– Optical parametric oscillator. A second-order nonlinear material $\chi^{(2)}$ is placed inside an optical cavity. The three waves involved in the nonlinear material is often called pump (ω_p), signal (ω_s) and idler (ω_i).	31
Figure 14	– Sum-Frequency Generation.	34
Figure 15	– Difference-Frequency Generation - OPA.	34

Figure 16 – Pictorial representation of phase mismatch vector $\Delta\vec{k}$ in sum-frequency generation process.	37
Figure 17 – I_3 as a function of the mismatch Δk	37
Figure 18 – Circles and ellipses on \vec{k} space. <i>a)</i> Uniaxial negative ($n_e < n_o$). <i>b)</i> Uniaxial positive ($n_e > n_o$). <i>c)</i> Biaxial.	41
Figure 19 – Pictorial representation of walk-off angle θ_w	42
Figure 20 – Type 2 phase-match on a KTP crystal in a parametric down-conversion process. For our KTP crystal, cut for type-II phase matching of 532 and 1064 nm, we have $\phi = 23.5^\circ$ and $\theta = 90^\circ$. In this sketch we are considering the extraordinary (e) wave to be horizontally polarized and the ordinary (o) wave vertically polarized.	43
Figure 21 – Examples of linear symmetrical configurations for optical cavities of length l and radius of curvature R . $C_{1,2}$ represents the curvature center of the mirrors.	44
Figure 22 – Stability diagram for g parameters. The blue shaded region indicates stable regimes.	44
Figure 23 – Fabry-Perot Resonator of length L . E_I , E_R , and E_T are, respectively, the incident, reflected, and transmitted electric field strength.	45
Figure 24 – Airy peaks of an optical resonator. Δ_ν is the FSR and δ_ν is the cavity linewidth. The resonance is achieved when ϕ is a multiple of 2π	46
Figure 25 – I_T versus ϕ for three distinct cavities finesse.	47
Figure 26 – Mode match in an optical cavity. The cavity length l , as well as the mirror’s radius of curvature R_1 and R_2 defines the beam waist for stable oscillation.	48
Figure 27 – In a confocal resonator (a), we can expect that a HG_{10} mode will resonate in the middle of the FSR of a Gaussian mode. On the other hand, in a concentric resonator (b), we might expect that a HG_{10} will resonate together with a Gaussian mode. . .	50
Figure 28 – Optical cavity of length L and lossy material α of length l . $E_{in}(t)$ is the input electric field and $E_p(t)$ is the electric field inside the cavity at point P	50
Figure 29 – Envelope $A(t)$ of an electric field $E(t)$	51

Figure 30 – Sketch of an OPO. α_{pin} is the input pump mode. α_j ($j = p, s, i$) are the three modes complex amplitudes inside the nonlinear $\chi^{(2)}$ material of length l . T_{1j} and T_{2j} are the mirrors transmission coefficients for each mode.	52
Figure 31 – OPO time evolution above-threshold. $\alpha_{pin} = 3$, $\gamma_p = \gamma = 1$, $\Delta_p = \Delta = 0$, $\chi = 1$ and $\eta_p = 1$. The threshold, therefore, is $ \alpha_{pin} _{th} = 1$. All parameters are in arbitrary units (a.u).	54
Figure 32 – Steady-state solutions intensities in OPO. $\gamma_p = \gamma = 1$, $\Delta_p = \Delta = 0$, $\chi = 1$ and $\eta_p = 1$. The threshold, therefore, is $ \alpha_{pin} _{th} = 1$. All parameters are in arbitrary units (a.u).	54
Figure 33 – OPA time evolution below-threshold. $\alpha_{pin} = 0.75$, $\alpha_{sin} = 0.20$, $\gamma_p = \gamma = 1.0$, $\Delta_p = \Delta = 0$, $\eta_p = \eta = 1.0$ and $\chi = 1.0$. The threshold is $ \alpha_{pin} _{th} = 1.0$	55
Figure 34 – Steady-state solutions intensities in OPA. $\alpha_{sin} = 0.10$, $\gamma_p = \gamma = 1.0$, $\Delta_p = \Delta = 0$, $\eta_p = \eta = 1.0$ and $\chi = 1.0$	56
Figure 35 – Transverse overlaps values at $z = 0$. In top we have both pump and signal modes at Gaussian ψ^{00} transverse structure and idler running over ψ^{0r} . At the bottom the pump is in a second-order LG mode ψ^{+20} and signal at ψ^{+10} first-order. The possible structures for the idler are ψ^{+1r}	58
Figure 36 – OPA time evolution below-threshold for both pump and injection at ψ^{00} . The OPA and cavities parameters are $\alpha_{pin}^{00} = 0.5$, $\alpha_{sin}^{00} = 0.3$, $\Lambda_{000}^{000} = 1$, $\Lambda_{001}^{000} = 0.5$, $\gamma_p = \gamma = 1$, $\Delta_p = \Delta = 0$, $\chi = 1$, $\eta_p = 1$. The threshold, therefore, is $ \alpha_{pin} _{th} = 1$	59
Figure 37 – OPA intensity evolution in steady-state for both pump and injection at ψ^{00} . The OPA and cavity parameters are $\alpha_{pin}^{00} = 0.1$, $\Lambda_{000}^{000} = 1$, $\Lambda_{001}^{000} = 0.5$, $\gamma_p = \gamma = 1$, $\Delta_p = \Delta = 0$, $\chi = 1$ and $\eta_p = 1$	59
Figure 38 – OPA time evolution below-threshold for pump at ψ^{+20} and injection at ψ^{+10} . The OPA and cavities parameters are $\alpha_{pin}^{+20} = 0.5$, $\alpha_{sin}^{+10} = 0.3$, $\Lambda_{000}^{211} = 1/\sqrt{2}$, $\Lambda_{001}^{211} = 1/4$, $\gamma_p = \gamma = 1$, $\Delta_p = \Delta = 0$, $\chi = 1$, $\eta_p = 1$. The threshold, therefore, is $ \alpha_{pin} _{th} = \sqrt{2}$	60
Figure 39 – OPA intensity evolution in steady-state for pump ψ^{+20} and injection at ψ^{+10} . The OPA and cavity parameters are $\alpha_{pin}^{00} = 0.1$, $\Lambda_{000}^{211} = 1/\sqrt{2}$, $\Lambda_{001}^{211} = 1/4$, $\gamma_p = \gamma = 1$, $\Delta_p = \Delta = 0$, $\chi = 1$ and $\eta_p = 1$	61

Figure 40 – Cavity resonance peak for a pump LG beam with extraordinary polarization (left) and ordinary polarization (right). In the ordinary wave the resonance peak splits in two, clearly showing the symmetry breaking between the two HG components of the LG beam. The OPO cavity parameters are $L_0 = 17.4$ mm, $l = 10.0$, mm. At 1064nm this peak separation is about 82 mrad.	62
Figure 41 – Sketch of a first-order LG mode with polarization at 45° passing through a KTP. With a PBS we can separate the ordinary (vertical) and extraordinary (horizontal) polarizations. The ordinary wave experience the astigmatism more crucial, while the effect can be neglected to the extraordinary wave.	63
Figure 42 – Sketch of the optical parametric oscillator with type-II phase-matching and structured light injection. \hat{e}_h and \hat{e}_v are the horizontal and vertical polarization unit vectors, respectively. The pump beam can be radially structured to optimize the spatial overlap with signal and idler.	65
Figure 43 – Example of a first-order injection beam. In this case we have set $A_{in}^{10} = 1$, $\theta = 45^\circ$ and $\phi = 90^\circ$	70
Figure 44 – Sketch of the optical parametric oscillator with type-II phase-matching and first-order structured light injection. \hat{e}_h and \hat{e}_v are the horizontal and vertical polarization unit vectors, respectively. The pump beam is a Gaussian mode.	71
Figure 45 – Poincaré sphere representation for first-order OAM symmetry.	72
Figure 46 – (a) Image shots of signal and idler beams along the equator. (b) Azimuthal angles measured from the mode inclination α with respect to the horizontal. The straight line shows the theoretical prediction. The standard deviations are smaller than 4° . The error bars are not visible within graphic precision.	73
Figure 47 – (a) Original (left) and mode-converted (right) image shots of signal and idler beams along the $\phi = 0$ meridian. (b) Inclinations angles α measured with respect to the horizontal HG mode. The straight line shows the theoretical prediction. The standard deviations are smaller than 4°	73
Figure 48 – Example of a second-order seed beam. In this case we have set $A_{in}^{01} = A_{in}^{20} = 1/\sqrt{2}$, $\theta = 45^\circ$ and $\phi = 90^\circ$	74

Figure 49 – Pump-signal-idler overlap integrals for $l = \pm 2$ (top) and $l = 0$ (bottom) as a function of the idler radial orders, when the pump parameters are fixed at $l_p = 0$ and $q_p = 1$	75
Figure 50 – Signal and idler symmetry in the Poincaré sphere for 2nd order OAM ($l = \pm 2$).	76
Figure 51 – Down-converted modes given the second-order injection in Fig.48. The coefficients were obtained from our numerical integration. The coordinate angles are $\theta^s = 0.78$ rad, $\theta^i = 2.36$ rad and $\phi^s = \phi^i = 1.57$ rad.	77
Figure 52 – Sketch of the optical parametric oscillator with type-II phase-matching and second-order structured light injection. \hat{e}_h and \hat{e}_v are the horizontal and vertical polarization unit vectors, respectively. The pump is radially structured ($l = 0, q = 1$) to optimize the spatial overlap with signal and idler.	77
Figure 53 – Pump-signal-idler spatial overlap for $l = \pm 3$ (top) and $l = \pm 1$ (bottom) as a function of the idler radial orders, when the pump parameters are fixed at $l_p = 0$ and $q_p = 2$	78
Figure 54 – Example of a third-order seed beam with $A_{in}^{11} = A_{in}^{30} = 1/\sqrt{2}$. The coordinates on the Poincaré spheres for $l = \pm 3$ and $l = \pm 1$ are $(\theta_3 = 45^\circ, \phi_3 = 0^\circ)$ and $(\theta_1 = 60^\circ, \phi_1 = 90^\circ)$, respectively.	79
Figure 55 – Third-order OAM symmetry. On left side we can visualize the symmetry relation verified in the Poincaré sphere for $l = \pm 3$ and on the right side the same symmetry is displayed on the independent sphere for $l = \pm 1$	80
Figure 56 – Down-converted modes given the third-order injection in Fig.54. The coefficients were obtained from our numerical integration. The coordinate angles in the Poincaré sphere for $l = \pm 3$ are $\theta_3^s = 0.78$ rad, $\theta_3^i = 2.35$ rad and $\phi_3^s = \phi_3^i = 0$ rad. In the Poincaré sphere for $l = \pm 1$ we have $\theta_1^s = 1.04$ rad, $\theta_1^i = 2.09$ rad and $\phi_1^s = \phi_1^i = 1.57$ rad.	81
Figure 57 – Poincaré sphere representations of the pump ($l = \pm 2$) and seed ($l = \pm 1$) beams.	82
Figure 58 – Poincaré sphere representation of the intracavity signal and idler structures when $\theta_p = \pi/2$ and $\phi_p = 0$	84

- Figure 59 – Sketch of the optical parametric oscillator with type-II phase-matching, first-order structured light injection and second-order balanced pump ($\theta_p = \pi/2$ and $\phi_p = 0.$). \hat{e}_h and \hat{e}_v are the horizontal and vertical polarization unit vectors. 84
- Figure 60 – Symmetry for the numerical simulation of the OPO dynamics under first-order injection (Fig.43). The spherical coordinates for $l = \pm 1$ are $\theta_1 = 0.7854$ rad and $\phi_1 = 1.571$ rad. The pump, seed and decay parameters were set to $\beta_{pin} = 1$, $A_{in}^{10} = 1$ and $\gamma_r = 1$, respectively. The free-running oscillation threshold is $\beta_{pth} \approx 2.0$ 86
- Figure 61 – Symmetry for the numerical simulation of the OPO dynamics under second-order injection (Fig.48). The spherical coordinates for $l = \pm 2$ are $\theta_2 = 0.7854$ rad and $\phi_2 = 1.571$ rad. The pump, seed and decay parameters were set to $\beta_{pin} = 0.75$, $A_{in}^{20} = 1/\sqrt{2}$ and $\gamma_r = 1$, respectively. The free-running oscillation threshold is $\beta_{pth} \approx 2.0$ 87
- Figure 62 – Two-sphere symmetry for the numerical simulation of the OPO dynamics under third-order injection (Fig.54). The spherical coordinates for $l = \pm 3$ are $\theta_3 = 0.7343$ rad and $\phi_3 = 0$. For $l = \pm 1$ the coordinates are $\theta_1 = 1.042$ rad and $\phi_1 = 1.571$ rad. The pump, seed and decay parameters were set to $\beta_{pin} = 1$, $A_{in}^{30} = A_{in}^{11} = 1/\sqrt{2}$ and $\gamma_r = 1$, respectively. The free-running oscillation threshold is $\beta_{pth} \approx 2.7$ 88
- Figure 63 – Symmetry for the numerical simulation of the OPO dynamics under first-order injection (Fig.43) and second-order balanced pump ($\theta_p = 90^\circ$ and $\phi_p = 0^\circ$). The spherical coordinates for $l = \pm 1$ are $\theta_1 = 0.7859$ rad, $\theta'_1 = 0.8019$ rad and $\phi_1 = 1.571$ rad. The pump, seed and decay parameters were set to $\beta_{pin}^+ = \beta_{pin}^- = 0.707$, $A_{in}^{10} = 1$ and $\gamma_r = 1$, respectively. The free-running oscillation threshold is $\beta_{pth} \approx 5.7$ 89

Figure 64 – Symmetry for the numerical simulation of the OPO dynamics under first-order injection (Fig.43) and second-order pump ($\theta_p = 45^\circ$ and $\phi_p = 90^\circ$). The spherical coordinates for $l = \pm 1$ are $\theta_1 = 1.549$ rad, $\theta'_1 = 0.7706$ rad, $\phi_1 = 0$ rad and $\phi'_1 = 1.571$ rad. The pump, seed and decay parameters were set to $\beta_{pin}^+ = 0.924$, $\beta_{pin}^- = 0.383i$, $A_{in}^{10} = 1$ and $\gamma_r = 1$, respectively. The free-running oscillation threshold is $\beta_{pth} \approx 5.7$	90
Figure 65 – Basic experimental setup built at LOQ-UFF to investigate OAM symmetry.	91
Figure 66 – Semi monolithic OPO. The input face of the crystal is coated to act as the OPO input coupler (HR at 1064 nm and $R = 92\%$ at 532 nm). The concave mirror (HR at 532 nm and $R = 95\%$ at 1064 nm) is mounted on a PZT.	93
Figure 67 – OPA process for Gaussian modes using one crystal. At the top, we have the Airy peaks for the injected mode (Blue) which will be amplified at signal mode. Once we match the resonance peaks, by controlling crystal temperature, for pump (Yellow), signal (Blue) and the stimulated idler (Purple) we have OPA process (bottom).	94
Figure 68 – Two crystals semi monolithic OPO. Same coatings as the previous setup in Fig.66 for the "KTP 1" and output mirror. The "KTP 2" is coated AR for both wavelengths, as well as the HWP.	95
Figure 69 – Two crystals OPO configuration for astigmatism correction for first-order LG mode ψ^{+10} injection. On the right side, we have the ordinary polarization which will be occupied by the stimulated idler mode. This last one can have its astigmatism corrected by placing a second rotated crystal (right bottom part). The signal mode, at extraordinary polarization, will not suffer any optical aberration, as illustrated on the left side of both configurations.	96
Figure 70 – Pictorial representation of walk-off angle θ_w	99
Figure 71 – The value ϕ_L represents how "far" the mode is in relation to the resonance.	101
Figure 72 – Knife-method apparatus (left) and experimental result of it (right).	103

Contents

1	INTRODUCTION	15
2	ORBITAL ANGULAR MOMENTUM OF LIGHT	20
2.1	Paraxial Equation	21
2.1.1	Gaussian Mode	22
2.1.2	Hermite-Gauss and Laguerre-Gauss Modes	23
2.1.3	Poincaré Sphere for Spatial Modes	25
2.2	Production and Measurement of OAM beams	27
3	OPTICAL PARAMETRIC OSCILLATOR	31
3.1	Introduction to Nonlinear Optics	32
3.1.1	Nonlinear Susceptibility	32
3.1.2	3 Wave Mixing Equations and Phase-Matching	34
3.2	Propagation of Light in Crystals	38
3.2.1	KTP Crystal	42
3.3	Optical Resonators	43
3.3.1	Fabry-Perot Resonator	45
3.3.2	Transverse Modes in Optical Resonators	47
3.3.3	Dynamical Equation in a Resonator	50
3.4	OPO Dynamical Equations	51
3.4.1	OPA Dynamical Equations	55
3.4.2	Dynamical Equations for Transverse Modes	56
3.4.3	Astigmatism effect in the OPO	61
4	GENERALIZED OAM SYMMETRY IN PARAMETRIC AMPLIFICATION	64
4.1	Structured Light Injection in Parametric Amplification	64
4.1.1	Dynamical Equations and Steady State Solution	66
4.2	Generalized Poincaré Symmetry	68
4.2.1	Symmetry for First-Order Seed	70
4.2.2	Symmetry for Second-Order Seed	74
4.2.3	Symmetry for Third-Order Seed: Two-Spheres	77
4.2.4	Symmetry for OAM-Structured Pump	81

4.3	Numerical Simulations Results	85
4.4	Experimental Proposal	90
5	CLOSING REMARKS	97
	APPENDIX A – WALK-OFF ANGLE	98
	APPENDIX B – TRANSMITTED INTENSITY AND FI- NESSE	100
	APPENDIX C – BEAM WAIST CHARACTERIZATION .	102
	APPENDIX D – DYNAMICAL EQUATIONS - RESONATOR AND OPO	104
	BIBLIOGRAPHY	106

1 Introduction

The laser as a device is undoubtedly one of the greatest contributions to the branches of nonlinear optics and quantum optics. Its development by Maiman et al. in 1960 [1] allowed for the first time the second-harmonic generation in quartz crystal [2]. The second-harmonic generation is essentially a second-order nonlinear phenomenon in which the nonlinearity of the material is capable to produce new frequencies components not present in the input laser beam. More precisely, given an input laser beam of frequency ω in a quartz crystal this last respond nonlinearly to the applied electric field and generate a laser beam with frequency of 2ω . Second-order nonlinear¹ materials allow the so-called three-wave mixing processes.

A very important three-wave mixing nonlinear phenomenon is the spontaneous parametric down-conversion (SPDC), which was first predicted in 1961 [3] but only observed in 1970 [4]. Classically, the SPDC consists of a process where a wave of frequency ω_p (pump) converts into two smaller frequencies waves with frequencies ω_s (signal) and ω_i (idler). In the quantum mechanical framework the SPDC can be understood as the higher energy $\hbar\omega_p$ pump photon is absorbed and a pair of photons, signal and idler, with lower energies $\hbar\omega_s$ and $\hbar\omega_i$ are emitted. In this process we have energy conservation ($\hbar\omega_p = \hbar\omega_s + \hbar\omega_i$).

The pair of photons produced in the SPDC is often the object of study of quantum correlations, such as entanglement [5]. Generally, the low efficiency of the nonlinear process can be overcome by placing the nonlinear material inside an optical resonator. The purpose of the resonator is to build up large field intensities and allow experimentalists to study SPDC, for example, in the continuous regime. This gave rise to a very important device in optics: the optical parametric oscillator (OPO). The first OPO was experimentally realized by J. A. Giordmaine and Robert C. Miller [6] just five years after the first laser, in 1965.

In the last few decades, the OPO has been widely used in quantum optics experiments. The optical parametric amplification (OPA), which can be understood as the OPO operation below threshold, is a powerful tool for generating quantum correlations between independent light beams [7, 8, 9]. It has been

¹ There are higher-order nonlinear materials where other frequency components can be produced.

used as an important resource for many quantum applications such as quantum teleportation and quantum metrology [10, 11]. The longitudinal mode structure of quantum correlated beams generated by an optical parametric oscillator gives rise to a frequency comb of quadrature entangled beams that are good candidates to scalable quantum computers [12, 13].

A very interesting physics branch rises when we explore how structured light beams are coupled in the parametric process. Orbital angular momentum (OAM) conservation has been investigated in cavity-free spontaneous [14] and stimulated parametric down-conversion [15, 16]. The nonlinear coupling between different transverse modes is subject to conditions imposed by the spatial overlap between them, giving rise to selection rules that limit the modes allowed in the interaction [17, 18, 19, 20]. When the process is intensified in an OPO, cavity conditions also dictate which modes can survive the loss-gain balance, which can affect both the transverse [21, 22, 23] and longitudinal [24] mode structure.

We briefly mention a few applications of the OPO to illustrate how versatile this device is. In this thesis, the OPO is the basis for the development of our theory [25] and, therefore, our contribution to the literature. In this present work, we investigated interesting symmetry properties verified by the down-converted beams produced in an OPA process with structured light. This theory can be understood as the generalization of the symmetry demonstrated experimentally [26] and theoretically proposed [27] for first-order modes. In the following paragraphs, the thesis structure is going to be presented.

In chapter 2, the OAM [28, 29] of light will be the most relevant topic. We are going to begin our discussion by introducing the basic features of an OAM laser beam, such as its twisted wavefront due to a phase term $e^{il\phi}$ on the electric field structure. l is known as the topological charge, which represent the amount of OAM in a light beam and ϕ is a azimuthal coordinate perpendicular to the propagation direction. Light carrying OAM is described in terms of the Laguerre-Gauss (LG) modes, which are the solution of the well known paraxial equation [30] in cylindrical coordinate. Also, we are going to talk about the Hermite-Gauss (HG) modes. This last is also the solution of the paraxial equation but in cartesian coordinates. Both LG and HG modes form a base [31] in such a way that we can write LG modes in terms of HG modes (both on same order).

Also in chapter 2, we are going to discuss a very important geometrical representation of OAM modes. This representation is equivalent to the famous

Poincaré sphere [32] to represent polarization states of light, but for OAM modes [33]. This geometrical representation for superior order modes is very important to understand our theory. Next, we are going to briefly describe a very important device used to produce OAM modes, the spatial light modulator (SLM) [34]. To end chapter 2, we are going to talk about a very simple and powerful method to measure the topological charge l of a OAM mode. This method [35] is simple because only demands the most common instrument present in every optical lab, a spherical lens.

In chapter 3, our goal is to reunite the knowledge necessary to understand the OPO in the classical regime. As we already mention the OPO is a device constituted of a nonlinear material inside an optical cavity. Our discussion, therefore, will begin by revising the basics of nonlinear optics [36, 37]. We will talk about the nonlinear susceptibility and the principal phenomena related to it, such as sum and difference frequency generation. This last represents the OPA process, as we will discuss. Next, we are going to discuss the three wave mixing equations, which couples the modes pump, signal, and idler in a second-order nonlinear material. A very important term present in the three wave mixing equations is the phase-mismatching Δk . When $\Delta k = 0$ we have linear momentum conservation which is crucial to maximize the nonlinear process.

The next topic in chapter 3 will be the propagation of light in crystals [38, 37]. In general, such materials exhibit anisotropic, or birefringent, behavior. Physically, this means that the polarization in such media is not just a scalar constant times the applied electric field. The dependence of \vec{P} on \vec{E} is expressible as a tensor relation. As we are going to see, for a given direction of propagation we have two distinct phase velocities. Each velocity is associate with distinct polarizations often called *ordinary* and *extraordinary* polarizations. This last experience the *walk-off* effect, which consists of an effect that causes the wave vector not to be parallel to the Poynting vector anymore. Next, we are going to present basic features of the second-order nonlinear crystal used in this thesis theory: the KTP (Potassium titanyl phosphate) crystal.

The last topic in chapter 3 is the optical resonators. One of the purposes to use an optical resonator is to build up large field intensities in its interior given a moderated power input [39]. To explore nonlinear effects, we should have a large amount of intensity in the nonlinear medium [36]. We are going to use as a model the Fabry-Perot plane-parallel cavity to study basic features of optical

resonators [37, 40, 41], such as the cavity resonance peaks, free spectral range, cavity linewidth, and cavity finesse. Then we are going to talk about transverse modes in a resonator and the dynamics of a mode inside such resonator.

After discussing the last topics we can derive and discuss the OPO dynamical equations [23, 37, 41]. We are going to discuss very important concepts, such as the oscillation threshold. This last is basically the minimum pump intensity necessary to produce signal and idler. As we will see, in this regime the pump power is "clipped", which means, above the threshold is always the same. The numerical integration of the OPO time evolution equations, as well as the modes intensities evolution in steady-state will be discussed. Next, we are going to make a similar discussion but with an OPA, which is basically considered an injection seed mode in the OPO. In this case, we don't have an oscillation threshold, as we can notice from our numerical simulations.

At the end of chapter 3, we are going to present the OPO (and OPA) dynamical equations with structured light. In this case, we have to consider a very important term in the dynamical equations: the transverse overlap. This term is a three mode integral on the transverse plane which imposes important selection rules in the parametric process [23, 42, 43], such as the OAM conservation. This term, therefore, dictates the allowed transverse modes that can exist in the parametric process in a hierarchical way depending on the overlap value. To illustrate such hierarchy we are going to present a few examples of the time evolution of particular configurations with different overlaps values. Also, we are going to give a brief explanation of the astigmatism effect [42] that occurs in KTP crystals.

Finally, in chapter 4, we are going to explain in details the novelty that this thesis brings to the literature [25]. We investigated how the Poincaré sphere symmetry [26, 27] extends to higher-order modes. In principle, this subject suggests a difficult task, since higher-order modes do not have a simple geometric representation. However, the selection rules that arise from the spatial overlap between the interacting modes impose restrictions that limit the symmetry properties to two-dimensional subspaces of the higher-order mode structure. The Poincaré symmetry is independently verified inside each subspace, what can be useful for parallel control of independent down-conversion channels.

We will start the discussion by talking about structured light injection in parametric amplification. The following topic will be to present the dynamical

equations and steady-state solutions with superior order structures. We will revise the symmetry for first-order modes and then explore it for second and third-order seed modes. For second-order modes no special symmetry is realized since we have a zero OAM subspace defined by $l = 0$. The simplest case with more than one Poincaré sphere is realized by a third-order seed beam. Those spheres are defined by two independent subspaces of OAM values $l = \pm 3$ and $l = \pm 1$.

Once we introduced the OAM symmetry for second and third-order modes the generalization for superior orders is analogous. For an even order N injection we will have $N/2$ independent spheres where the OAM symmetry occurs. While for odd modes of order N we will have $(N + 1)/2$ independent spheres where we can verify the aforementioned symmetry. We also studied the symmetry between signal and idler when we structure the pump beam with OAM. As we will see the symmetries properties get even less intuitive. All of our numerical simulations solutions of the OPO equations are in very good agreement with the analytical predictions. We also presented an experimental setup that is already being built at our lab to explore the generalized OAM symmetry.

2 Orbital Angular Momentum of Light

It is well known that a lightwave can carry both spin angular momentum (SAM) and orbital angular momentum (OAM) [28]. Opposite to the SAM of $\pm\hbar$ per photon due to the circularly polarized light, OAM can be interpreted to characterize the “twist” of a helical phase front [44], according to Fig. 1. Physically, OAM beams have an annular ring intensity profile with an optical vortex at the beam center as illustrated in Fig. 1. This can be understood as a consequence of a phase term of the form $e^{il\phi}$ in the electric field structure, where l is known as the topological charge and is related to the amount of angular momentum and the number of intertwined helices per wavelength. ϕ is the azimuthal coordinate perpendicular to the propagation axis. The study of OAM of light is in the branch of optics known as *structured light* which has application in different areas such as optical communication [29] and optical tweezers [45].

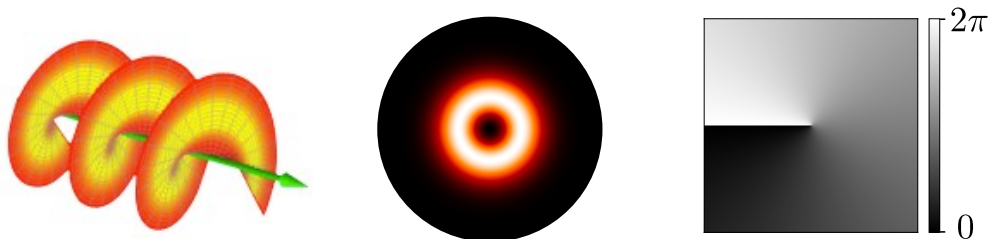


Figure 1 – Twisted wavefront (left), intensity transverse profile (middle) and phase structure (right) of a beam with OAM of $l = +1$.

In this chapter, we are going to talk about different transverse structures of light derived from the solutions of the paraxial equation in cartesian and cylindrical coordinate systems [27, 30]. Those solutions are called the Hermite-Gauss (HG) and Laguerre-Gauss (LG) modes. This last one describes light with OAM. We will also discuss how LG modes can be conveniently represented in a sphere analogous to the famous Poincaré sphere of light polarization [33]. This representation is very important to understand the symmetry we want to explore in the theory developed in this thesis. We are going to discuss how we can produce OAM beams using a device called spatial light modulator (SLM) [46] and how we can also measure the topological charge l of a light beam using a simple spherical lens [35].

2.1 Paraxial Equation

Let's begin by writing the wave equation for the electric field obtained from Maxwell's equations in free space:

$$\nabla^2 \vec{E} - \frac{1}{c^2} \frac{\partial^2 \vec{E}}{\partial t^2} = 0, \quad (2.1)$$

where c is the speed of the light wave in vacuum. Assuming solutions of the form $\vec{E}(\vec{r}, t) = \hat{e} f(\vec{r}) e^{-i\omega t}$, where \hat{e} is the polarization direction, $e^{-i\omega t}$ is the time dependence phase term and $f(\vec{r})$ is a spatial dependent amplitude term which gives rise to the Helmholtz equation

$$\nabla^2 f(\vec{r}) + k^2 f(\vec{r}) = 0, \quad (2.2)$$

where $k = \omega/c$ is the wavenumber in vacuum. The Helmholtz Equation (2.2) can be understood as a time-independent form of the wave equation (2.1). Its solution

$$f(\vec{r}) = \psi(\vec{r}) e^{i\vec{k} \cdot \vec{r}} \quad (2.3)$$

contains the propagation phase term $e^{i\vec{k} \cdot \vec{r}}$ and the spatial envelope term $\psi(\vec{r})$ on the transverse direction.

When working with laser beams we have to consider low divergence angle in relation to the propagation axis. Given this consideration we can obtain from substitution of Equation (2.3) in (2.2) [30]:

$$\nabla^2 \psi + 2ik \frac{\partial \psi}{\partial z} = 0. \quad (2.4)$$

We can conveniently rewrite the Laplacian as $\nabla^2 \psi = \nabla_{\perp}^2 \psi + \frac{\partial^2 \psi}{\partial z^2}$ and rewrite (2.4) as

$$\nabla_{\perp}^2 \psi + \frac{\partial^2 \psi}{\partial z^2} + 2ik \frac{\partial \psi}{\partial z} = 0. \quad (2.5)$$

where we separate the transverse second derivative in the (x, y) plane from the longitudinal direction z . At this point we can make use of the paraxial approximation which is related to slow variation of ψ along the propagation axis:

$$\left| \frac{\partial^2 \psi}{\partial z^2} \right| \ll \left| \frac{\partial^2 \psi}{\partial x^2} \right|, \left| \frac{\partial^2 \psi}{\partial y^2} \right|, 2k \left| \frac{\partial \psi}{\partial z} \right|. \quad (2.6)$$

Given these considerations we can neglect the term $\frac{\partial^2 \psi}{\partial z^2}$ and write the paraxial equation:

$$\nabla_{\perp}^2 \psi + 2ik \frac{\partial \psi}{\partial z} = 0. \quad (2.7)$$

On the following sections, we can are going to discuss the solutions of the paraxial equation in cartesian and cylindrical coordinates. The lowest order solution is base independent and give rises to the Gaussian mode, which we will begin the discussion.

2.1.1 Gaussian Mode

Firstly, let's begin by discussing the most simple solution for the paraxial equation, the Gaussian mode [47]. The Gaussian mode is present in most transverse structure (Fig. 2) of commercial lasers. The normalized Gaussian solution $\psi^{00}(x, y, z)$ propagating in the z direction will be written in cartesian coordinate as [30]

$$\psi^{00}(x, y, z) = \sqrt{\frac{2}{\pi}} \frac{1}{w(z)} \exp \left[\frac{-(x^2 + y^2)}{w^2(z)} + ik \frac{(x^2 + y^2)}{2R(z)} - i \arctan \left(\frac{z}{z_R} \right) \right], \quad (2.8)$$

where $R(z)$ is the radius of curvature of the phase front at a given position z along the propagation axis. The term $\arctan(z/z_R)$ on the right-hand side of (2.8) is called the Gouy phase of the Gaussian mode. $w(z)$ is the beam ratio in a given z position. $R(z)$ and $w(z)$ are, respectively, given by

$$R(z) = z \left[1 + \left(\frac{z_R}{z} \right)^2 \right], \quad (2.9)$$

$$w(z) = w_0 \sqrt{1 + \left(\frac{z}{z_R} \right)^2}, \quad (2.10)$$

where $z_R = \pi\omega_0^2/\lambda$ is called the Rayleigh length and determine the position where the beam radius of curvature has its minimum value. ω_0 in Equation (2.10) determines the minimum width of the beam and is called the beam waist. The parameters that characterize the Gaussian beam is illustrated in Fig. 3. As we are going to see in the next chapter the parameters in Equations (2.9), (2.10) and (2.12) are very important in order to have a stable transverse mode oscillating inside an optical resonator.

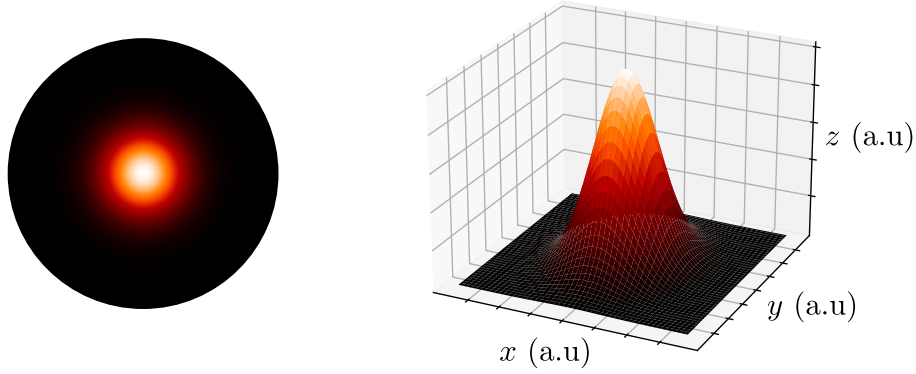


Figure 2 – Transverse structure of Gaussian mode (left) as well as its 3D structure (right).

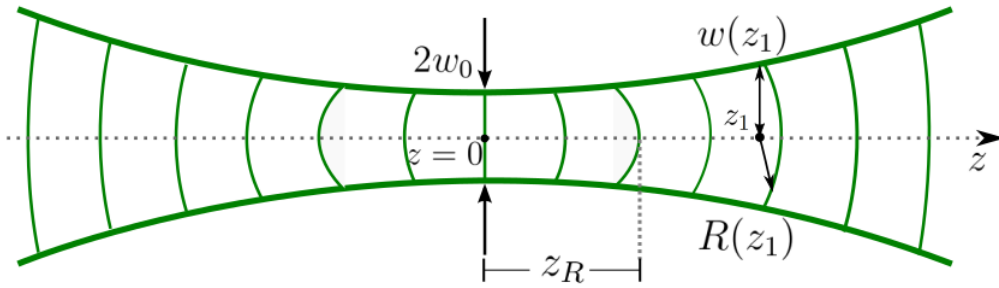


Figure 3 – Travelling Gaussian beam in the z direction. At z_R we have the minimum radius of curvature. At z_1 the beam has a radius of $w(z_1)$ and its wavefront has a radius of curvature of $R(z_1)$.

2.1.2 Hermite-Gauss and Laguerre-Gauss Modes

The most general solution of the paraxial equation in cartesian coordinate is called the Hermite-Gauss (HG) mode and is mathematically described by ψ_{HG}^{nm} [43]:

$$\psi_{HG}^{nm}(x, y, z) = \sqrt{\frac{2}{\pi n! m!}} \frac{2^{-\frac{(n+m)}{2}}}{w(z)} H_n \left(\sqrt{2} \frac{x}{w(z)} \right) H_m \left(\sqrt{2} \frac{y}{w(z)} \right) \times \exp \left[-\frac{x^2 + y^2}{w^2(z)} + ik \frac{x^2 + y^2}{2R(z)} - i\Phi^{mn}(z) \right], \quad (2.11)$$

The indices m, n determines the order $N = m + n$ of the HG mode. We can see that its amplitudes are modulated by Hermite polynomials H_n and H_m on the transverse directions x and y , respectively. The term $\Phi^{mn}(z)$ is the longitudinal Gouy phase of the HG mode:

$$\Phi^{nm}(z) = (m + n + 1) \arctan \left(\frac{z}{z_R} \right). \quad (2.12)$$

For the general solution of (2.7) in cylindrical coordinates, we have the Laguerre-Gauss (LG) modes. That solution originates from the light beams carrying OAM and is written as [30]

$$\psi_{LG}^{lq}(\rho, \phi, z) = \sqrt{\frac{2q!}{\pi(q+|l|)!}} \frac{\sqrt{2}\rho^{|l|}}{w(z)^{|l|+1}} L_p^{|l|} \left[\frac{2\rho^2}{w^2(z)} \right] \exp \left[-\frac{\rho^2}{w^2(z)} \right] \times \exp \left[ik \frac{\rho^2}{2R(z)} + il\phi - i\Phi^{lp}(z) \right], \quad (2.13)$$

where the Gouy phase $\Phi^{lq}(z)$ for LG modes is

$$\Phi^{lp}(z) = (|l| + 2q + 1) \arctan \left(\frac{z}{z_R} \right). \quad (2.14)$$

$L_p^{|l|}$ is a Laguerre polynomial and the order of a LG mode is determined as $N = |l| + 2q$. The indice q is the mode radial order and the number l is called the topological charge and determines the amount of OAM of the light beam. The phase term $e^{il\phi}$ it is responsible for the twisting phase front and the central vortex represented in Fig. 1. The HG and LG transverse structure are shown in Fig. 4 below.

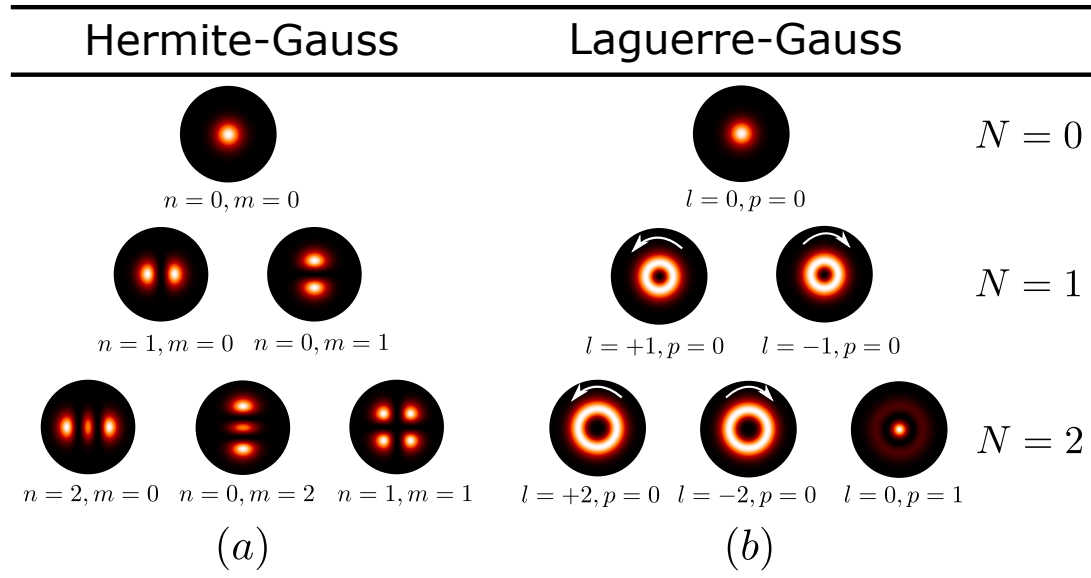


Figure 4 – Different orders intensity profile of HG (a) and LG (b) modes. For HG modes $N = m + n$ and for LG modes $N = |l| + 2q$.

It is very important to mention that the modes ψ_{HG}^{nm} and ψ_{LG}^{lq} forms a basis since those modes are mutually orthogonal to each other [27]. This means that a linear combination of those modes is still a solution of the paraxial Equation.

The general expression relating ψ_{HG}^{nm} and ψ_{LG}^{lq} of order N are [31]

$$\psi_{LG}^{nm} = \sum_{k=0}^N \left[\frac{(N-k)!k!}{2^N n!m!} \right]^{\frac{1}{2}} \frac{1}{k!} \frac{d^k}{dt^k} [(1-t)^n (1+t)^m]_{t=0} \psi_{HG}^{N-k,k}, \quad (2.15)$$

where the topological charge is calculated as $l = n - m$ and the radial number is $q = \min(n, m)$. Fig. 5 below illustrates a few examples of possible combinations of HG modes to generate LG modes.

$$\begin{aligned}
 N = 1 \left\{ \begin{array}{l} \text{HG}_{10}^{00} = \frac{1}{\sqrt{2}} \text{HG}_{10}^{10} - \frac{i}{\sqrt{2}} \text{HG}_{10}^{01} \\ \text{HG}_{10}^{10} = \frac{1}{\sqrt{2}} \text{HG}_{10}^{00} - \frac{1}{\sqrt{2}} \text{HG}_{10}^{01} \end{array} \right. \\
 N = 2 \left\{ \begin{array}{l} \text{HG}_{20}^{00} = \frac{1}{2} \text{HG}_{20}^{20} - \frac{i}{\sqrt{2}} \text{HG}_{20}^{11} - \frac{1}{2} \text{HG}_{20}^{02} \\ \text{HG}_{20}^{02} = \frac{1}{\sqrt{2}} \text{HG}_{20}^{00} + \frac{1}{\sqrt{2}} \text{HG}_{20}^{11} \\ \text{HG}_{20}^{11} = \frac{1}{2} \text{HG}_{20}^{00} - \frac{1}{\sqrt{2}} \text{HG}_{20}^{11} + \frac{1}{2} \text{HG}_{20}^{02} \end{array} \right.
 \end{aligned}$$

Figure 5 – Normalized modes superposition examples. The coefficients in the superposition is generated by Eq. (2.15).

2.1.3 Poincaré Sphere for Spatial Modes

Analogous to the famous Poincaré sphere used to represent the polarization state of light [32] we can conveniently define a sphere to represent first-order modes [33]. To do so we can define a set of parameters given by:

$$o_1 = \frac{I_{HG_{10}^{0^\circ}} - I_{HG_{10}^{90^\circ}}}{I_{HG_{10}^{0^\circ}} + I_{HG_{10}^{90^\circ}}}, \quad (2.16a)$$

$$o_2 = \frac{I_{HG_{10}^{45^\circ}} - I_{HG_{10}^{135^\circ}}}{I_{HG_{10}^{45^\circ}} + I_{HG_{10}^{135^\circ}}}, \quad (2.16b)$$

$$o_3 = \frac{I_{LG_0^1} - I_{LG_0^{-1}}}{I_{LG_0^1} + I_{LG_0^{-1}}}, \quad (2.16c)$$

where $I_{HG_{1,0}^\alpha}$ represents the intensity of HG modes with a given orientation represented by an angle α with respect to the horizontal. $I_{LG_0^{\pm 1}}$ are the intensities

of LG modes with $l = \pm 1$ and $p = 0$. Those parameters satisfies

$$o_1^2 + o_2^2 + o_3^2 = 1. \quad (2.17)$$

The relation (2.17) suggest that the parameters o_1 , o_2 and o_3 define a sphere of unitary radius in which any point on the surface of the sphere represent a first-order mode, according to Fig. 6 below.

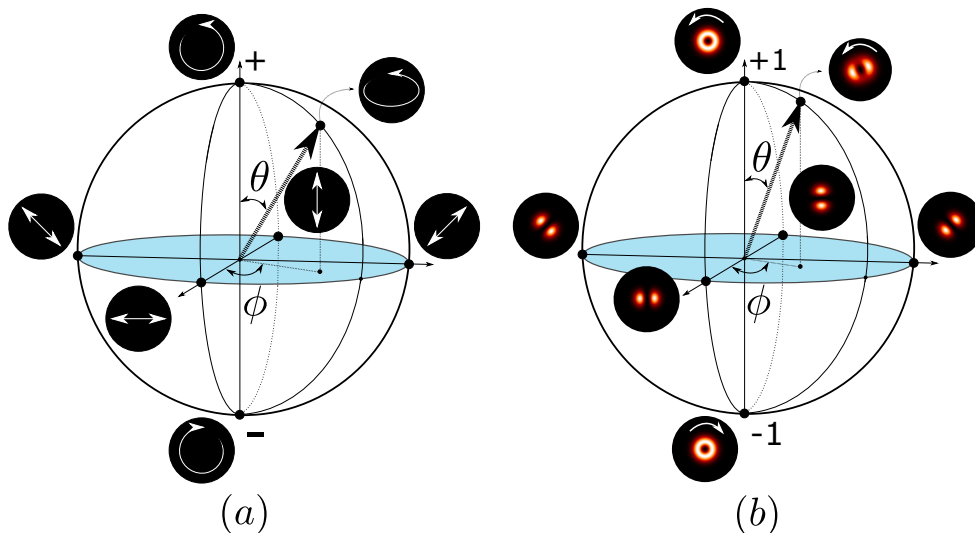


Figure 6 – Analogy between the polarization sphere (a) and first-order OAM sphere (b). Any point on the sphere surface is defined by the spherical coordinates θ and ϕ .

Essentially, we can represent any point on the sphere surface as a linear combinations of its poles. For first-order modes this can be mathematically written as [33]

$$\psi = \cos\left(\frac{\theta}{2}\right) \psi_{LG}^{+10} + e^{i\phi} \sin\left(\frac{\theta}{2}\right) \psi_{LG}^{-10}, \quad (2.18)$$

where θ is the polar angle and ϕ the azimuthal angle in the sphere representation.

The generalization for superior values of OAM is straightforward. Basically, any pair of opposite signs and same OAM magnitude ($|l|$) forms an SU(2) structure [25] which can be written analogous to (2.18). As an example, for an odd order $N = 3$ we can define two independent subspace $\{\psi_{LG}^{\pm|3|0}\}$ and $\{\psi_{LG}^{\pm|1|1}\}$ that realizes an SU(2) structure. In other words, for each subspace we have an independent sphere defined by the OAM values, according to Fig. 7.

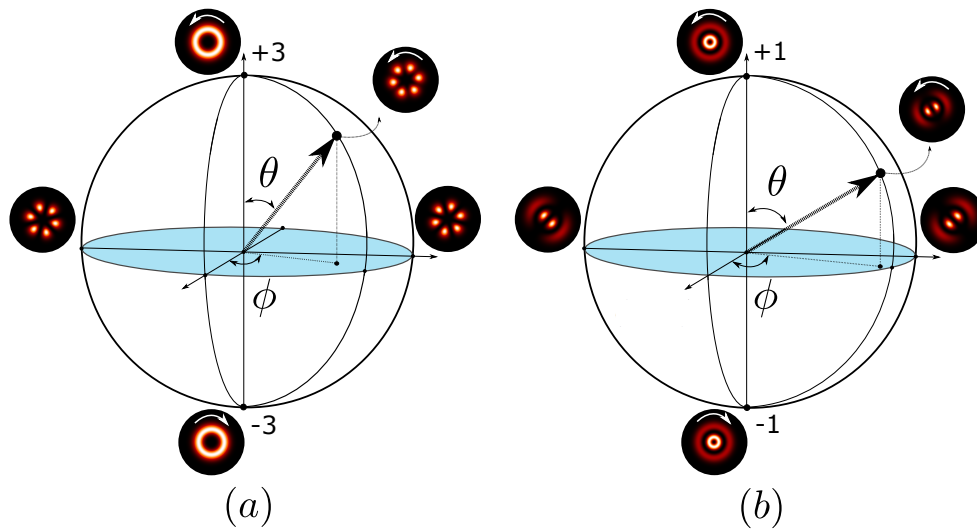


Figure 7 – Third-order OAM spheres. $|l| = 3$ and $q = 0$ on the poles (a) . $|l| = 1$ and $q = 1$ on the poles (b).

2.2 Production and Measurement of OAM beams

In this section we are going to discuss a way to produce and measure the topological charge of a light beam experimentally. There are several ways to produce light with OAM [30]. In this present work, we used a technique that consists of a phase hologram generated on a computer (PC) and imprinted in a device screen. This device is called the spatial light modulator (SLM). The SLM is a device based on Liquid Crystal on Silicon (LCOS) technology in which by applying a voltage signal on the liquid crystal (LC) screen we can modulate the reflected wavefront of a light beam impinging on that screen [34]. The LC alignment is controlled, pixel by pixel, using a controller connected to a PC using a digital video interface (DVI). Fig. 9 below illustrates the basic working principle of the SLM.

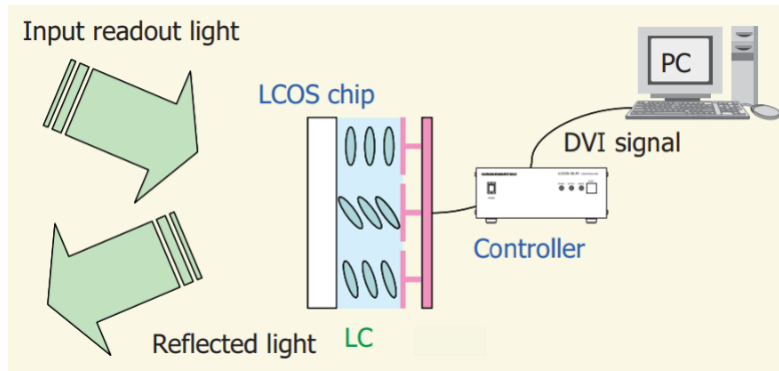


Figure 8 – Illustration of the basic working of a SLM. The reflected light phase structure can be arbitrary manipulated.

The SLM only modulates linear polarized light in a given direction set by the manufacturer [34], so we start by setting the polarization to this direction using a polarizing beam splitter (PBS) and half-wave plate (HWP)¹. The incident light on the SLM screen is modulated with a programmed hologram that is made with a phase ramp and a sawtooth grating. The phase ramp imprints the desired phase structure in the beam. The grating is computed in order to use a setup with angled incidence, which makes this method easier to work with when compared with normal incidence. With this method, many diffraction orders are generated and the desired profile is in the first diffraction order [34]. In Fig. 9 below we can see a illustration to produce a phase hologram for generating a LG mode with $l = 1$ and $q = 0$. In Fig.10 we show a experimental setup of a SLM built in our Lab.

¹ The PBS is a cube that transmits horizontally polarized light and reflects vertically polarized light. The HWP allows changing the orientation of linearly polarized light.

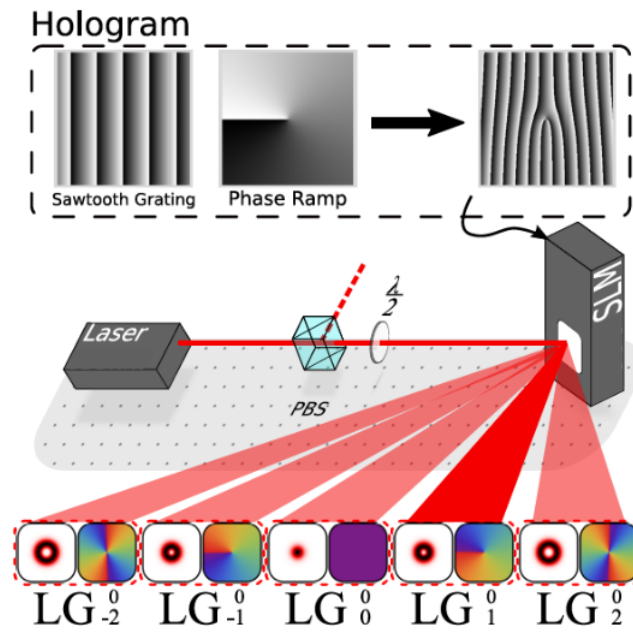
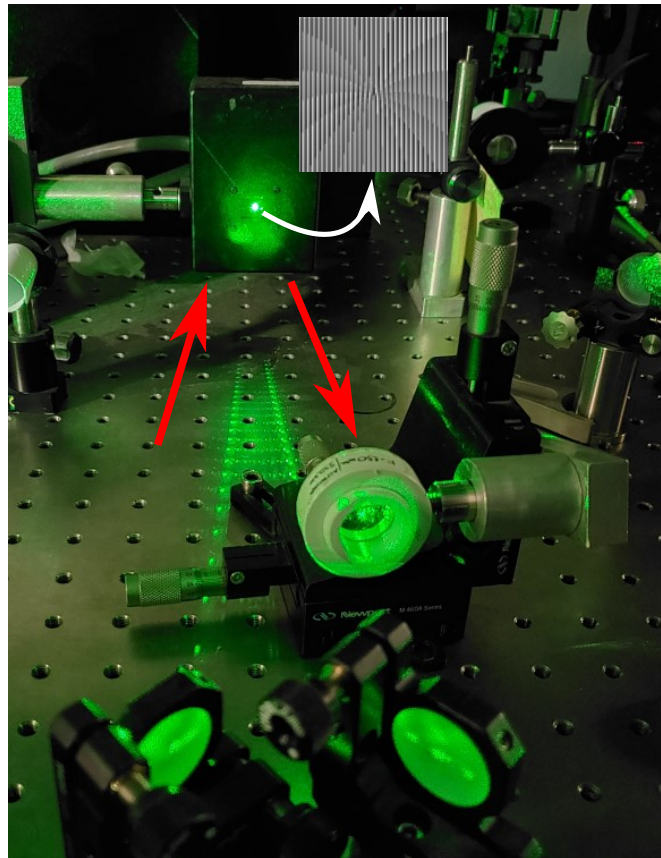
Figure 9 – Basic setup sketch to produce LG modes.

Figure 10 – Experimental setup of our SLM (Hamamatsu, model X10468-01).

In order to measure the topological charge of a light beam we can use an optical element found in any optics laboratory: a spherical bi-convex lens. The method consists of making a slight tilt on the lens which is being overtaken by an OAM beam [35]. Let's suppose for example that an input beam impinging in a tilted lens has a topological charge of l . After passing through the tilted lens it will be produced an HG mode with n bright spots, where $n = |l| + 1$, as illustrated in Fig. 12. The inclination of the produced HG is related to the sign of the topological charge. In other words, two OAM beams with $l = 1$ and $l = -1$ passing through a tilted lens will produce the same HG mode but with different inclinations. A formal description of this method can be found in [35].

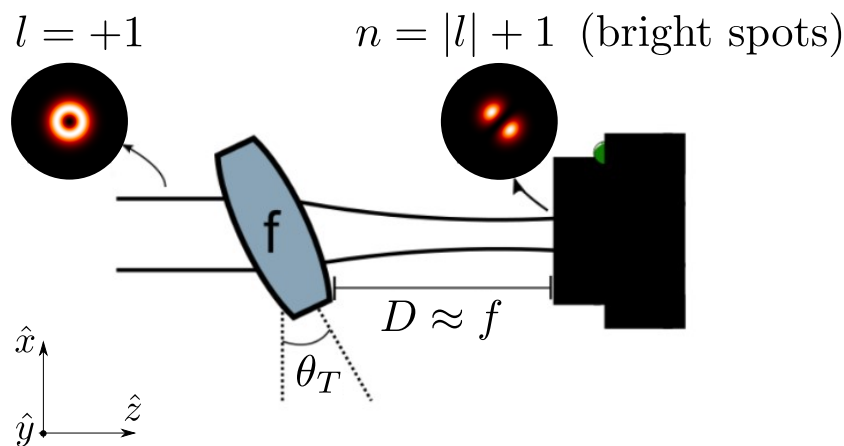


Figure 11 – Illustration of an OAM beam passing through a tilted lens. In this example, the topological charge is $l = 1$, so we will have a first-order HG being produced ($n=2$ bright spots). θ_T is the tilt angle. The HG mode is observed in a distance D close to the focal length f of the lens.

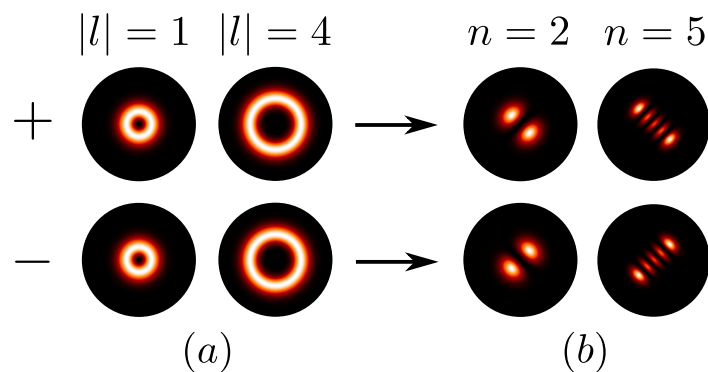


Figure 12 – Input modes in the tilted lens (a) and its respective outputs (b) near focal region.

3 Optical Parametric Oscillator

The optical parametric oscillator (OPO) is a device capable of generating two laser beams often called signal (ω_s) and idler (ω_i), given a input pump beam (ω_p). Its construction is compounded of an optical cavity with a nonlinear and anisotropic material inside of it, pictorially illustrated in Fig. 13. One of the nonlinear phenomenon that might occur in the OPO is called *parametric down conversion*, which consist of a down-frequency conversion of the ω_p wave into two smaller frequencies waves with ω_s and ω_i . In this process we have energy and momentum conservation.

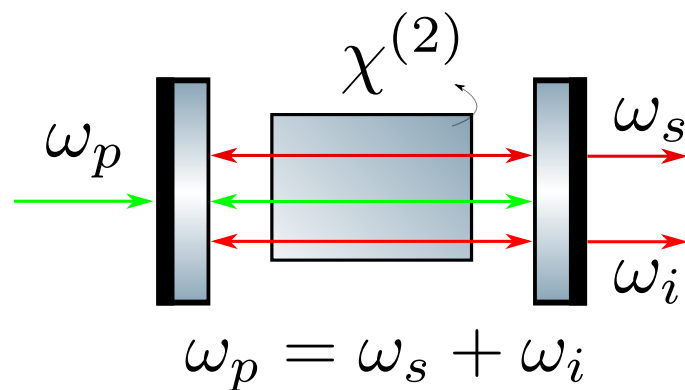


Figure 13 – Optical parametric oscillator. A second-order nonlinear material $\chi^{(2)}$ is placed inside an optical cavity. The three waves involved in the nonlinear material is often called pump (ω_p), signal (ω_s) and idler (ω_i).

In this chapter, we are going to discuss the fundamental concepts to understand how the OPO works in the classical regime. Our goal is to obtain the dynamical equations that govern the pump, signal, and idler modes. To achieve that goal we must review a few important topics. First, we are going to begin our discussion by reviewing the basics of nonlinear optics following references [36, 37]. In particular, we are going to study only second-order nonlinear phenomena which can be understood as three wave mixing process.

Then we are going to discuss the basics of propagation of light in crystals, such as KTP crystal, which is the nonlinear anisotropic media considered in this thesis. The basics of optical cavities will also be studied based on [37, 38, 39, 40] and how to obtain a dynamical equation for the electric field envelope inside a

resonator. By discussing those last topics we are able to obtain the dynamical equations of the OPO in the classical regime and show a few important numerical integrations of them. Also, we are going to discuss the dynamical equations of an injected OPO, which gives rise to an optical parametric amplification (OPA) process. This last phenomenon is very important to understand our theory presented in chapter 4.

3.1 Introduction to Nonlinear Optics

Nonlinear optical phenomena occur whenever the induced polarization in some media response in a nonlinear manner in the strength of the optical field. This nonlinear response can be obtained by applying an intense optical field, such as a laser beam. Physically, we have an intense laser field that can cause the polarization of the medium to develop new frequency components not present in the incident radiation field. A famous example is the second-harmonic generation where an input beam of frequency ω in a nonlinear material can generate an output beam of frequency 2ω [2].

In the next sections we are going to discuss some important second-order nonlinear process driven by a second order susceptibility $\chi^{(2)}$. This last quantity govern 3 wave mixing process such as the parametric down conversion, which is the most important nonlinear process in the OPO. We are going to discuss the solution for the wave equations that involve the waves in a $\chi^{(2)}$ material and discuss the influence of the phase-match condition on the nonlinear process.

3.1.1 Nonlinear Susceptibility

In a linear isotropic medium, the induced polarization is directly proportional to the applied electric field. The proportionality constant is called linear susceptibility $\chi^{(1)}$. In nonlinear optics, the polarization can be written as a power series in terms of the electric field [36]. We are going to discuss only second-order polarization processes given by nonlinear susceptibility $\chi^{(2)}$. When taking account the anisotropy of $\chi^{(2)}$ materials means that the polarization vector need not to be parallel to the applied electric field. In this sense, we have that the $\chi^{(2)}$ is given by a rank 3 tensor and the second-order polarization can be written in Cartesian coordinates as

$$P_i^{(2)}(\omega) = \sum_{jk} \sum_{(nm)} \epsilon_0 \chi_{ijk}^{(2)}(\omega; \omega_n, \omega_m) E_j(\omega_n) E_k(\omega_m), \quad (3.1)$$

where the indices ijk refer to the Cartesian components of the fields. The notation (nm) indicates that, in performing the summation over n and m , the sum $\omega_n + \omega_m = \omega$, although ω_n and ω_m are each allowed to vary. Let's use the result (3.1) to understand important nonlinear process.

- *Second-Harmonic Generation:*

We are going to suppose that we have a plane wave of frequency ω_1 impinging over a $\chi^{(2)}$ nonlinear medium. For simplicity, the wave has a polarization along the x direction and can be represented as

$$\vec{E}(\vec{r}, t) = E_x(\omega_1) e^{i(\vec{k}_1 \vec{r} - \omega_1 t)} \hat{x} + c.c.. \quad (3.2)$$

By calculating $P_i^{(2)}(\omega)$ using (3.1) we obtain¹

$$\begin{aligned} P_i^{(2)}(\omega) = & \epsilon_0 \chi_{ixx}^{(2)}(\omega; \omega_1, \omega_1) [E_x^2(\omega_1) e^{2i(\vec{k}_1 \vec{r} - \omega_1 t)} + c.c. \\ & + E_x(\omega_1) E_x^*(\omega_1) + c.c]. \end{aligned} \quad (3.3)$$

The first term in Eq. (3.3) is called the second-harmonic generated (SHG) of the input field and has a frequency of $\omega = 2\omega_1$. The second term represents the optical rectification which represents an static field in the medium.

- *Sum and Difference frequency generation:*

Now let's suppose that we have two frequencies components in our incident plane wave also polarized in the x -direction:

$$\vec{E}(\vec{r}, t) = [E_{1x}(\omega_1) e^{i(\vec{k}_1 \vec{r} - \omega_1 t)} + E_{2x}(\omega_2) e^{i(\vec{k}_2 \vec{r} - \omega_2 t)} + c.c.] \hat{x}. \quad (3.4)$$

After calculating all terms that appears after calculating (3.1), such as the SHG and optical rectification, let's focus our attention for the terms

$$\begin{aligned} P_i^{(2)}(\omega_3) = & 2\epsilon_0 \{ \chi_{ixx}^{(2)}(\omega_3 = \omega_1 + \omega_2; \omega_1, \omega_2) E_{1x}(\omega_1) E_{2x}(\omega_2) e^{i[(\vec{k}_1 + \vec{k}_2) \vec{r} - (\omega_1 + \omega_2)t]} \\ & + \chi_{ixx}^{(2)}(\omega_3 = \omega_1 - \omega_2; \omega_1, \omega_2) E_{1x}(\omega_1) E_{2x}^*(\omega_2) e^{i[(\vec{k}_1 - \vec{k}_2) \vec{r} - (\omega_1 - \omega_2)t]} \}. \end{aligned} \quad (3.5)$$

The first and second terms in Eq. (3.5) represents, respectively, the sum and difference frequencies generation. There is a nice geometrical interpretation and

¹ The results in this section supposes that $\chi_{ijk}^{(2)}(\omega; \omega_n, \omega_m) = \chi_{ikj}^{(2)}(\omega; \omega_m, \omega_n)$, which is a symmetry hipotesis discussed in [36].

energy-level diagram to visualize the process, according to Figs. (14) and (15). In those figures we are assuming the phase-match condition ($\vec{k}_3 = \vec{k}_1 + \vec{k}_2$), whose importance will be discussed with more details in the next section.

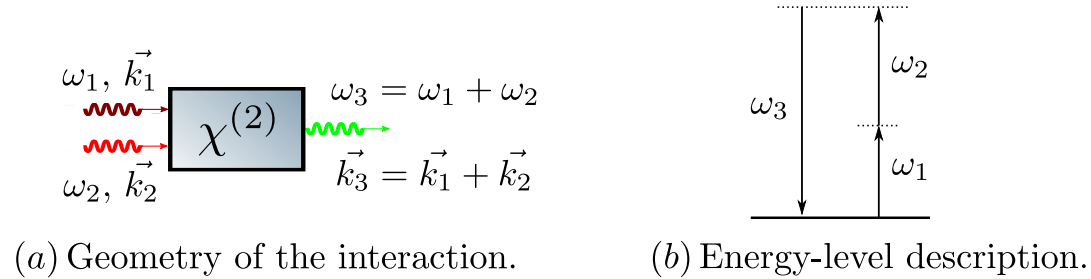


Figure 14 – Sum-Frequency Generation.

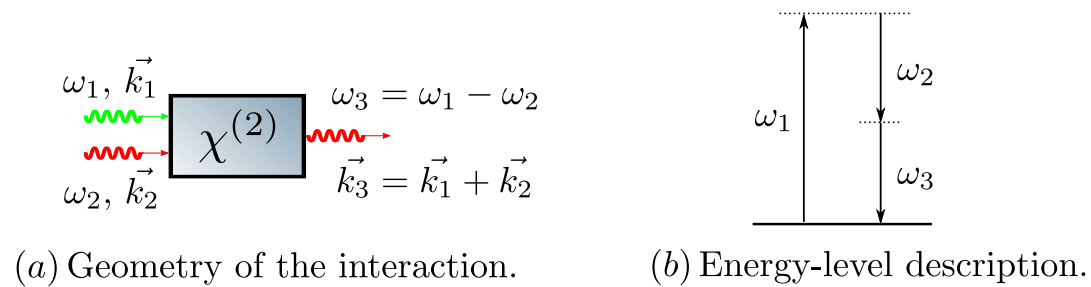


Figure 15 – Difference-Frequency Generation - OPA.

Superficially, difference-frequency generation and sum-frequency generation appear to be very similar processes. By looking at the difference-frequency generation in terms of the energy-level diagram the conservation of energy requires that not only a photon is created at $\omega_3 = \omega_1 - \omega_2$ but also a photon with ω_2 . In other words, when a photon with frequency ω_1 is destroyed we have the amplification of the photon ω_2 , since he is already present in the beginning, and the generation of the photon ω_3 . This process is also known as optical parametric amplification (OPA) and it is explored in this thesis.

3.1.2 3 Wave Mixing Equations and Phase-Matching

We have seen in the last section that the nonlinearity response of a medium can produce new frequencies components not present in the incident radiation field. We are going to examine how the wave equation, derived from Maxwell's equations, describes this nonlinear interaction mechanism and also how the phase-match condition is crucial for maximizing a nonlinear process. Let's begin writing

the wave equation in the absence of free charges ($\rho = 0$), free currents ($\vec{J} = 0$) and assume that the material is nonmagnetic ($\vec{B} = \mu_0 \vec{H}$) [36], so that

$$\vec{\nabla} \times \vec{\nabla} \times \vec{E} + \frac{1}{c^2} \frac{\partial^2 \vec{E}}{\partial t^2} = -\frac{1}{\epsilon_0 c^2} \frac{\partial^2 \vec{P}}{\partial t^2}, \quad (3.6)$$

where c is the vacuum speed of light and ϵ_0 is the vacuum permittivity. Equation (3.6) is the most general form of the wave equation in nonlinear optics. The polarization \vec{P} can be written in terms of a linear part \vec{P}^L and a nonlinear part \vec{P}^{NL} as $\vec{P} = \vec{P}^L + \vec{P}^{NL}$.

By using an identity from vector calculus, and the slowly varying amplitude approximation [36] we can write the first left term in Eq. (3.6) as $\vec{\nabla} \times \vec{\nabla} \times \vec{E} = -\nabla^2 \vec{E}$. As we are in the context of nonlinear optics it is convenient to rewrite (3.6) in terms of the nonlinear part of the polarization \vec{P}^{NL} as [36]

$$\nabla^2 \vec{E}_n - \frac{\epsilon_1(\omega_n)}{c^2} \frac{\partial^2 \vec{E}_n}{\partial t^2} = \frac{1}{\epsilon_0 c^2} \frac{\partial^2 \vec{P}_n^{NL}}{\partial t^2}. \quad (3.7)$$

The Equation (3.7) has the form of a driven wave equation where the nonlinear response of the medium acts as a source term on the right-hand side. This Equation is valid for each frequency component of the field represented with index n . For a isotropic and dispersionless material $\epsilon_1(\omega_n)$ is a frequency dependent relative permittivity constant which is different for each material.

In particular, let's consider the sum-frequency generation in a lossless nonlinear optical medium involving collimated, monochromatic, continuous wave input beams. The Equation (3.7) must hold for each frequency component on the process and in particular for the sum-frequency component at frequency $\omega_3 = \omega_1 + \omega_2$. Let's consider plane wave scalar solution with amplitudes A_j ($j = 1, 2, 3$) propagating in the $+z$ direction as

$$E_j(z, t) = A_j e^{i(k_j z - \omega_j t)} + c.c. \quad (3.8)$$

We expect that the nonlinear source term is not too large so the solution to equation (3.7) will still be of the form of (3.8).

The nonlinear source term for the summed frequency wave ω_3 can be written as

$$P_3(z, t) = P_3 e^{-i\omega_3 t} + c.c., \quad (3.9)$$

where according to first term in equation (3.5) we can couple the fields as $P_3 = 2\epsilon_0 \chi^{(2)} E_1 E_2$. By replacing this last result and Equation (3.8) in (3.7) we

can obtain [36]

$$\frac{d^2 A_3}{dz^2} + 2ik_3 \frac{dA_3}{dz} = -\frac{\omega_3^2 \chi^{(2)}}{cn_3} A_1 A_2 e^{i(k_1+k_2-k_3)z}, \quad (3.10)$$

where n_3 is the refractive index for the wave ω_3 . At this point is permissible to neglect the first term on the left-hand side of (3.10) by considering that it is much smaller than the second [36]. That means, $\left| \frac{d^2 A_3}{dz^2} \right| \ll \left| k_3 \frac{dA_3}{dz} \right|$, which is the slowly varying amplitude approximation.

In general, the spatial variation of the ω_1 and ω_2 waves must also be taken into consideration, and we can derive analogous equations for those fields by repeating the derivation given above for each of these frequencies [36]. In that way we can obtain the 3 differential coupled equations for the 3 wave mixing process as

$$\frac{dA_1}{dz} = \frac{i\chi\omega_1^2}{2n_1c} A_3 A_2^* e^{-i\Delta kz}, \quad (3.11a)$$

$$\frac{dA_2}{dz} = \frac{i\chi\omega_2^2}{2n_2c} A_1^* A_3 e^{-i\Delta kz}, \quad (3.11b)$$

$$\frac{dA_3}{dz} = \frac{i\chi\omega_3^2}{2n_3c} A_1 A_2 e^{i\Delta kz}, \quad (3.11c)$$

where we have introduced the quantity

$$\Delta k = k_1 + k_2 - k_3, \quad (3.12)$$

which is called the wavevector phase mismatch.

- *Phase-Matching Considerations:*

Let's consider, for simplicity, that the amplitudes A_1 and A_2 are approximately constant on the right-hand side of (3.11c). Our main assumption at this point is to consider the phase mismatch (3.14) as

$$\Delta k = 0, \quad (3.13)$$

which is called the phase match condition. Physically, when this condition is fulfilled the generated wave maintains a fixed phase relation with respect to the nonlinear polarization and is able to extract energy most efficiently from the incident waves [36]. A pictorial representation of the phase mismatch vector is shown in Fig. 16 below.

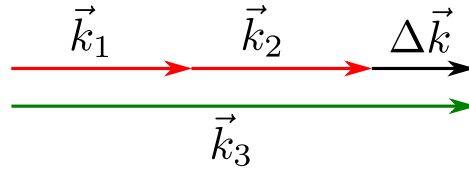


Figure 16 – Pictorial representation of phase mismatch vector $\Delta\vec{k}$ in sum-frequency generation process.

When the condition (3.13) is not considered the intensity of the radiation emitted at ω_3 is smaller. We can understand the process by integrating (3.11c) along a nonlinear medium of length L (considering $A_3(0) = 0$) so that

$$A_3(L) = \frac{i\chi\omega_3^2}{2n_3c} A_1 A_2 \int_0^L e^{i\Delta k z} dz = \frac{i\chi\omega_3^2}{2n_3c} A_1 A_2 \left(\frac{e^{i\Delta k L} - 1}{i\Delta k} \right). \quad (3.14)$$

Now by integrating the result above we can obtain $I_3 = |A_3(L)|^2$ as

$$I_3 = \left(\frac{\chi}{2n_3c} \right)^2 \omega_3^4 I_1 I_2 L^2 \frac{\sin^2 \left(\frac{\Delta k L}{2} \right)}{\left(\frac{\Delta k L}{2} \right)^2}. \quad (3.15)$$

The Fig. 17 below illustrate the graphic of I_3 as a function of the mismatch Δk .

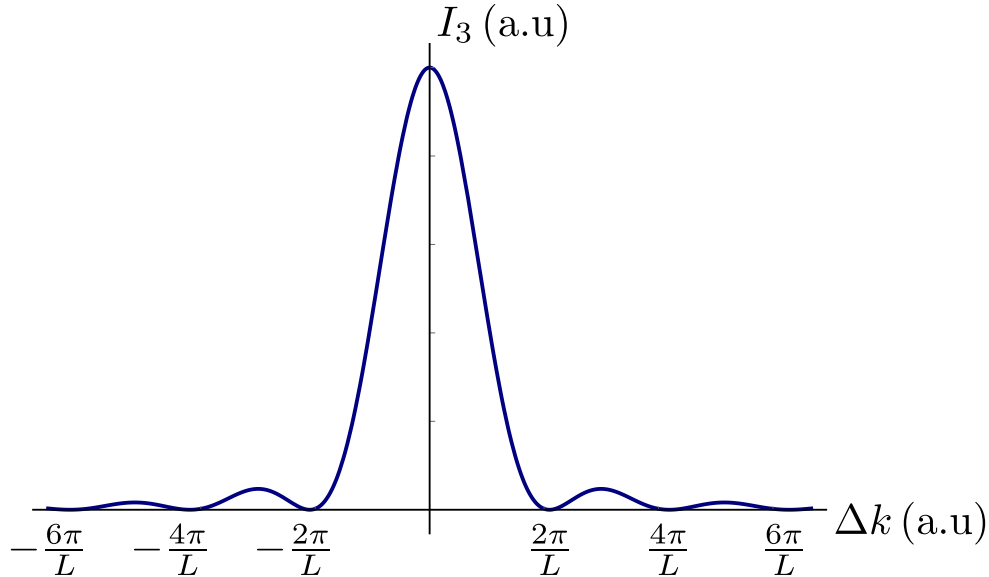


Figure 17 – I_3 as a function of the mismatch Δk .

Our discussion until now is made considering plane waves only. In a real-world experiment, however, we are dealing with structured light such as the structures discussed in the previous chapter. By considering the transverse

structure of a laser beam travelling in a nonlinear crystal we must rewrite the coupled differential equations as [43]

$$\frac{d\alpha_1^{lp}}{dz} = \frac{i\chi\omega_1^2}{2n_1c} \sum_{mq, nr} \Lambda_{pqr}^{lmn}(z) \alpha_3^{nr} (\alpha_2^{mq})^* e^{-i\Delta kz}; \quad (3.16a)$$

$$\frac{d\alpha_2^{mq}}{dz} = \frac{i\chi\omega_2^2}{2n_2c} \sum_{lp, nr} \Lambda_{pqr}^{lmn}(z) (\alpha_1^{lp})^* \alpha_3^{nr} e^{-i\Delta kz}; \quad (3.16b)$$

$$\frac{d\alpha_3^{nr}}{dz} = \frac{i\chi\omega_3^2}{2n_3c} \left[\sum_{lp, mq} \Lambda_{pqr}^{lmn}(z) \right]^* \alpha_1^{lp} \alpha_2^{mq} e^{i\Delta kz}. \quad (3.16c)$$

At this point we are considering the complex amplitudes α_j^{ab} belonging to the LG basis (ψ_{LG}^{lq}) previous exposed. The indice $j = 1, 2, 3$ is the frequency indice of each mode. The indice $a = l, m, n$ is the topological charge and $b = p, q, r$ is the radial order indice. The term²

$$\Lambda_{pqr}^{lmn}(z) = 2\pi \int \rho d\rho [\psi_0^{lp}(\rho, \phi, z)]^* \psi_1^{mq}(\rho, \phi, z) \psi_2^{nr}(\rho, \phi, z). \quad (3.17)$$

is an integral known as overlap transverse coupling and plays an important role to determine which transverse modes can be coupled inside the nonlinear process [43]. The integral (3.17) implies the general selection rule $l = m + n$, which is OAM conservation [48].

3.2 Propagation of Light in Crystals

The goal in this section is to give a basic understanding of light propagation in crystals. One of the main features, as far as optical properties are concerned, is that crystals are generally electrically anisotropic. Physically, this means that the polarization in such media is not just a scalar constant times the applied electric field [38]. The dependence of \vec{P} on \vec{E} is expressible as a tensor relation in the form

$$\vec{P} = \epsilon_0 \vec{\chi} \vec{E} \equiv \begin{bmatrix} P_x \\ P_y \\ P_z \end{bmatrix} = \epsilon_0 \begin{bmatrix} \chi_{xx} & \chi_{xy} & \chi_{xz} \\ \chi_{yx} & \chi_{yy} & \chi_{yz} \\ \chi_{zx} & \chi_{zy} & \chi_{zz} \end{bmatrix} \begin{bmatrix} E_x \\ E_y \\ E_z \end{bmatrix}. \quad (3.18)$$

Consequently, the speed of light in such media is a function of the direction of propagation and polarization. Essentially, for a given direction of propagation, we have two distinct phase velocities. Each velocity is associated with distinct polarizations often called *ordinary* and *extraordinary* polarizations.

² By choosing HG modes ψ_{HG}^{nm} the integral should be performed in cartesian coordinates. The results are base independent [43].

In this section, we are going to assume only plane wave solutions $\vec{E}(\vec{r}, t) = \vec{E}_0 e^{i(\vec{k}\vec{r} - \omega t)}$. From equation (3.6), previously discussed, we are going to use the identity $\vec{\nabla} \times (\vec{\nabla} \times \vec{E}) = -(\vec{k} \times \vec{k} \times \vec{E})$ [37]. Given this last consideration we can obtain

$$\vec{k} \times \vec{k} \times \vec{E} = -\frac{\omega^2}{c^2} \frac{\mathcal{E}}{\epsilon_0} \vec{E}, \quad (3.19)$$

where $\vec{\mathcal{E}} = \epsilon_0(\mathbf{1} + \vec{\chi})$ is called the dielectric tensor ($\mathbf{1}$ is a unitary matrix) [38]. The result (3.19) can be written in terms of its components as

$$(k_x^2 - k^2) E_x + k_x k_y E_y + k_x k_z E_z = -k_0^2 \frac{\mathcal{E}_{xx}}{\epsilon_0} E_x, \quad (3.20a)$$

$$k_y k_x E_x + (k_y^2 - k^2) E_y + k_y k_z E_z = -k_0^2 \frac{\mathcal{E}_{yy}}{\epsilon_0} E_y, \quad (3.20b)$$

$$k_z k_x E_x + k_z k_y E_y + (k_z^2 - k^2) E_z = -k_0^2 \frac{\mathcal{E}_{zz}}{\epsilon_0} E_z, \quad (3.20c)$$

where $k^2 = k_x^2 + k_y^2 + k_z^2$ and $k_0 = \frac{\omega}{c}$ is the wavenumber module and c is the speed of light in vacuum. The terms \mathcal{E}_{jj} are related to the refractive index in the x , y , and z directions as $n_j = \sqrt{\mathcal{E}_{jj}/\epsilon_0}$ ($j = x, y, z$).

In order to interpret the physical meaning of these equations, let's consider a few particular cases. Firstly, we will consider a wave propagating in the x -direction and then in the xy plane. The mathematical procedure to an arbitrary direction is analogous. Basically, we have to evaluate the determinant of the coefficient matrix of (3.20a), (3.20b) and (3.20c) and make it null in order to have non-zero solutions for the electric field [37]. In other words, we have to evaluate

$$\begin{vmatrix} (n_x^2 k_0^2 - k_y^2 - k_z^2) & k_x k_y & k_x k_z \\ k_y k_x & (n_y^2 k_0^2 - k_x^2 - k_z^2) & k_y k_z \\ k_z k_x & k_z k_y & (n_z^2 k_0^2 - k_x^2 - k_y^2) \end{vmatrix} = 0. \quad (3.21)$$

- *Propagation in the x -direction:*

For a wave propagating in the x -direction we have that $k_x = k$ and $k_y = k_z = 0$. By making this assumption the determinant (3.21) becomes

$$n_x^2 k_0^2 (n_y^2 k_0^2 - k_x^2) (n_z^2 k_0^2 - k_x^2) = 0, \quad (3.22)$$

where $k_x = n_y k_0$ or $k_x = n_z k_0$ are 2 possible solutions.

If $k_x = n_y k_0$, we can obtain from (3.20a), (3.20b) and (3.20c) that $E_y \neq 0$ and $E_x = E_z = 0$ (polarization in y -direction). Similarly, using the other possible

solution $k_x = n_z k_0$ we get from same equations that $E_z \neq 0$ and $E_x = E_y = 0$ (polarization in z -direction). More generally, we can observe that for a given propagation direction in a anisotropic medium we always have two possible distinct phase velocities³ $v_p = \omega/k$.

- *Propagation in the xy plane:*

For propagation in the xy plane we would have only $k_z = 0$. The determinant (3.21), therefore, would become

$$(n_z^2 k_0^2 - k_x^2 - k_y^2) \left[(n_x^2 k_0^2 - k_y^2) (n_y^2 k_0^2 - k_x^2) - k_x^2 k_y^2 \right] = 0, \quad (3.23)$$

where again we have 2 possible solutions. The first one is

$$k_x^2 + k_y^2 = n_z^2 k_0^2, \quad (3.24)$$

which is a circle in \vec{k} space, more precisely in the xy plane. Using (3.24) in equations (3.20a), (3.20b) and (3.20c) we can obtain that the wave is polarized in z -direction ($E_x = E_y = 0$), which is perpendicular to the direction of propagation. Using the relations $k_x = k \cos \theta$ and $k_y = k \sin \theta$, where θ is the angle between \vec{k} and \hat{x} , in (3.24) we can see that the wave experience same refractive index $n_z = k/k_0$. This physically means that this wave does not undergo any anisotropic effect. This wave is called *ordinary wave* [38].

The other solution of (3.23) gives rise to an ellipse

$$\frac{k_x^2}{n_y^2 k_0^2} + \frac{k_y^2}{n_x^2 k_0^2} = 1, \quad (3.25)$$

where, by similar calculation, we can obtain that the wave is polarized in the xy plane ($E_z = 0$), that means, parallel to the plane. Once again using the relations $k_x = k \cos \theta$ and $k_y = k \sin \theta$, where θ is the angle between \vec{k} and \hat{x} in (3.25) the refractive index, by definition $n = k/k_0$, will become angle-dependent as

$$\frac{1}{n^2(\theta)} = \frac{\cos^2 \theta}{n_y^2} + \frac{\sin^2 \theta}{n_x^2}. \quad (3.26)$$

From (3.26) we can interpret that the for any propagation direction the wave will experience different refractive index. The wave that undergoes this effect is called the *extraordinary wave*.

³ If $n_y = n_z$ the field would not experience any anisotropic effect.

In the xz ($k_y = 0$) and yz ($k_x = 0$) planes we get similar equations and the conclusions are analogous. We also obtain circles and ellipses in each coordinate plane on \vec{k} space. The intersection of the circle and ellipse in a given plane define a direction called an *optical axis* of the crystal, according to Fig. 18. When propagating in the direction of an optical axis, the phase velocities of the two orthogonally polarized waves (ordinary and extraordinary) reduce to the same value [38].

There are mainly two types of crystals: *Uniaxial* (one optical axis) and *Biaxial* (two optical axis) crystals. The type of crystal depends on the principal refractive indexes n_x, n_y and n_z . For a uniaxial crystal we must have two equals refractive index, for example, $n_x = n_y \neq n_z$. A biaxial crystal must have all three refractive indexes different ($n_x \neq n_y \neq n_z$). In a uniaxial crystal we can map the n_x and n_y indexes to the extraordinary refractive index n_e and the n_z index to the ordinary index n_o , where we are supposing propagation in xy plane. A uniaxial crystal is said to be *positive* when $n_e > n_o$ the or *negative* when $n_e < n_o$.

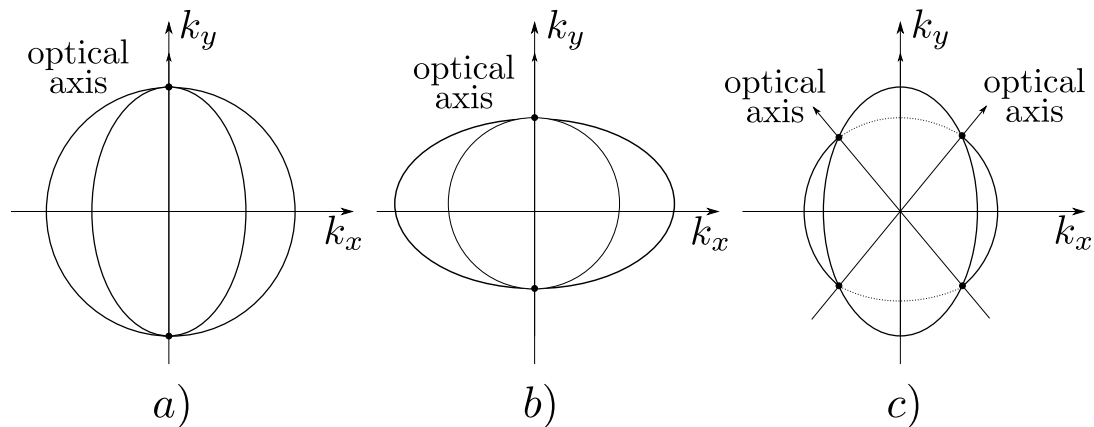


Figure 18 – Circles and ellipses on \vec{k} space. a) Uniaxial negative ($n_e < n_o$). b) Uniaxial positive ($n_e > n_o$). c) Biaxial.

- *Walk-off effect:*

An interesting effect that occurs by consequence of the anisotropy of the medium is the walk-off effect. The wave vector \vec{k} and the electric field \vec{E} vectors are perpendicular in an isotropic medium. The walk-off effect, basically, makes those vector not perpendiculars any more [37]. We can mathematically conclude the effect by calculating one of Maxwell's equations, in absence of

charge, $\vec{\nabla} \cdot \vec{D} = 0$, where $\vec{D} = \mathcal{E}\vec{E}$ is the electric displacement [49]

$$\vec{\nabla} \cdot \vec{D} = \mathcal{E}_{xx} \frac{\partial E_x}{\partial x} + \mathcal{E}_{yy} \frac{\partial E_y}{\partial y} + \cancel{\mathcal{E}_{zz} \frac{\partial E_z}{\partial z}} = 0 \longrightarrow n_x^2 k_x E_x + n_y^2 k_y E_y = 0. \quad (3.27)$$

where the wave is propagating on the xy plane, $n_j^2 = \mathcal{E}_{jj}/\epsilon_0$ and $\frac{\partial E_j}{\partial j} = ik_j E_j$ ($j = x, y, z$). Since we are in an anisotropic medium context we have that $n_x \neq n_y$. From Eq. (3.27) we can conclude that the dot product $\vec{k} \cdot \vec{E} \neq 0$, that means, they are not mutually orthogonal. This means that the wave vector will no longer be parallel to the Poynting vector \vec{S} , since $\vec{S} = (\vec{E} \times \vec{B})/\epsilon_0$. This last physical fact gives rise to the walk-off angle θ_w [37]:⁴

$$\cos \theta_w = \frac{\sin^2 \theta + \gamma^2 \cos^2 \theta}{\sqrt{\sin^2 \theta + \gamma^4 \cos^2 \theta}}, \quad (3.28)$$

where $\gamma = n_e/n_o$ and θ is the angle between \vec{k} and the optical axis. Fig. 70 below represents the walk-off angle.

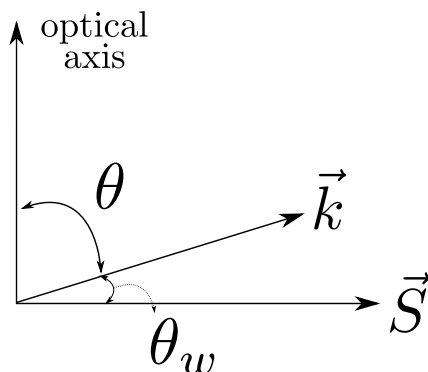


Figure 19 – Pictorial representation of walk-off angle θ_w .

3.2.1 KTP Crystal

In this present work, we are using a KTP (Potassium titanyl phosphate) crystal as $\chi^{(2)}$ nonlinear anisotropic medium. The KTP is said to have a type-II phase-matching. This means that in a parametric down-conversion process, for example, the down-converted beams have mutually orthogonal polarization. One of those polarization is the *extraordinary* (e) and the other is the *ordinary* (o) previously discussed. The KTP is Biaxial, which means, have all different refractive index $n_x \neq n_y \neq n_z$. In order to maximize nonlinear effects, the angle between the wave vector and the z -direction is $\theta = 90^\circ$. Also, the angle between

⁴ Mathematical details on appendix A

the propagation direction and x -direction is $\phi \approx 23^\circ$ [50]. Fig. 20 below illustrates some features of the KTP crystal

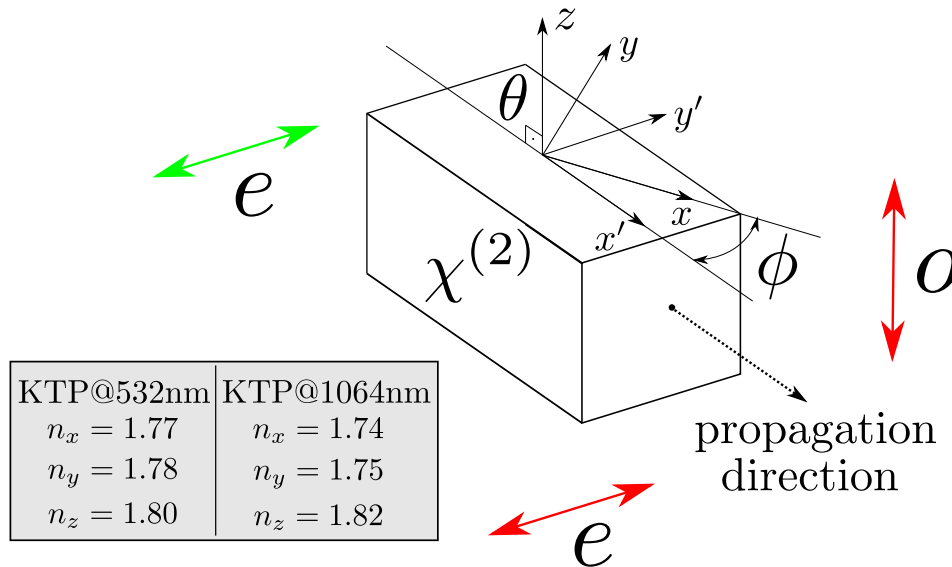


Figure 20 – Type 2 phase-match on a KTP crystal in a parametric down-conversion process. For our KTP crystal, cut for type-II phase matching of 532 and 1064 nm, we have $\phi = 23.5^\circ$ and $\theta = 90^\circ$. In this sketch we are considering the extraordinary (e) wave to be horizontally polarized and the ordinary (o) wave vertically polarized.

3.3 Optical Resonators

An optical resonator has essentially two main purposes [39]: *i*) to build up large field intensities in its interior given a moderated power input; *ii*) acts as a frequency and spatial filter when pumped with a light beam. To explore nonlinear effects, we should have a large amount of intensity in the nonlinear medium [36]. The frequencies and spatial selected modes are determined by the condition that the complete round trip phase delay be some multiple of 2π .

In this section, we are going to discuss only the linear cavities configurations as illustrated in Fig. 21. In a simple manner, a stable resonator accommodates modes that can reflect back and forth in the mirrors such that the beam does not miss in the reflection and is thus lost.

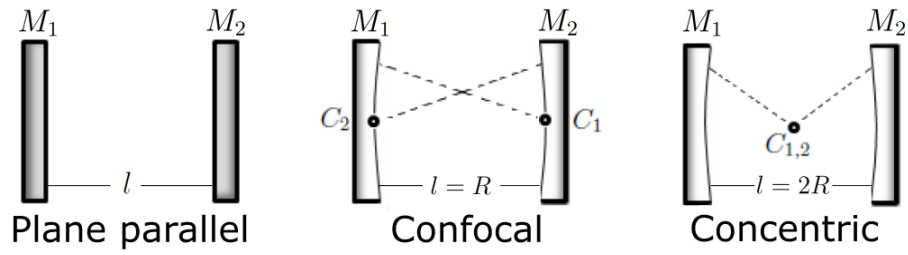


Figure 21 – Examples of linear symmetrical configurations for optical cavities of length l and radius of curvature R . $C_{1,2}$ represents the curvature center of the mirrors.

The stability condition depends in the separation l between the mirrors and their radii of curvature R_1 and R_2 . By defining a $g_i = 1 - l/R_i$ ($i = 1, 2$) parameter the stability condition for a given mode to oscillate in a resonator is [41]

$$0 \leq \left(1 - \frac{l}{R_1}\right) \left(1 - \frac{l}{R_2}\right) \leq 1, \quad (3.29)$$

where the condition (3.29) can be visualized in a diagram in Fig. 22.

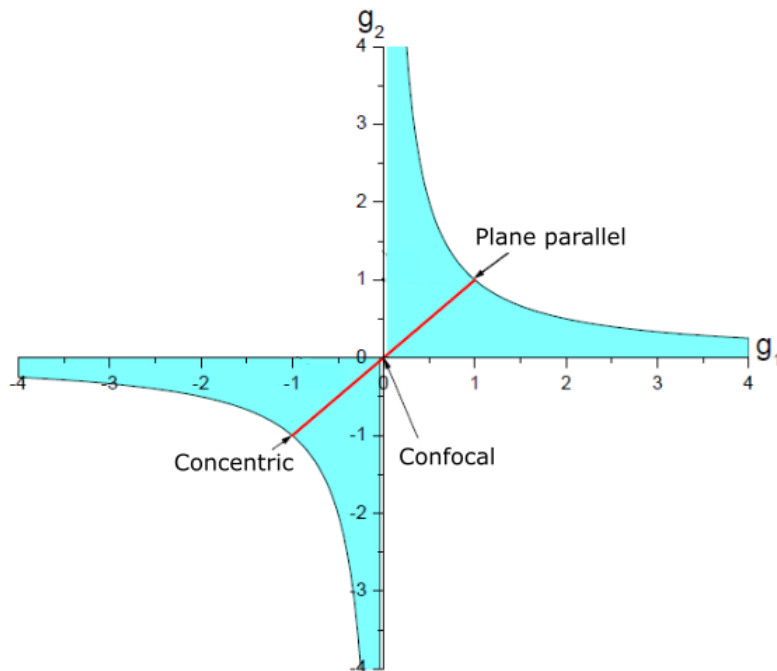


Figure 22 – Stability diagram for g parameters. The blue shaded region indicates stable regimes.

Let's continue our discussion by presenting the Fabry-Perot resonator. In this resonator model, we are going to take into account only the variation of the

amplitude and propagation phase of an electric field, without worrying about the transverse mode. Then we are going to discuss how the geometrical properties of the cavity impose the beam waist to have a precise value. After that we are going to discuss the resonance condition for transverse modes in a resonator.

3.3.1 Fabry-Perot Resonator

The Fabry-Perot resonator is a plane parallel cavity of length L with mirrors reflectivities r_1, r_2 and transmissivities t_1, t_2 , according to Fig. 23. Our goal in this section is to discuss the transmitted intensity of this cavity given an input field. To do so we can write the transmitted field E_T after several reflections inside the cavity as

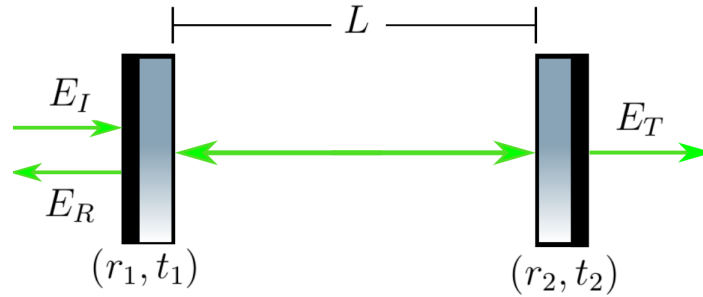


Figure 23 – Fabry-Perot Resonator of length L . E_I , E_R , and E_T are, respectively, the incident, reflected, and transmitted electric field strength.

$$E_T = E_I t_1 t_2 e^{\frac{i\phi}{2}} + E_I t_1 r_2 r_1 t_2 e^{\frac{3i\phi}{2}} + E_I t_1 r_2^2 r_1^2 t_2 e^{\frac{5i\phi}{2}} + \dots \equiv E_I t_1 t_2 e^{\frac{i\phi}{2}} \sum_{n=0}^{\infty} (r_1 r_2 e^{i\phi})^n, \quad (3.30)$$

where $\phi = \left(\frac{2\pi}{\lambda}\right) 2L$ is the phase acquired in a round trip. The result (3.30) is a convergent geometric series⁵ that can be written as

$$E_T = \frac{t_1 t_2 e^{\frac{i\phi}{2}}}{1 - r_1 r_2 e^{i\phi}} E_I. \quad (3.31)$$

By taking the square modulus of (3.31) we can obtain the transmitted intensity of the resonator as (more details in appendix B) [37]

$$I_T = \frac{I_I T_1 T_2}{(1 - \sqrt{R_1 R_2})^2} \frac{1}{1 + \zeta \sin^2\left(\frac{\phi}{2}\right)}, \quad (3.32)$$

⁵ $\sum_{n=0}^{\infty} q^n = \frac{1}{1-q}$, if $|q| < 1$

where $T_j = |t_j|^2$ and $R_j = |r_j|^2$ ($j = 1, 2$) are the transmission and reflection coefficients of the mirrors and $\zeta = \frac{4\sqrt{R_1 R_2}}{(1 - \sqrt{R_1 R_2})^2}$. From (3.32) we can see that the transmitted intensity has two factors where the first one is a constant given by the mirrors specifications and the second one depends on the phase ϕ . This second term is known as the *Airy function*. We can note from 3.32 that I_T is maximum whenever $\phi = 2\pi n$. In Fig. 24 below we can see the graph of I_T versus ϕ , where we show the free spectral range $\Delta\nu$ (FSR) of the cavity and its linewidth $\delta\nu$. In the following section we are going to discuss those quantities in more details. The FSR $\Delta\nu$ of a cavity is equivalent to the inverse interval of time for the light to complete a round trip and the linewidth $\delta\nu$ is commonly defined as the full width at half maximum (FWHM) of the resonance peak.

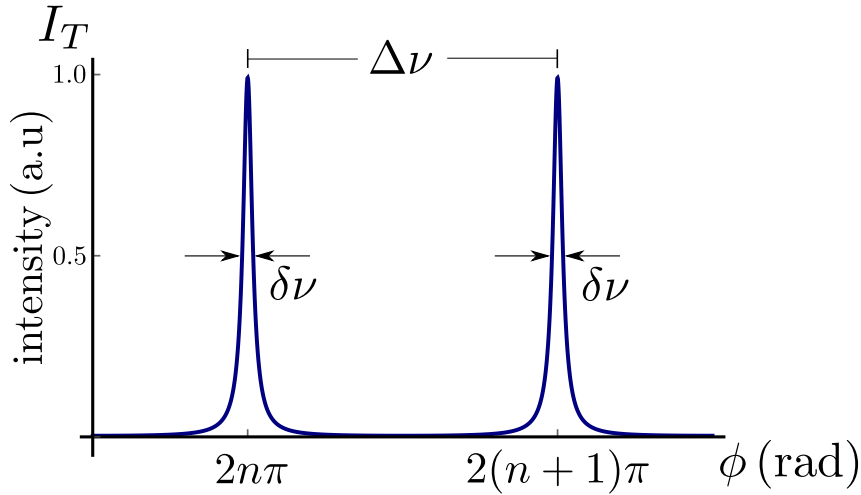


Figure 24 – Airy peaks of an optical resonator. $\Delta\nu$ is the FSR and $\delta\nu$ is the cavity linewidth. The resonance is achieved when ϕ is a multiple of 2π .

- *Cavity Finesse:*

An important quantity relevant to quantify the cavity losses is the so-called *Finesse* and is defined as

$$F = \frac{\Delta\nu}{\delta\nu}. \quad (3.33)$$

Its value is associated with the reflection coefficients of the mirrors and is given by (more details in appendix A)

$$F = \frac{\pi}{2 \arcsin\left(\frac{1 - \sqrt{\rho}}{2\sqrt{\rho}}\right)}, \quad (3.34)$$

where $\rho = R_1 R_2$. By using Eq. (3.34) we can rewrite the transmitted intensity of an resonator as [40]

$$I_T = \frac{I_I T_1 T_2}{(1 - \sqrt{R_1 R_2})^2} \frac{1}{1 + \frac{\sin^2(\frac{\phi}{2})}{\sin^2(\frac{\pi}{2F})}}. \quad (3.35)$$

Low finesse values imply high losses and a widening of the resonance peaks and for high values of finesse the opposite, according to Fig. 25.

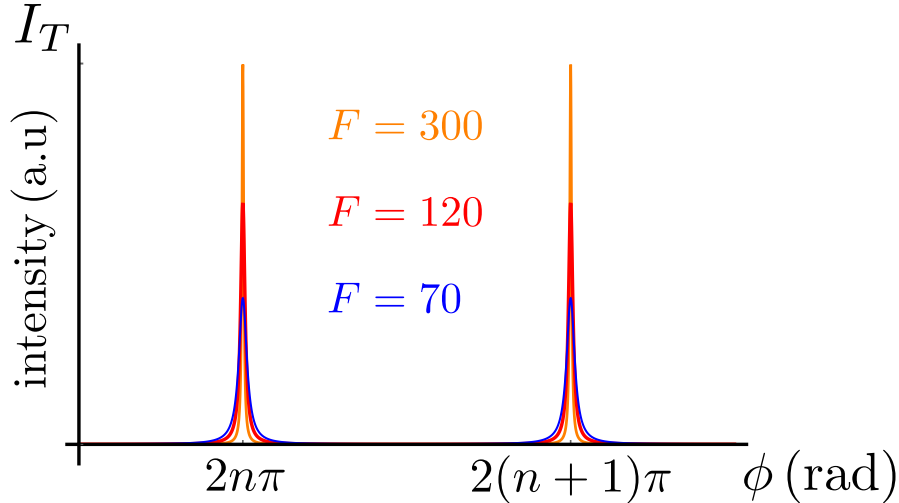


Figure 25 – I_T versus ϕ for three distinct cavities finesse.

3.3.2 Transverse Modes in Optical Resonators

Our goal in this section is to discuss the resonance conditions to have a stable oscillation for a transverse mode in an optical resonator [39]. In order to achieve it, we are going to consider the spatial mode characteristics, such as the radius of curvature of the phase front $R(z)$ ((2.9)) and the beam spot size $w(z)$ ((2.10)).

Let's start considering two mirrors, with spherical radii of curvature R_1 (at z_1) and R_2 (at z_2) and some distance of separation l , according to Fig. 26. It is possible to have a propagating beam mode that reflects back and forth between the mirrors without a change in its transverse profile. To achieve that condition it is necessary that the radius of the curvature of the beam phase front matches the radii of curvature of the mirrors, such that $R(z_1) = R_1 = z_1 + z_R^2/z_1$ and $R(z_2) = R_2 = z_2 + z_R^2/z_2$. From which we get

$$\begin{aligned} z_1 &= \frac{R_1}{2} \pm \frac{1}{2} \sqrt{R_1^2 - 4z_R^2}, \\ z_2 &= \frac{R_2}{2} \pm \frac{1}{2} \sqrt{R_2^2 - 4z_R^2}. \end{aligned} \quad (3.36)$$

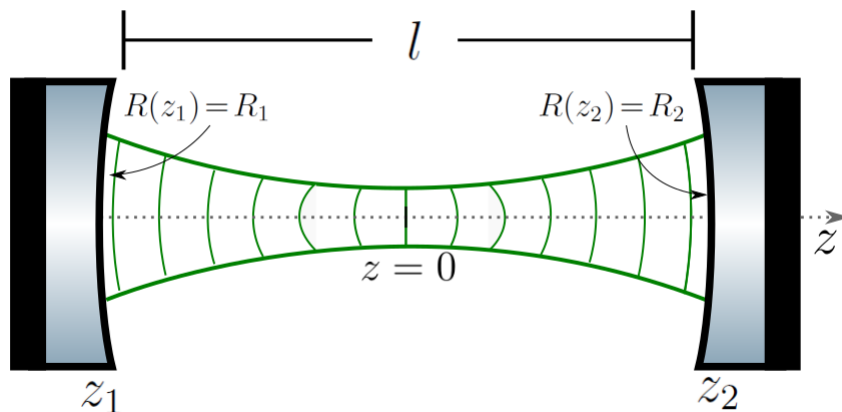


Figure 26 – Mode match in an optical cavity. The cavity length l , as well as the mirror's radius of curvature R_1 and R_2 defines the beam waist for stable oscillation.

By taking the mirror spacing as $l = z_2 - z_1 > 0$, we solve (3.36) for z_R^2 , where z_2 is to right of z_1 and mirror curvature is taken as positive when the center of curvature is to the left of the mirror. We obtain

$$z_R^2 = \frac{l(-R_1 - l)(R_2 - l)(R_2 - R_1 - l)}{(R_2 - R_1 - 2l)^2}. \quad (3.37)$$

For a symmetrical confocal cavity, such that $R_2 = -R_1 = R = l$, we have that the Rayleigh length is $z_R = \sqrt{(2R - l)l}/2$. From the relation $w_0 = \sqrt{(\lambda z_R / \pi n)}$ we should have a beam waist localized in $z = 0$ equals to

$$(w_0)_{conf} = \left(\frac{\lambda l}{2\pi n} \right), \quad (3.38)$$

where n is the medium refractive index.

At this point we have just discussed the geometrical conditions to have a stable oscillation mode. Let's focus now on the phase condition of the intracavity wave in order to have resonance, that means, the phase difference between the ends of the two mirrors must be an integer multiple of π .

$$\theta_{m,n}(z_2) - \theta_{m,n}(z_1) = q\pi, \quad (3.39)$$

where $\theta_{m,n}(z) = kz - (m + n + 1)\Theta(z)$ is the phase shift on the propagation axis, where we are considering the Gouy phase term $\Theta(z) = \arctan(z/z_R)$. By using (3.39) we can obtain the resonance condition for a given mode as [39]

$$k_q l - (m + n + 1) \left[\arctan\left(\frac{z_2}{z_R}\right) - \arctan\left(\frac{z_1}{z_R}\right) \right] = q\pi \quad (3.40)$$

Let's consider the effect of varying the transverse mode indices m and n in a given resonance mode q , such that

$$k_1 l - (m + n + 1)_1 \arctan(z_1/z_R) = q\pi, \quad (3.41)$$

$$k_2 l - (m + n + 1)_2 \arctan(z_2/z_R) = q\pi. \quad (3.42)$$

By subtracting (3.41) and (3.42) and considering that $k_1 - k_2 = 2\pi(\Delta\nu)n/c$ yields [39]

$$\Delta\nu = \frac{c}{2\pi l n} \Delta(m + n) \left[\arctan\left(\frac{z_2}{z_R}\right) - \arctan\left(\frac{z_1}{z_R}\right) \right]. \quad (3.43)$$

Let's consider two examples, the confocal resonator ($l = R$) and the near concentric resonator ($l \approx 2R$). For the confocal cavity $z_2 = -z_1 = z_R$, therefore $\arctan(z_2/z_R) = -\arctan(z_1/z_R) = \pi/4$. For the near concentric resonator we have that $z_R \rightarrow \infty$ and $z_2 = -z_1 = 2z_R$, therefore $\arctan(z_2/z_R) = -\arctan(z_1/z_R) \rightarrow \pi/2$. For those cavities configurations we have

$$(\Delta\nu)_{conf} = \frac{c}{2ln} \frac{\Delta(m+n)}{2}, \quad (3.44)$$

$$(\Delta\nu)_{conc} = \frac{c}{2ln} \Delta(m + n). \quad (3.45)$$

From (3.44) we find that in the confocal resonator the resonance frequencies of the transverse modes, resulting from changing m and n , either coincide or fall halfway between those that result from a change in the longitudinal mode index q [39]. From (3.45) we see that the resonance frequencies of the transverse modes, resulting from changing m and n , coincide from a change in the longitudinal mode index q . On the Fig. 27 below we show an example that a first order HG_{10} mode can resonate in different positions depending on the cavity configuration.

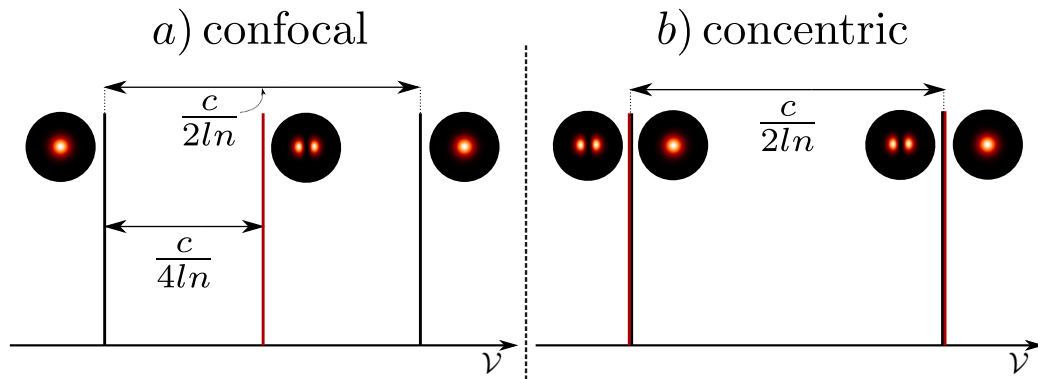


Figure 27 – In a confocal resonator (a), we can expect that a HG_{10} mode will resonate in the middle of the FSR of a Gaussian mode. On the other hand, in a concentric resonator (b), we might expect that a HG_{10} will resonate together with a Gaussian mode.

3.3.3 Dynamical Equation in a Resonator

The goal in this section is to obtain a time dependent differential equation for the electric field amplitude envelope inside a cavity with loss. Let's begin considering an optical resonator of length L with a lossy medium α of length l illustrated in Fig. 28.

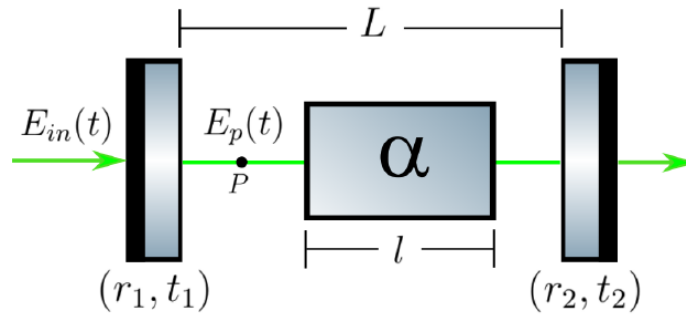
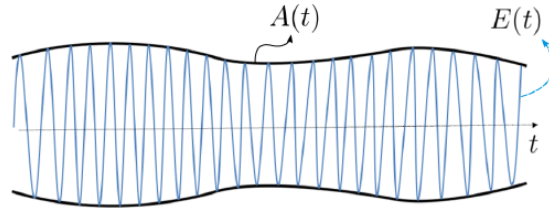


Figure 28 – Optical cavity of length L and lossy material α of length l . $E_{in}(t)$ is the input electric field and $E_p(t)$ is the electric field inside the cavity at point P .

We are going to write the scalar fields $E_{in}(t)$ and $E_p(t)$ in terms of its respective envelopes $A(t)$, pictorially illustrated in Fig. 29, as

$$E_{in}(t) = A_{in}(t)e^{-i\omega t}, \quad (3.46a)$$

$$E_p(t) = A(t)e^{-i\omega t}. \quad (3.46b)$$

Figure 29 – Envelope $A(t)$ of an electric field $E(t)$.

After a round trip time interval τ we can assume that the variation of the envelope intracavity field is negligible and the electric field at point P as [37]

$$E_p(t + \tau) = E_p(t)r_1r_2e^{-2\alpha l} + t_1E_{in}(t + \tau). \quad (3.47)$$

The term $e^{-2\alpha l}$ represents a double passage on the lossy medium, which if we assume that the losses are small we can write that $e^{-2\alpha l} \approx 1 - 2\alpha l$. Also considering high reflective mirrors we can make the approximation $r_1r_2 \approx 1 - (T_1 + T_2)/2$ [mart]. By replacing (3.46a) and (3.46b) in (3.47) we can obtain⁶

$$\frac{dA(t)}{dt} \cong -(\gamma - i\Delta)A(t) + \frac{\sqrt{T_1}}{\tau}A_{in}(t), \quad (3.48)$$

where $\gamma = \frac{2\alpha l}{\tau} + \frac{T_1+T_2}{2\tau}$.

3.4 OPO Dynamical Equations

In a $\chi^{(2)}$ nonlinear material the 3 waves involved in the process are often called pump (α_p), signal (α_s) and idler (α_i). One of the nonlinear process that is possible to occur is called parametric down conversion which can be understood as a difference-frequency generation process illustrated in the energy-level description on Fig. 15. The pump acts as the ω_1 frequency and signal and idler can be mapped with ω_2 and ω_3 waves. Once the nonlinear material is placed inside of an optical resonator we can build up large field values for signal and idler once the gains are higher than losses for those modes (oscillation condition) [41]. This device is called the OPO and is illustrated in Fig. 30 below.

⁶ Algebraic details in Appendix B

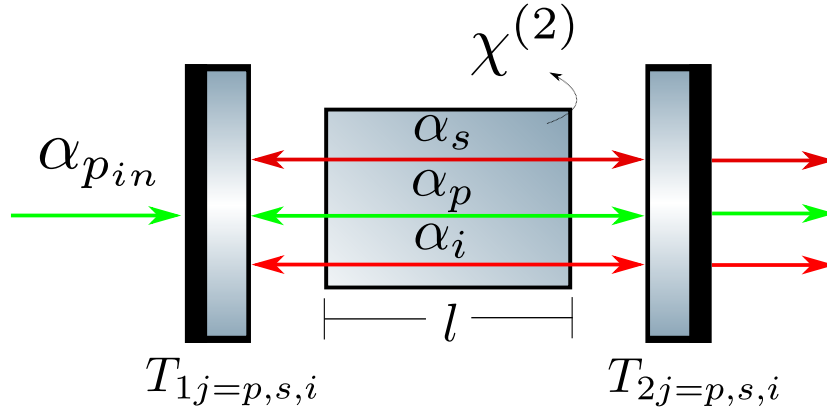


Figure 30 – Sketch of an OPO. α_{pin} is the input pump mode. α_j ($j = p, s, i$) are the three modes complex amplitudes inside the nonlinear $\chi^{(2)}$ material of length l . T_{1j} and T_{2j} are the mirrors transmission coefficients for each mode.

An approach to obtain the OPO dynamic equations is by making the assumption of the weak coupling $\chi^{(2)}$ which allow writing the amplitudes envelopes after a round trip in the cavity as [37]

$$A_j'(2l) \cong A_j(0) + 2l \frac{\partial A_j}{\partial z}, \quad (3.49)$$

where the indice $j = p, s, i$ refers to modes pump, signal and idler, respectively. The results (3.11a), (3.11b) and (3.11c) previously obtained can be replaced on the second term on the right-hand side of (3.49). By comparing the obtained result with the equation (3.48) which were also obtained after a mode round trip we obtain the OPO equations⁷ [37]

$$\dot{\alpha}_p = -(\gamma_p - i\Delta_p) \alpha_p + i\chi \alpha_s \alpha_i + \eta_p \alpha_{pin}, \quad (3.50a)$$

$$\dot{\alpha}_s = -(\gamma_s - i\Delta_s) \alpha_s + i\chi \alpha_p \alpha_i^*, \quad (3.50b)$$

$$\dot{\alpha}_i = -(\gamma_i - i\Delta_i) \alpha_i + i\chi \alpha_p \alpha_s^*. \quad (3.50c)$$

The phase match condition $\Delta k = 0$ is guaranteed. We also made the substitutions $\alpha_j = \sqrt{n_j/\omega_j} A_j$ ($j = p, s, i$), $\alpha_{pin} = \sqrt{n_p/\omega_p} A_{pin}$ and $\eta_p = \sqrt{T_p} \tau$. The coupling constant of the 3 waves is represented as $\chi = (l\chi^{(2)}/c\tau) \sqrt{\omega_p \omega_s \omega_i / n_p n_s n_i}$. The quantities $\gamma_j = (4\alpha_j l + T_{1j} + T_{2j})/2\tau$ and $\Delta_j = \varphi_j - 2\pi n$ ($j = p, s, i$ and n is a integer) represents, respectively, the losses and detuning for each mode. The detuning can be understood as the phase difference of a given mode ω_j to its nearest frequency resonance mode ω_n .

⁷ further mathematical details in the appendix B

To get a better feeling of the OPO equations we are going to discuss the concept of oscillation threshold, which is the minimum intensity value of the input pump mode capable to generate the down-converted beams signal and idler. In other words, above-threshold, we have no null solution for α_s and α_i . We can obtain an expression for the threshold from the steady state solution. In order to achieve it, let's assume $\dot{a}_p = \dot{a}_s = \dot{a}_i = 0$, $\Delta_s = \Delta_i = \Delta$ and $\gamma_s = \gamma_i = \gamma$. From Equations (3.50a), (3.50b) and (3.50c) we have

$$(\gamma_p - i\Delta_p) \alpha_p = i\chi\alpha_s\alpha_i + \eta_p\alpha_{p_{in}}, \quad (3.51a)$$

$$(\gamma - i\Delta) \alpha_s = i\chi\alpha_p\alpha_i^*, \quad (3.51b)$$

$$(\gamma - i\Delta) \alpha_i = i\chi\alpha_p\alpha_s^*. \quad (3.51c)$$

Multiplying the complex conjugate of (3.51c) by the (3.51b) we have

$$(\gamma - i\Delta)(\gamma + i\Delta) = \chi^2|\alpha_p|^2 \longrightarrow |\alpha_p|^2 = \frac{\gamma^2 + \Delta^2}{\chi^2}. \quad (3.52)$$

The result (3.52) shows that the intracavity pump power is "clipped": above-threshold is always the same. Also, writing each mode as $\alpha_j = |\alpha_j|e^{i\theta_j}$ ($j = p, s, i$) we can obtain from (3.51b) and (3.51c) that $\theta_p = \theta_s + \theta_i$. By conveniently setting $\theta_p = \theta_{p_{in}} = 0$ and considering that the down-converted modes intensities is given by $I = |\alpha_s||\alpha_i|$ (for $|\alpha_s| = |\alpha_i|$) we can obtain from (3.51b) and (3.51a) that

$$I = \frac{1}{\chi} \left[\frac{(\gamma_p - i\Delta_p)(\gamma - i\Delta)}{i\chi} - \eta_p\alpha_{p_{in}} \right] \quad (3.53)$$

which means that the production of the down-converted beams ($I > 0$) must obey the threshold condition

$$\alpha_{p_{in\ th}} > \frac{(\gamma_p - i\Delta_p)(\gamma - i\Delta)}{i\eta_p\chi} \longrightarrow |\alpha_{p_{in}}|_{th}^2 > \frac{(\gamma_p^2 + \Delta_p^2)(\gamma^2 + \Delta^2)}{(\eta_p\chi)^2}. \quad (3.54)$$

This last result (3.54) imposes the minimum input pump intensity $|\alpha_{p_{in}}|_{th}^2$ necessary to produce signal and idler.

The numerical integration of the OPO time evolution equations, above-threshold, is displayed in Fig. 31. From it, we can notice a transient behavior of the amplitudes of the 3 modes involved on the nonlinear process, before achieving the steady-state.

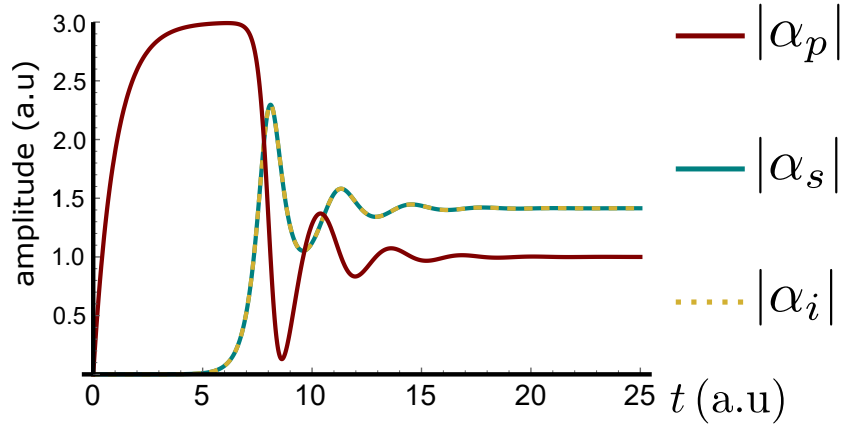


Figure 31 – OPO time evolution above-threshold. $\alpha_{pin} = 3$, $\gamma_p = \gamma = 1$, $\Delta_p = \Delta = 0$, $\chi = 1$ and $\eta_p = 1$. The threshold, therefore, is $|\alpha_{pin}|_{th} = 1$. All parameters are in arbitrary units (a.u.).

The intensity simulation of pump, signal and idler as a function of the input pump mode $|\alpha_{pin}|^2$ is displayed in Fig. 32. From this figure, we can clearly observe that below-threshold (in this simulation $|\alpha_{pin}|_{th}^2 = 1$ (a.u)) we have that both $|\alpha_s|^2 = |\alpha_i|^2 = 0$. Once the threshold is overcome, we have production of both signal and idler. The clipping value ($|\alpha_p|^2 = 1$) can also be observed in Fig. 32. Above-threshold the pump intensity is $|\alpha_p|^2 = 1$ (a.u) independently of the input pump power.

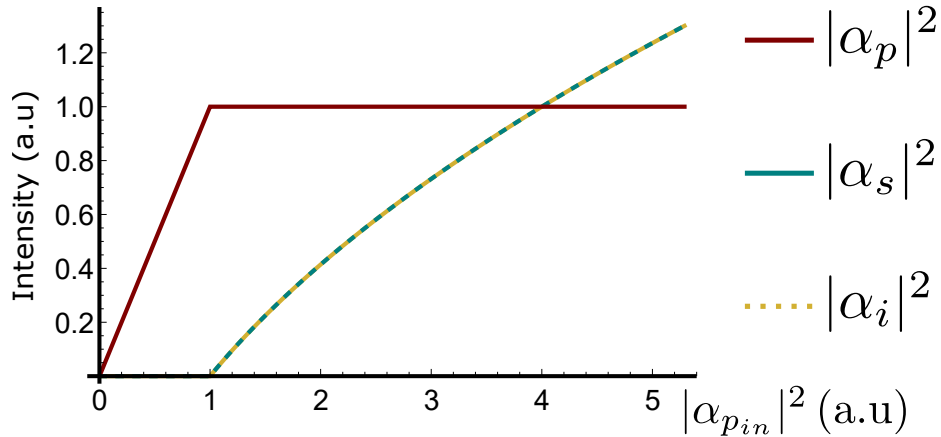


Figure 32 – Steady-state solutions intensities in OPO. $\gamma_p = \gamma = 1$, $\Delta_p = \Delta = 0$, $\chi = 1$ and $\eta_p = 1$. The threshold, therefore, is $|\alpha_{pin}|_{th} = 1$. All parameters are in arbitrary units (a.u.).

3.4.1 OPA Dynamical Equations

In this present work, our theoretical predictions are made by considering an OPO under injection. This will give rise to an OPA, which is a frequency-difference process, previously discussed in an energy-level description in the Fig. 15. In the OPA process we will consider a seed mode expressed by the complex amplitude $\alpha_{s_{in}}$. This last one will be amplified and give rise to the signal mode. On the other hand, the idler mode will be stimulated on the process. The dynamical equations of the OPA are

$$\dot{\alpha}_p = -(\gamma_p - i\Delta_p)\alpha_p + i\chi\alpha_s\alpha_i + \eta_p\alpha_{p_{in}}, \quad (3.55a)$$

$$\dot{\alpha}_s = -(\gamma_s - i\Delta_s)\alpha_s + i\chi\alpha_p(\alpha_i)^* + \eta\alpha_{s_{in}} \quad (3.55b)$$

$$\dot{\alpha}_i = -(\gamma_i - i\Delta_i)\alpha_i + i\chi\alpha_p(\alpha_s)^*. \quad (3.55c)$$

The numerical integration of the OPA time evolution equations is displayed in Fig. 33. As we can observe, in this injected regime situation we will have no longer a threshold condition in order to produce the down-converted modes signal and idler. This can also be observed in the intensity graph simulation of the 3 modes as function of the input pump, on Fig. 34.

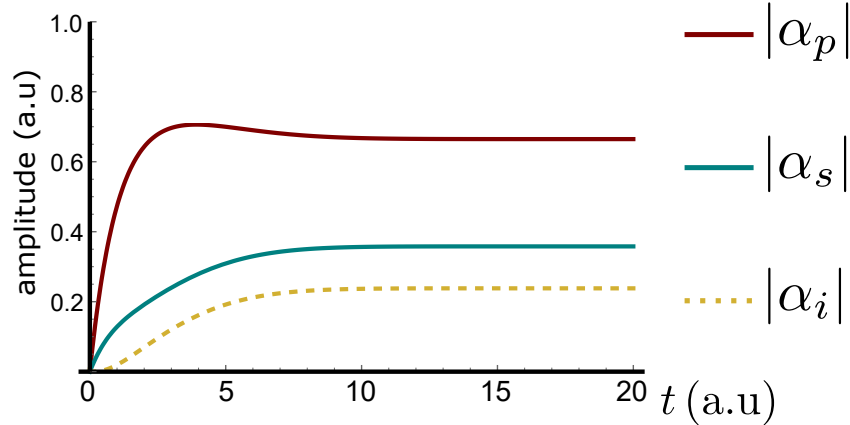


Figure 33 – OPA time evolution below-threshold. $\alpha_{p_{in}} = 0.75$, $\alpha_{s_{in}} = 0.20$, $\gamma_p = \gamma = 1.0$, $\Delta_p = \Delta = 0$, $\eta_p = \eta = 1.0$ and $\chi = 1.0$. The threshold is $|\alpha_{p_{in}}|_{th} = 1.0$.

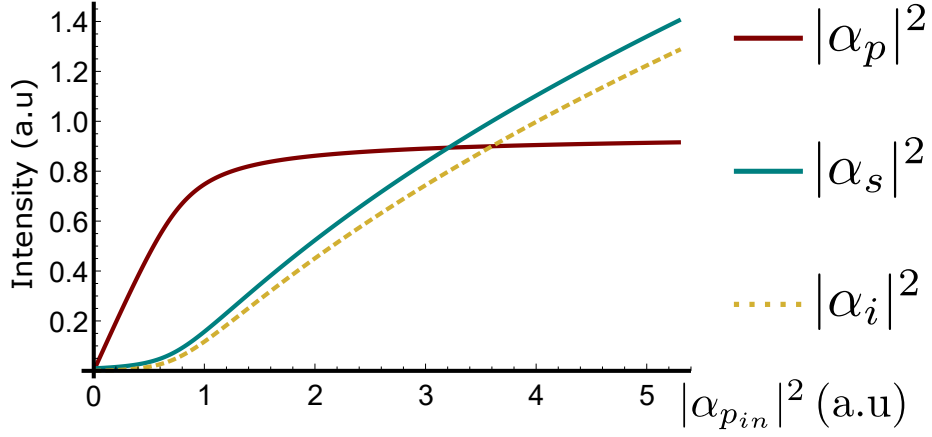


Figure 34 – Steady-state solutions intensities in OPA. $\alpha_{sin} = 0.10$, $\gamma_p = \gamma = 1.0$, $\Delta_p = \Delta = 0$, $\eta_p = \eta = 1.0$ and $\chi = 1.0$.

3.4.2 Dynamical Equations for Transverse Modes

When considering the transverse structure of light the OPO dynamical equations get more complex. In this work, we are going to write the modes on the LG basis $\psi^{\mathbf{lq}}$, where \mathbf{l} is the topological charge and \mathbf{q} is the radial order, as

$$\mathcal{E}_j(\mathbf{r}) = \sum_{\mathbf{lp}} \alpha_j^{\mathbf{lp}} \psi^{\mathbf{lp}}(\mathbf{r}), \quad (3.56)$$

where the index $j = p, s, i$ refers to pump, signal and idler. Making those assumptions, the OPO dynamical equations for transverse modes are

$$\dot{\alpha}_p^{\mathbf{lp}} = -(\gamma_p - i\Delta_p) \alpha_p^{\mathbf{lp}} + i\chi \sum_{mq, nr} I_{pqr}^{lmn} \alpha_s^{\mathbf{mq}} \alpha_i^{\mathbf{nr}} + \eta_p \alpha_{pin}^{\mathbf{lp}}, \quad (3.57a)$$

$$\dot{\alpha}_s^{\mathbf{mq}} = -(\gamma_s - i\Delta_s) \alpha_s^{\mathbf{mq}} + i\chi \sum_{lp, nr} \left(I_{pqr}^{lmn} \right)^* \alpha_p^{\mathbf{lp}} (\alpha_i^{\mathbf{nr}})^*, \quad (3.57b)$$

$$\dot{\alpha}_i^{\mathbf{nr}} = -(\gamma_i - i\Delta_i) \alpha_i^{\mathbf{nr}} + i\chi \sum_{lp, mq} \left(I_{pqr}^{lmn} \right)^* \alpha_p^{\mathbf{lp}} (\alpha_s^{\mathbf{mq}})^*. \quad (3.57c)$$

The term I_{pqr}^{lmn} represents an effective coupling constant and is defined as

$$I_{pqr}^{lmn} = \int_{-l/2}^{l/2} dz e^{i\Delta kz} \Lambda_{pqr}^{lmn}(z), \quad (3.58)$$

where l is the crystal length and $\Lambda_{pqr}^{lmn}(z)$ is the transverse coupling previous discussed (3.17).

In principle, the transverse mode dynamics involves an infinite set of coupled equations mediated by the coupling constants I_{pqr}^{lmn} . However, the spatial transverse overlap Λ_{pqr}^{lmn} restrict the nonvanishing transverse modes to a finite set

[43]. This means that the pump beam can excite many different transverse modes for signal and idler, but in general it is the one with the lowest threshold that survives [42]. On other words, the effective coupling is inversely proportional to the threshold, according to [43]

$$|\alpha_{p_{in}}|_{th}^2 > \frac{(\gamma_p^2 + \Delta_p^2)(\gamma^2 + \Delta^2)}{(\eta_p \chi)^2 |I_{pqr}^{lmn}|^2}. \quad (3.59)$$

In this present work, we calculated the transverse overlaps between pump, signal and idler based in Ref. [43]. The results are family independent, which means, either LG or HG modes rely on the same conclusions. Basically, the procedure is to plug the solutions for LG modes (2.13) (or HG modes (2.11)) into the transverse overlap expressions (3.17). Also, they are considering that $\Delta k \ll k_p$ (Δk is the phase-mismatch and k_p is the pump wave number) and $l \lesssim z_R$, which is frequently the case for the experimental conditions. After some algebraic calculations we obtain general constraints regarding the transverse mode coupling in three-wave mixing

$$\begin{aligned} S_p + S_s + S_i &\equiv 0 \pmod{2}, \\ S_p &\leq S_s + S_i, \end{aligned} \quad (3.60)$$

where S_j ($j = p, s, i$) are the modes orders. $S = |l| + 2q$ for LG modes and $S = m + n$ for HG. Also, we can rewrite the effective coupling constant I_{pqr}^{lmn} as

$$I_{pqr}^{lmn} = z_R \left(\int_{-l/2z_R}^{l/2z_R} du \frac{e^{i(\Delta k z_R)u}}{1 - iu} \left[\frac{1 + iu}{\sqrt{1 + u^2}} \right]^{\Delta k} \right) \Lambda_{pqr}^{lmn}(0), \quad (3.61)$$

where we defined $u = z/z_R$. The term between parentheses can be viewed as an overall conversion efficiency, since it does not make explicit reference to the particular modes being coupled, except for the mode order difference $\Delta S = S_p - S_s - S_i$. This means that the second factor $\Lambda_{pqr}^{lmn}(0)$ is the relevant for fixed ΔS .

The theory developed in this thesis deals with an OPA process. This means that we are not only pumping the OPO cavity but also injecting a seed beam. This last one will be amplified giving rise to the signal mode. Both of them (pump and injection) have fixed transverse structure. This means that the idler mode will be stimulated according to the biggest $\Lambda_{pqr}^{lmn}(0)$ values. In Fig.35 we show some coupling values examples where we have fixed the parameters l and p for the pump, and m and q for the signal. Since we are considering OAM

conservation the n parameter for the idler is also fixed so we run the graphs as a function of the r values.

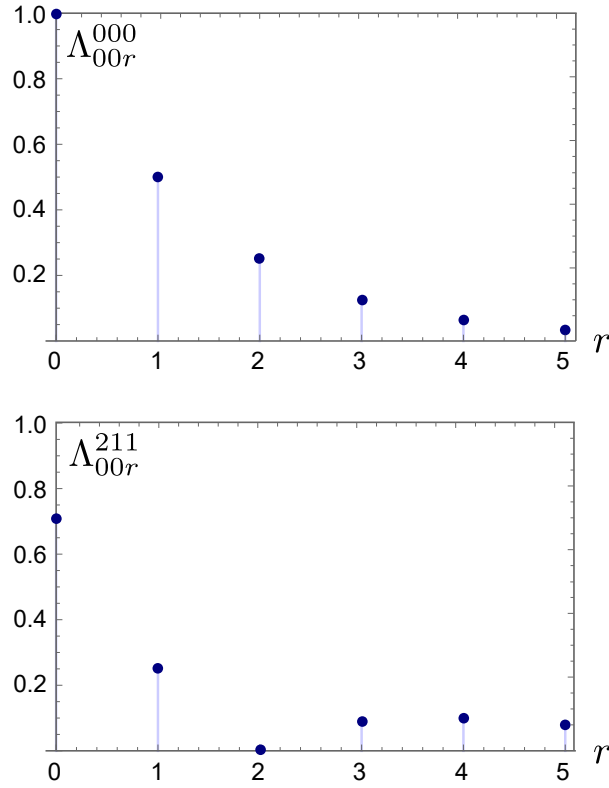


Figure 35 – Transverse overlaps values at $z = 0$. In top we have both pump and signal modes at Gaussian ψ^{00} transverse structure and idler running over ψ^{0r} . At the bottom the pump is in a second-order LG mode ψ^{+20} and signal at ψ^{+10} first-order. The possible structures for the idler are ψ^{+1r} .

In order to achieve a better physical feeling of the different overlaps values we are going to explore how the amplitudes evolve in time and how the modes intensities evolve with the input pump intensity for the steady-state solutions. Now, let's expose the triple resonance dynamical equations for the configurations we are considering in Fig.35. For the case where we have both pump and signal at Gaussian mode ψ^{00} the OPA equations are

$$\begin{aligned}
 \dot{\alpha}_p^{00} &= -\gamma_p \alpha_p^{00} + i\chi \Lambda_{000}^{000} \alpha_s^{00} \alpha_i^{00} + i\chi \Lambda_{001}^{000} \alpha_s^{00} \alpha_i^{01} + \eta_p \alpha_{pin}^{00}, \\
 \dot{\alpha}_s^{00} &= -\gamma \alpha_s^{00} + i\chi \left(\Lambda_{000}^{000} \right)^* \alpha_p^{00} \left(\alpha_i^{00} \right)^* + i\chi \left(\Lambda_{001}^{000} \right)^* \alpha_p^{00} \left(\alpha_i^{01} \right)^* + \eta_p \alpha_{sin}^{00}, \\
 \dot{\alpha}_i^{00} &= -\gamma \alpha_i^{00} + i\chi \left(\Lambda_{000}^{000} \right)^* \alpha_p^{00} \left(\alpha_s^{00} \right)^*, \\
 \dot{\alpha}_i^{01} &= -\gamma \alpha_i^{01} + i\chi \left(\Lambda_{001}^{000} \right)^* \alpha_p^{00} \left(\alpha_s^{00} \right)^*.
 \end{aligned} \tag{3.62a}$$

In Fig.36, we have the OPA time evolution for both pump and injection at ψ^{00} . The biggest overlap is value is $\Lambda_{000}^{000} = 1$, which represents all three modes in Gaussian structure ψ^{00} . The second biggest overlap value is $\Lambda_{001}^{000} = 0.5$, which represents both pump and injection at ψ^{00} and idler at ψ^{01} . This difference in the overlap values is evident from the dashed curves in Fig.36. We can see from it that the amplitude $|\alpha_i^{00}|$ get bigger in time in relation to $|\alpha_i^{01}|$. Similar conclusions can be observed in Fig.37 but in terms of the intensities. Let's recall that in this case, the solutions are in steady-state.

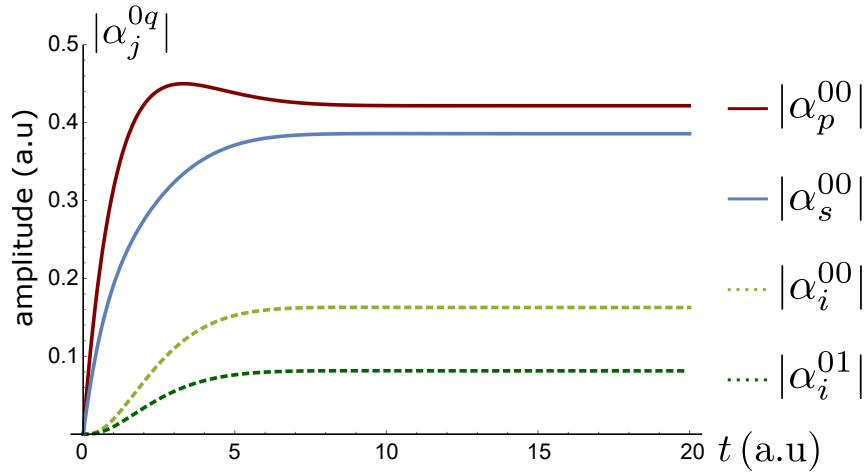


Figure 36 – OPA time evolution below-threshold for both pump and injection at ψ^{00} . The OPA and cavities parameters are $\alpha_{pin}^{00} = 0.5$, $\alpha_{sin}^{00} = 0.3$, $\Lambda_{000}^{000} = 1$, $\Lambda_{001}^{000} = 0.5$, $\gamma_p = \gamma = 1$, $\Delta_p = \Delta = 0$, $\chi = 1$, $\eta_p = 1$. The threshold, therefore, is $|\alpha_{pin}|_{th} = 1$.

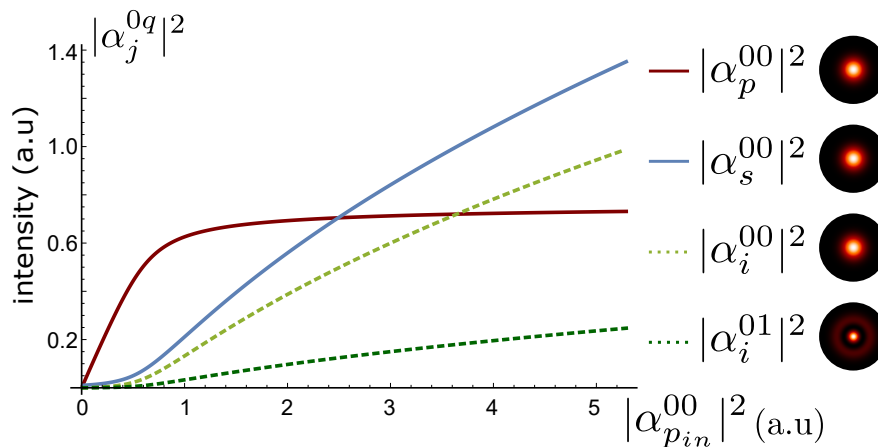


Figure 37 – OPA intensity evolution in steady-state for both pump and injection at ψ^{00} . The OPA and cavity parameters are $\alpha_{sin}^{00} = 0.1$, $\Lambda_{000}^{000} = 1$, $\Lambda_{001}^{000} = 0.5$, $\gamma_p = \gamma = 1$, $\Delta_p = \Delta = 0$, $\chi = 1$ and $\eta_p = 1$.

For the case where we have the pump at ψ^{+20} and the injected signal mode at ψ^{+10} the triple resonant dynamical equations are

$$\begin{aligned}
\dot{\alpha}_p^{+20} &= -\gamma_p \alpha_p^{+20} + i\chi \Lambda_{000}^{211} \alpha_s^{+10} \alpha_i^{+10} + i\chi \Lambda_{001}^{211} \alpha_s^{+10} \alpha_i^{+11} + \eta_p \alpha_{pin}^{+20}, \\
\dot{\alpha}_s^{+10} &= -\gamma \alpha_s^{+10} + i\chi \left(\Lambda_{000}^{211}\right)^* \alpha_p^{+20} \left(\alpha_i^{+10}\right)^* + i\chi \left(\Lambda_{001}^{211}\right)^* \alpha_p^{+20} \left(\alpha_i^{+11}\right)^* + \eta_p \alpha_{sin}^{+10}, \\
\dot{\alpha}_i^{+10} &= -\gamma \alpha_i^{+10} + i\chi \left(\Lambda_{000}^{211}\right)^* \alpha_p^{+20} \left(\alpha_s^{+10}\right)^*. \\
\dot{\alpha}_i^{+11} &= -\gamma \alpha_i^{+11} + i\chi \left(\Lambda_{001}^{211}\right)^* \alpha_p^{+20} \left(\alpha_s^{+10}\right)^*.
\end{aligned} \tag{3.63a}$$

In Fig.38 we have the OPA time evolution for pump at ψ^{+20} and injection at ψ^{+10} . The biggest overlap is value is $\Lambda_{000}^{211} = 1/\sqrt{2}$, which represents pump at ψ^{+20} , signal at ψ^{+10} and idler at ψ^{+10} . The second biggest overlap value is $\Lambda_{001}^{211} = 1/4$, which represents pump and signal with same structures as before but idler at ψ^{+11} . This difference in the overlap values is evident from the dashed curves in Fig.38. We can see from it that the amplitude $|\alpha_i^{+10}|$ get bigger in time in relation to $|\alpha_i^{+11}|$. Similar conclusions can be observed in Fig.39 but in terms of the intensities. Let's recall that in this case, the solutions are in steady-state.

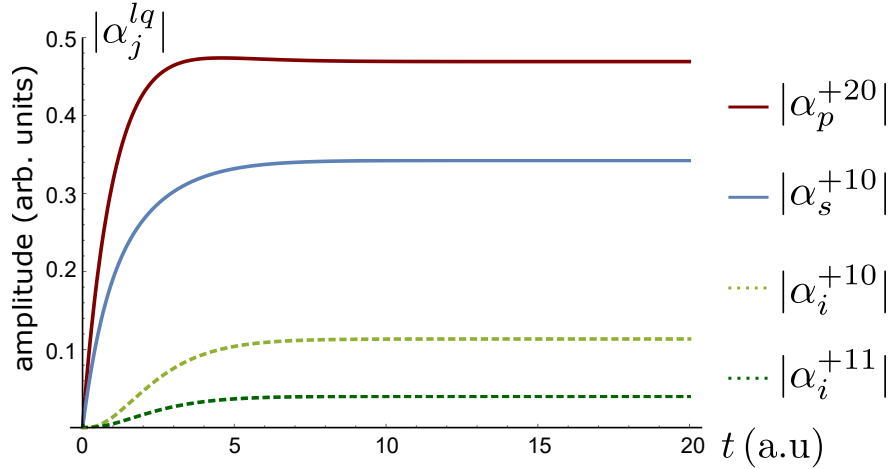


Figure 38 – OPA time evolution below-threshold for pump at ψ^{+20} and injection at ψ^{+10} . The OPA and cavities parameters are $\alpha_{pin}^{+20} = 0.5$, $\alpha_{sin}^{+10} = 0.3$, $\Lambda_{000}^{211} = 1/\sqrt{2}$, $\Lambda_{001}^{211} = 1/4$, $\gamma_p = \gamma = 1$, $\Delta_p = \Delta = 0$, $\chi = 1$, $\eta_p = 1$. The threshold, therefore, is $|\alpha_{pin}|_{th} = \sqrt{2}$.

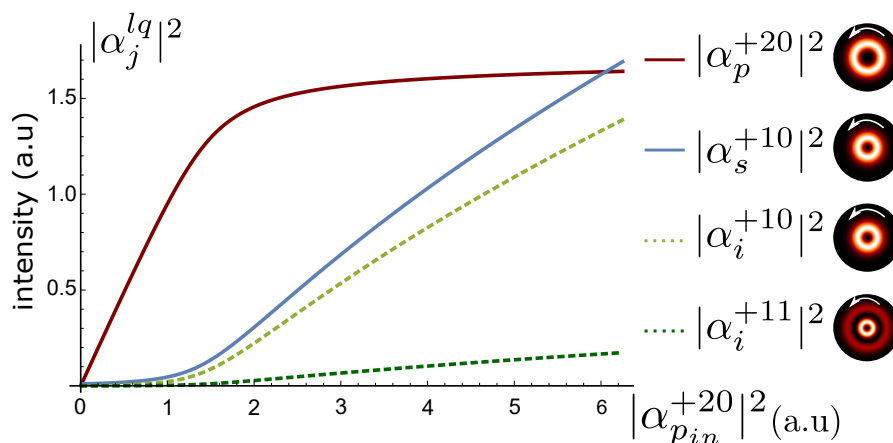


Figure 39 – OPA intensity evolution in steady-state for pump ψ^{+20} and injection at ψ^{+10} . The OPA and cavity parameters are $\alpha_{sin}^{00} = 0.1$, $\Lambda_{000}^{211} = 1/\sqrt{2}$, $\Lambda_{001}^{211} = 1/4$, $\gamma_p = \gamma = 1$, $\Delta_p = \Delta = 0$, $\chi = 1$ and $\eta_p = 1$.

3.4.3 Astigmatism effect in the OPO

In this section, we are going to talk about a very important topic when working with birefringent crystals, such as the KTP: Astigmatism. In an experiment, this effect can be very challenging to deal with for reasons we are about to discuss. As we have seen, in anisotropic media we have two distinct phase velocities for a given propagation direction. Each of those is associated with an extraordinary (e) wave and ordinary (o) wave. We are going to consider a wave traveling along the crystal as illustrated in Fig.20. With that being considered a rotated frame (x', y', z) can be used to describe the propagation inside the crystal.

At this point, is important to distinguish an effective wavenumber associated with those waves, that means, define a $k_{eff} = n_{0(e)}^{y'(z)} k$ for each polarization (ordinary and extraordinary) and transverse direction (y' and z) [42]. k is the wave number in vacuum. Physically, those distinct wavenumbers mean that the OPO cavity length L is distinct for each transverse directions and polarization. The effective cavity length L for each case is [42]

$$L = L_0 - l \left(\frac{k_{eff} - k}{k_{eff}} \right), \quad (3.64)$$

where L_0 is the cavity mirrors separations, l is the crystal length. The importance of this different cavity length L is in the Gouy phase shift. The Gouy phase acquired in the propagation equivalent to a round trip is calculated as $\Phi_{o(e)}^{y'(z)} = 4 \arctan \left(\frac{\sqrt{L}/\sqrt{2R-L}}{\sqrt{L}/\sqrt{2R-L}} \right)$, where L is the effective cavity length in Equation (3.64) and R is the mirrors radius of curvature.

Typically, the Gouy phase difference for the ordinary polarization is more relevant, that means, we can neglect this phase shift for the extraordinary waves [42]. The transverse structure also plays an important role in astigmatism, since the Gouy phase depends on its order as shown in Equations (2.12) and (2.14). For a Hermite-Gauss mode ψ_{HG}^{nm} the total Gouy phase added in a round trip on the OPO cavity is given by [42]

$$\Phi = (m + 1/2)\Phi^z + (n + 1/2)\Phi^{y'}, \quad (3.65)$$

As an example, if we pump a OPO cavity with a first-order Laguerre-Gauss mode ψ_{LG}^{10} we can notice an interesting physical consequence of astigmatism. Let's recall that we can relate first-order modes as $\psi_{LG}^{10} = (\psi_{HG}^{10} - i\psi_{HG}^{01})/\sqrt{2}$ (for superior order modes we can make use of Eq.(2.15)). From Equation (3.65) we can see that a phase difference between the ψ_{HG}^{01} and ψ_{HG}^{10} will occur. This phase different will result in a splitting of the resonance position. As we already mention, this splitting due to astigmatism is more relevant in the ordinary polarization as represented in Fig.40 [42]. A sketch of a first-order LG at diagonal polarization passing through a KTP crystal is shown in Fig.41. We can also check, according to Equation (3.65), that this astigmatism effect get more crucial for superior order modes. In a experiment this can be very challenging to deal with.

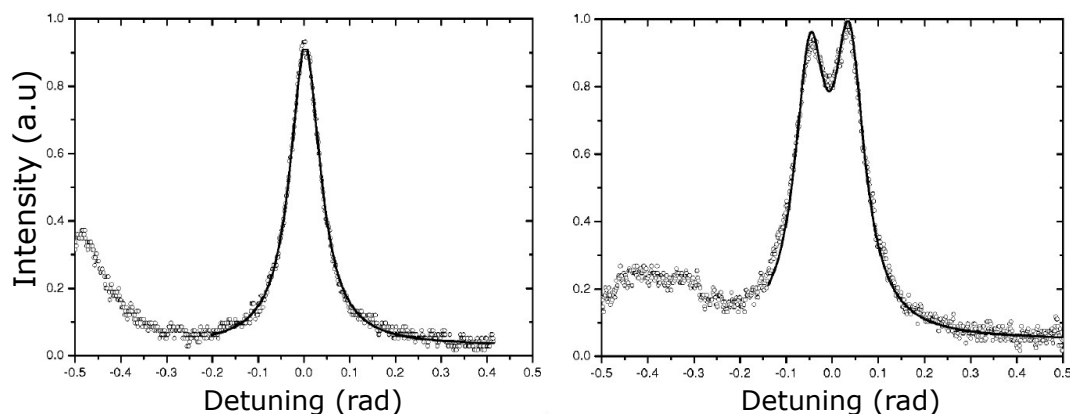


Figure 40 – Cavity resonance peak for a pump LG beam with extraordinary polarization (left) and ordinary polarization (right). In the ordinary wave the resonance peak splits in two, clearly showing the symmetry breaking between the two HG components of the LG beam. The OPO cavity parameters are $L_0 = 17.4$ mm, $l = 10.0$, mm. At 1064nm this peak separation is about 82 mrad.

From this analysis we conclude that the OPO can support the oscillation of an LG mode for the extraordinary wave, since its HG components have a

degenerate (or quasidegenerate) resonance frequency. On the other hand, an LG mode in the ordinary wave cannot operate because its HG components will not have the same resonance frequency. A more complete discussion about the OAM transfer from the pump to the down-converted modes in a spontaneous process can be found in [42, 43].

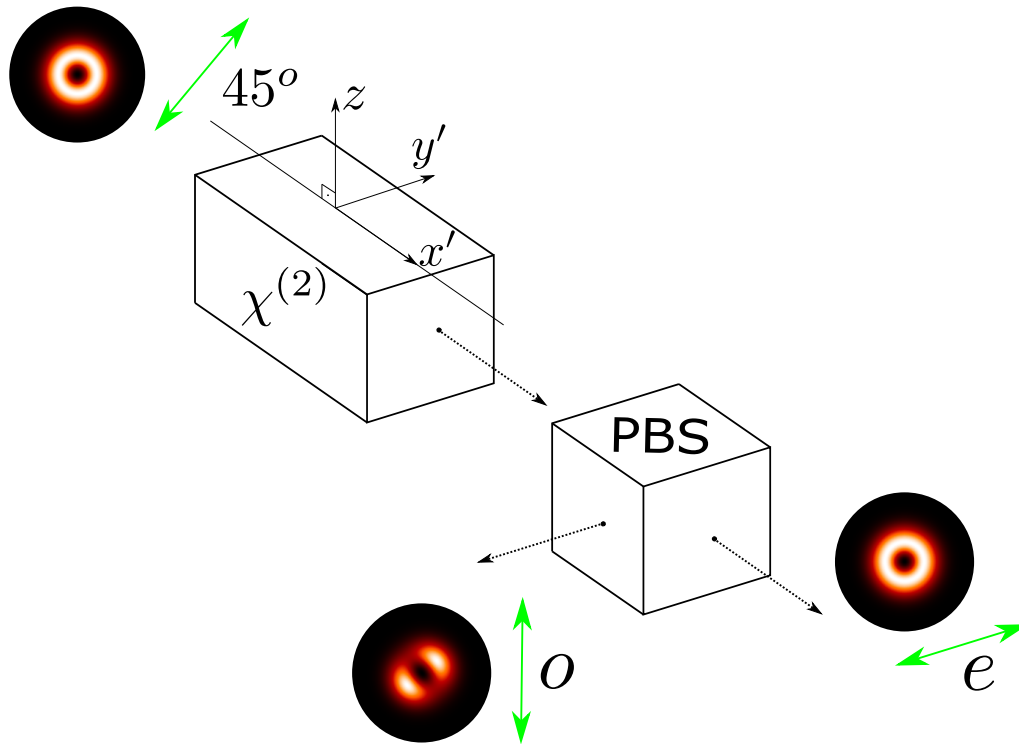


Figure 41 – Sketch of a first-order LG mode with polarization at 45° passing through a KTP. With a PBS we can separate the ordinary (vertical) and extraordinary (horizontal) polarizations. The ordinary wave experience the astigmatism more crucial, while the effect can be neglected to the extraordinary wave.

4 Generalized OAM Symmetry in Parametric Amplification

In this chapter, we are going to discuss in detail the novelty that this thesis brings to the literature [25]. This novelty consists of a study of OAM symmetry between the down-converted beams produced in a parametric amplification process. This symmetry can be understood in terms of the well-known Poincaré sphere representation for transverse modes. For first-order modes this symmetry were proposed and experimentally demonstrated in [26, 51].

In this work, we investigate how this Poincaré sphere symmetry extends to higher-orders. In principle, this subject suggests a difficult task, since higher-order modes do not have a simple geometric representation. However, the selection rules that arise from the spatial overlap between the interacting modes impose restrictions that limit the symmetry properties to two-dimensional subspaces of the higher-order mode structure. The Poincaré symmetry is independently verified inside each subspace, what can be useful for parallel control of independent down-conversion channels. Here, we will focus on the classical behaviour of the mode dynamics, which will serve as a starting point for a future investigation in the quantum domain. As we will see, this classical instance of the problem already encompasses a rich dynamics.

4.1 Structured Light Injection in Parametric Amplification

Let's begin assuming a parametric amplification process in a second-order nonlinear crystal. We are considering two input beams, *pump* (ω_p) and *signal* (ω_s), whose interaction results in a third mode *idler* (ω_i). In this nonlinear process we have energy conservation $\omega_p = \omega_s + \omega_i$. The physical situation is illustrated in Fig. 42. A pump beam is sent to the OPO cavity along with a seed beam that matches the signal frequency and polarization. Inside the resonator, the pump energy is transferred to signal and idler, which, under type-II phase-matching, is generated with its polarization orthogonal to the signal beam.

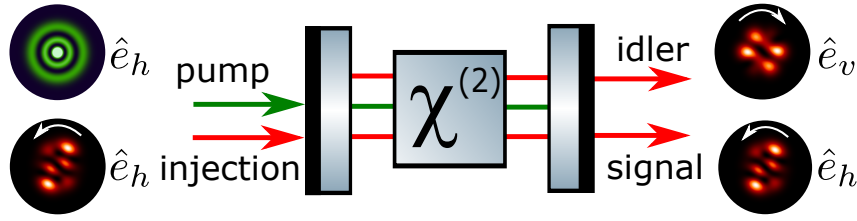


Figure 42 – Sketch of the optical parametric oscillator with type-II phase-matching and structured light injection. \hat{e}_h and \hat{e}_v are the horizontal and vertical polarization unit vectors, respectively. The pump beam can be radially structured to optimize the spatial overlap with signal and idler.

We are interested in deriving general symmetry properties carried by the signal and idler beams as a result of the nonlinear coupling. This kind of symmetry has already been investigated, both theoretical [51] and experimentally [26], for first-order modes, where OAM conservation and intensity overlap were the main features behind the symmetry observed. Our objective is to extend these symmetry properties to higher order modes injected in the OPO.

The seed beam is assumed to be structured with an arbitrary superposition of Laguerre-Gaussian (LG) modes of the same order N_s , while the pump beam is assumed to be in a single LG mode without OAM. In the LG basis, the pump and seed electric fields can be written as

$$\begin{aligned}\mathcal{E}_{pin}(\mathbf{r}) &= \alpha_{pin} \psi^{0q_p}(\mathbf{r}), \\ \mathcal{E}_{sin}(\mathbf{r}) &= \sum_l \alpha_{sin}^{lq_s} \psi^{lq_s}(\mathbf{r}),\end{aligned}\quad (4.1)$$

where $\psi^{lq}(\mathbf{r})$ is a LG mode (2.13) with topological charge (OAM) l and radial index q , α_{sin}^{lq} is the corresponding complex amplitude of the signal mode and α_{pin} is the input pump complex amplitude. The summation over the seed modes is constrained by $2q_s + |l| = N_s$. The choice of a fixed order for the seed beam is of experimental relevance, since in this case all components evolve with the same Gouy phase and can be simultaneously mode matched to the OPO cavity.

4.1.1 Dynamical Equations and Steady State Solution

The terms (4.1) act as source terms of the dynamical equations. The intracavity electric fields, therefore, are also on the LG basis and is written as

$$\begin{aligned}\mathcal{E}_p(\mathbf{r}) &= \alpha_p \psi^{0q_p}(\mathbf{r}), \\ \mathcal{E}_j(\mathbf{r}) &= \sum_l \alpha_j^{lq_j} \psi^{lq_j}(\mathbf{r}),\end{aligned}\quad (4.2)$$

where the index $j = s, i$ refers to signal and idler, respectively. The stimulated idler beam will populate the LG modes with optimal overlap

$$\Lambda_{q_s q_i}^l = \int [\psi^{0q_p}(\mathbf{r})]^* \psi^{lq_s}(\mathbf{r}) \psi^{-lq_i}(\mathbf{r}) d^2\mathbf{r}, \quad (4.3)$$

with the pump and seed modes. This imposes OAM conservation $l_s + l_i = l_p$ and restricts the radial indices as well. Since the pump beam is assumed to carry zero OAM, the coupled signal and idler modes must have opposite topological charges. However, the radial mode selection for the idler beam is not so simple. It is determined by the maximum overlap with the pump and seed modes. This point will be clarified in our numerical examples.

Assuming the perfect resonance of the three fields ($\Delta_p = \Delta_s = \Delta_i = 0$), the dynamical equations for the intracavity mode amplitudes are

$$\begin{aligned}\dot{\alpha}_p &= -\gamma_p \alpha_p + i\chi \sum_l \Lambda_{q_s q_i}^l \alpha_s^{lq_s} \alpha_i^{-lq_i} + \eta_p \alpha_{p_{in}}, \\ \dot{\alpha}_s^{lq_s} &= -\gamma \alpha_s^{lq_s} + i\chi \Lambda_{q_s q_i}^{l*} \alpha_p (\alpha_i^{-lq_i})^* + \eta \alpha_{s_{in}}^{lq_s}, \\ \dot{\alpha}_i^{lq_i} &= -\gamma \alpha_i^{lq_i} + i\chi \Lambda_{q_s q_i}^{l*} \alpha_p (\alpha_s^{-lq_s})^*,\end{aligned}\quad (4.4)$$

where χ is the nonlinear coupling constant, γ_p is the pump decay rate, γ is the common decay rate of signal and idler, η_p and η are the pump and signal input transmissions, respectively. We recall that the mode indices l and q_s run over the allowed values compatible with the seed order $N_s = 2q_s + |l|$, while the stimulated idler beam will carry the LG modes with optimal overlap with the pump and seed modes.

Our analysis is significantly simplified when we define the normalized variables

$$\begin{aligned}\beta_p &= \chi \alpha_p / \gamma, \quad \beta_{p_{in}} = \chi \eta_p \alpha_{p_{in}} / \gamma^2, \\ \beta_s^{lq_s} &= \chi \alpha_s^{lq_s} / \gamma, \quad \beta_{s_{in}}^{lq_s} = \chi \eta \alpha_{s_{in}}^{lq_s} / \gamma^2, \\ \beta_i^{lq_i} &= \chi \alpha_i^{lq_i} / \gamma.\end{aligned}\quad (4.5)$$

With the normalized variables, the dynamical equations become

$$\dot{\beta}_p = -\gamma_r \beta_p + i \sum_l \Lambda_{q_s q_i}^l \beta_s^{l q_s} \beta_i^{-l q_i} + \beta_{p_{in}}, \quad (4.6)$$

$$\dot{\beta}_s^{l q_s} = -\beta_s^{l q_s} + i \Lambda_{q_s q_i}^{l*} \beta_p \left(\beta_i^{-l q_i} \right)^* + \beta_{s_{in}}^{l q_s}, \quad (4.7)$$

$$\dot{\beta}_i^{l q_i} = -\beta_i^{l q_i} + i \Lambda_{q_s q_i}^{l*} \beta_p \left(\beta_s^{-l q_s} \right)^*, \quad (4.8)$$

where derivatives in the left-hand-side are taken with respect to the dimensionless time $\tau = \gamma t$ and we introduced the decay ratio $\gamma_r = \gamma_p / \gamma$.

The steady-state solutions of the equations above allow us to analyze the solutions for the modes involved in the OPA process. By setting the time derivatives equal to zero in the left-hand-side ($\dot{\beta}_p = \dot{\beta}_s^{l q_s} = \dot{\beta}_i^{l q_i} = 0$) of (4.7) and (4.8) we can obtain from the latest equations that

$$\begin{aligned} \beta_s^{l q_s} &= \frac{\beta_{s_{in}}^{l q_s}}{1 - \left| \Lambda_{q_s q_i}^l \beta_p \right|^2}, \\ \beta_i^{l q_i} &= \frac{i \beta_p \Lambda_{q_s q_i}^{l*} \left(\beta_{s_{in}}^{-l q_s} \right)^*}{1 - \left| \Lambda_{q_s q_i}^l \beta_p \right|^2}. \end{aligned} \quad (4.9)$$

These equations can be plugged into the steady state condition for the intracavity pump amplitude, resulting in

$$\left[\gamma_r + \sum_l \frac{\left| \Lambda_{q_s q_i}^l \beta_{s_{in}}^{l q_s} \right|^2}{\left(1 - \left| \Lambda_{q_s q_i}^l \beta_p \right|^2 \right)^2} \right] \beta_p = \beta_{p_{in}}, \quad (4.10)$$

where we used $\Lambda_{q_s q_i}^{-l} = \Lambda_{q_s q_i}^l$. Without loss of generality, we may set the input pump phase equal to zero ($\alpha_{p_{in}} \in \mathbb{R}$). Therefore, the intracavity pump amplitude is also a real number that can be found by solving the quintic equation (4.10). For arbitrary mode orders, this is usually a difficult task that is beyond the scope of this work. Nevertheless, Eqs. (4.9) allow us to establish an interesting property of the down-converted beams generated by the nonlinear process, without the need of the intracavity pump solution. As we discuss next, the relationship between the amplitudes of the seed beam and the intracavity down-converted fields sets an interesting symmetry relation between signal and idler in a generalized Poincaré sphere representation of higher order modes.

4.2 Generalized Poincaré Symmetry

Previously we discussed the Poincaré sphere representation of OAM beams. As we discussed, it originally has been first introduced for first-order modes [33], represented on Fig. 6. It describes linear combinations of Laguerre-Gaussian modes with radial number $q = 0$ and topological charges $l = \pm 1$, but it can be extended to superior values of OAM, as represented on figure 7.

In this present work, we will use an independent Poincaré sphere for each two-dimensional mode space spanned by Laguerre-Gaussian beams with opposite OAM, $\psi^{\pm lq}$. For the signal beam, l and q_s run over the allowed values compatible with $2q_s + |l| = N$. For the idler beam, the radial numbers are defined by those modes with maximal spatial overlap with the pump and seed modes. Note that a zero OAM component $l = 0$ can only occur in even orders for $q_s = N/2$, while the LG modes with odd orders have $l \neq 0$. In this way, we can group the LG modes of a given order in pairs with opposite OAM $\{\psi^{\pm lq}\}$ and an isolated mode with zero OAM for even orders. For example, for seed beams with orders from 0 to 4 we have

$$\begin{aligned}
 N = 0 : & \quad \{\psi^{00}\} , \\
 N = 1 : & \quad \{\psi^{\pm 10}\} , \\
 N = 2 : & \quad \{\psi^{\pm 20}\} \oplus \{\psi^{01}\} , \\
 N = 3 : & \quad \{\psi^{\pm 30}\} \oplus \{\psi^{\pm 11}\} , \\
 N = 4 : & \quad \{\psi^{\pm 40}\} \oplus \{\psi^{\pm 21}\} \oplus \{\psi^{02}\} .
 \end{aligned} \tag{4.11}$$

Note that each $\{\psi^{\pm l|q_s}\}$ subspace realizes an independent SU(2) structure.

The idler modes will follow a similar structure. However, the corresponding radial numbers are selected by the optimal overlap with the pump and seed modes and, in general, do not fix a given order. As we will see, the Poincaré sphere symmetry previously demonstrated for first order modes in Refs. [26, 51] is independently verified within each one of the two-dimensional OAM subspaces for higher orders.

From Eqs. (4.9) we can see that the intracavity signal and idler amplitudes are related by

$$\beta_i^{lq_i} = i \beta_p \Lambda_{q_s q_i}^{l*} \left(\beta_s^{-lq_s} \right)^* . \tag{4.12}$$

For $l = 0$, there is no SU(2) structure and this equation simply states the conjugate relation between signal and idler amplitudes for the zero OAM modes.

In this case, no Poincaré symmetry can be realized. However, when $l \neq 0$, Eq. (4.12) sets a connection between the SU(2) structures of signal and idler. Let the signal input be an arbitrary structure of order $N = 2q_s + |l|$, which can be written as

$$\mathcal{E}_{sin} = \sum_{l>0} A_{in}^{lq_s} \left[\cos(\theta_l/2) \psi^{lq_s} + e^{i\phi_l} \sin(\theta_l/2) \psi^{-lq_s} \right], \quad (4.13)$$

where $\{A_{in}^{lq}\}$ are complex amplitudes and $\{(\theta_l, \phi_l)\}$ are the Poincaré sphere coordinates that represent the seed mode in each SU(2) structure $\mathcal{H}^l \equiv \{\psi^{\pm lq}\}$. For a given order N , a Poincaré sphere is associated with each OAM value l . With these definitions, the source terms that figure in the dynamical equations (4.6), (4.7), (4.8) become

$$\begin{aligned} \beta_{sin}^{lq_s} &= \frac{\chi\eta}{\gamma^2} A_{in}^{lq_s} \cos(\theta_l/2), \\ \beta_{sin}^{-lq_s} &= \frac{\chi\eta}{\gamma^2} A_{in}^{lq_s} e^{i\phi_l} \sin(\theta_l/2). \end{aligned} \quad (4.14)$$

From the steady state solution (4.9) and the signal-idler conjugation relation (4.12), we easily get

$$\begin{aligned} \beta_s^{lq_s} &= \frac{\chi}{\gamma} \xi_s^{lq_s} \cos(\theta_l/2), \quad \beta_s^{-lq_s} = \frac{\chi}{\gamma} \xi_s^{lq_s} e^{i\phi_l} \sin(\theta_l/2), \\ \beta_i^{lq_i} &= \frac{\chi}{\gamma} \xi_i^{lq_i} e^{-i\phi_l} \sin(\theta_l/2), \quad \beta_i^{-lq_i} = \frac{\chi}{\gamma} \xi_i^{lq_i} \cos(\theta_l/2), \end{aligned} \quad (4.15)$$

where

$$\begin{aligned} \xi_s^{lq_s} &= \frac{\eta A_{in}^{lq_s} / \gamma}{1 - |\Lambda_{q_s q_i}^l \beta_p|^2}, \\ \xi_i^{lq_i} &= i \beta_p \Lambda_{q_s q_i}^{l*} \left(\xi_s^{lq_s} \right)^*. \end{aligned} \quad (4.16)$$

Equations (4.15) set the Poincaré sphere symmetry between signal and idler spatial modes. Indeed, we can easily see that signal and idler coordinates on the sphere are related by

$$\begin{aligned} \theta_i^i &= \pi - \theta_i^s, \\ \phi_i^i &= \phi_i^s, \end{aligned} \quad (4.17)$$

which means that within each SU(2) structure \mathcal{H}^l , signal and idler are represented by two points on the sphere that are the specular image of each other with respect

to the equatorial plane. This is a generalization of the first-order mode symmetry previously demonstrated in Refs. [51, 26]. The intracavity signal and idler spatial modes are then given by

$$\begin{aligned}\mathcal{E}_s &= \sum_{l>0} \xi_s^{lq_s} \left[\cos(\theta_l/2) \psi^{lq_s} + e^{i\phi_l} \sin(\theta_l/2) \psi^{-lq_s} \right], \\ \mathcal{E}_i &= \sum_{l>0} \xi_i^{lq_i} \left[e^{-i\phi_l} \sin(\theta_l/2) \psi^{lq_i} + \cos(\theta_l/2) \psi^{-lq_i} \right].\end{aligned}\tag{4.18}$$

We next discuss some examples which allow us to visualize the generalization of the Poincaré sphere symmetry between signal and idler spatial modes. As we will see, the odd modes already capture the essential features of the symmetry, since for even orders the zero OAM components do not possess the required SU(2) structure.

4.2.1 Symmetry for First-Order Seed

We now briefly revisit the first-order case already discussed in Refs. [51, 26]. In this case, we can assume a Gaussian pump ($q_p = 0$) and a first order signal input,

$$\begin{aligned}\mathcal{E}_{pin} &= \alpha_{pin} \psi^{00}, \\ \mathcal{E}_{sin} &= A_{in}^{10} \left[\cos(\theta/2) \psi^{10} + e^{i\phi} \sin(\theta/2) \psi^{-10} \right].\end{aligned}\tag{4.19}$$

The first-order injection, as well as the OPO sketch, are represented in figures 43 and 44, respectively.

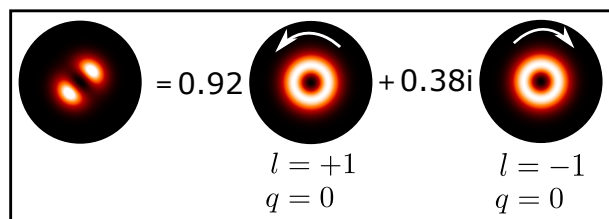


Figure 43 – Example of a first-order injection beam. In this case we have set $A_{in}^{10} = 1$, $\theta = 45^\circ$ and $\phi = 90^\circ$.

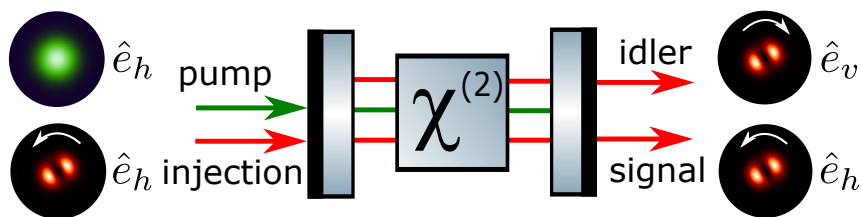


Figure 44 – Sketch of the optical parametric oscillator with type-II phase-matching and first-order structured light injection. \hat{e}_h and \hat{e}_v are the horizontal and vertical polarization unit vectors, respectively. The pump beam is a Gaussian mode.

The steady state intracavity pump amplitude is given by the solution of the quintic equation

$$\left[\gamma_r + \frac{|\Lambda_{00}^1 A_{in}^{10}|^2}{(1 - |\Lambda_{00}^1 \beta_p|^2)^2} \right] \beta_p = \beta_{pin}. \quad (4.20)$$

Then, the intracavity signal and idler spatial structures are

$$\begin{aligned} \mathcal{E}_s &= \xi_s^{10} \left[\cos(\theta/2) \psi^{10} + e^{i\phi} \sin(\theta/2) \psi^{-10} \right], \\ \mathcal{E}_i &= \xi_i^{10} \left[e^{-i\phi} \sin(\theta/2) \psi^{10} + \cos(\theta/2) \psi^{-10} \right], \end{aligned} \quad (4.21)$$

with the mode amplitudes given by

$$\begin{aligned} \xi_s^{10} &= \frac{\eta A_{in}^{10}/\gamma}{1 - |\Lambda_{00}^1 \beta_p|^2}, \\ \xi_i^{10} &= i\beta_p \Lambda_{00}^{1*} (\xi_s^{10})^*. \end{aligned} \quad (4.22)$$

The coordinates of the points representing the signal and idler structures in the Poincaré sphere are related by

$$\begin{aligned} \theta^i &= \pi - \theta^s, \\ \phi^i &= \phi^s. \end{aligned} \quad (4.23)$$

As shown in Fig. 45, the point representing the idler mode is the specular image of the point representing the signal with respect to the equatorial plane. This symmetry provides optimal intensity overlap and OAM conservation between signal and idler.

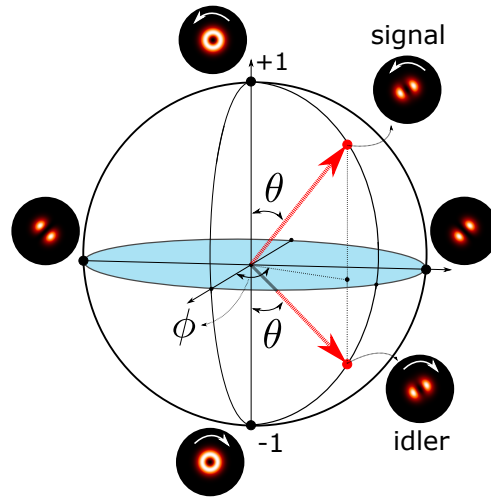


Figure 45 – Poincaré sphere representation for first-order OAM symmetry.

The experimental results for first-order modes are displayed in Figs. 46 and 47. The experimental details can be found in Ref. [26]. Since for first-order modes, the transverse profile of signal and idler are theoretically the same, only with opposite OAM values, we had to use the tilted lens method, previously discussed, in order to distinguish the down-converted modes following a meridian trajectory, illustrated in Fig. 47. For the modes lying in the equator, the tilted lens was not necessary, since those modes do not have OAM. So its equality of transverse structure is enough to prove the symmetry in this region, according to Fig. 46.

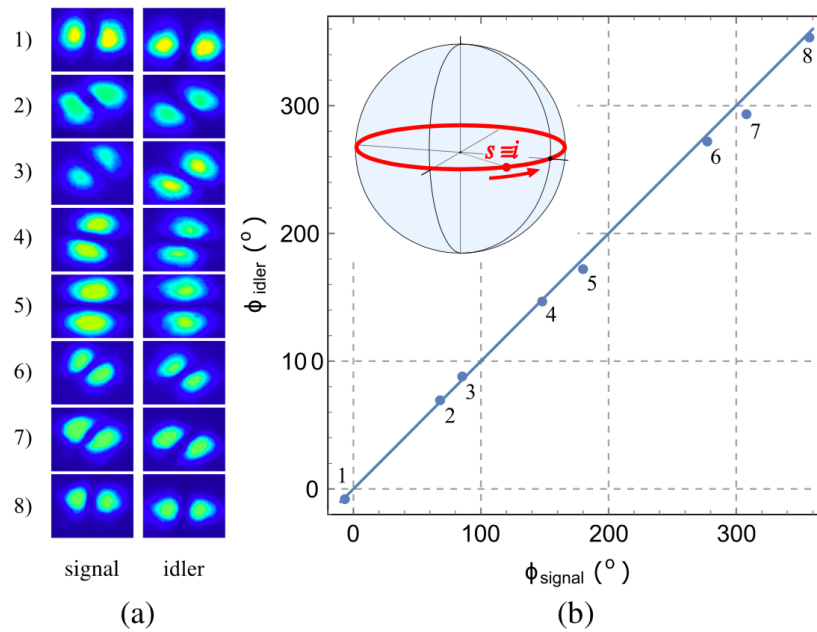


Figure 46 – (a) Image shots of signal and idler beams along the equator. (b) Azimuthal angles measured from the mode inclination α with respect to the horizontal. The straight line shows the theoretical prediction. The standard deviations are smaller than 4° . The error bars are not visible within graphic precision.

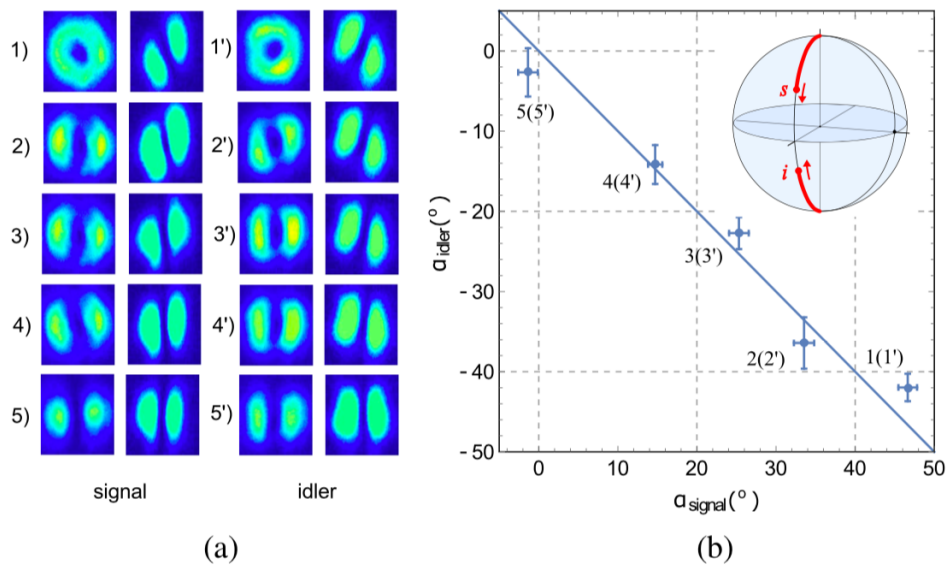


Figure 47 – (a) Original (left) and mode-converted (right) image shots of signal and idler beams along the $\phi = 0$ meridian. (b) Inclinations angles α measured with respect to the horizontal HG mode. The straight line shows the theoretical prediction. The standard deviations are smaller than 4° .

4.2.2 Symmetry for Second-Order Seed

The even-order subspaces include a zero-OAM mode with radial number $q = N/2$. Since it is an isolated single-mode subspace, there is no room for a Poincaré sphere representation or symmetry relation. The remaining OAM carrying modes can be grouped in pairs with opposite OAM, constituting a set of independent SU(2) structures where the aforementioned symmetry is verified. For example, consider the case of a second order seed beam $\{\psi^{\pm 20}, \psi^{01}\}$ and a single-mode pump with zero OAM and radial order $q_p = 1$,

$$\begin{aligned}\mathcal{E}_{p_{in}} &= \alpha_{p_{in}} \psi^{01}, \\ \mathcal{E}_{s_{in}} &= A_{in}^{01} \psi^{01} + A_{in}^{20} [\cos(\theta/2) \psi^{20} + e^{i\phi} \sin(\theta/2) \psi^{-20}].\end{aligned}\quad (4.24)$$

The second-order injection is represented in figure 48.

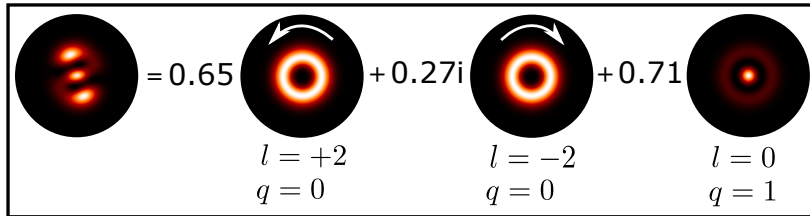


Figure 48 – Example of a second-order seed beam. In this case we have set $A_{in}^{01} = A_{in}^{20} = 1/\sqrt{2}$, $\theta = 45^\circ$ and $\phi = 90^\circ$.

The idler modes which will profit from the pump and seed energy are those with maximum spatial overlap with the input modes. First, OAM conservation is required for non-vanishing overlap. Then, the radial order associated with each OAM is determined by the maximum numerical value of the overlap integrals $\Lambda_{0q_i}^2$ and $\Lambda_{1q_i}^0$. In Fig. 49 we show the numerical value of the overlap integrals as a function of the idler radial order. Those simulations were made accordingly to Ref. [43].

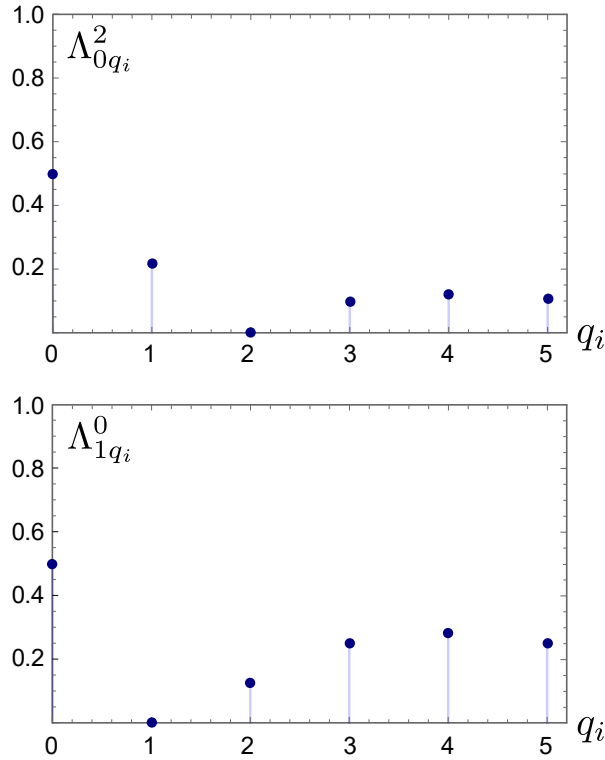


Figure 49 – Pump-signal-idler overlap integrals for $l = \pm 2$ (top) and $l = 0$ (bottom) as a function of the idler radial orders, when the pump parameters are fixed at $l_p = 0$ and $q_p = 1$.

As we can see, for both $l = 0$ and $l = \pm 2$, the zero radial order ($q_i = 0$) displays optimal coupling. Therefore, the transverse modes taking part in the intracavity interaction are $\{\psi^{01}\}$ for the pump, $\{\psi^{01}, \psi^{\pm 20}\}$ for the signal and $\{\psi^{00}, \psi^{\pm 20}\}$ for the idler. In this case, the pump steady-state is given by the solution of

$$\left[\gamma_r + \frac{|\Lambda_{10}^0 A_{in}^{01}|^2}{(1 - |\Lambda_{10}^0 \beta_p|^2)^2} + \frac{|\Lambda_{00}^2 A_{in}^{20}|^2}{(1 - |\Lambda_{00}^2 \beta_p|^2)^2} \right] \beta_p = \beta_{p_{in}}, \quad (4.25)$$

and the steady state amplitudes of signal and idler are

$$\begin{aligned} \mathcal{E}_s &= \xi_s^{01} \psi^{01} + \xi_s^{20} \left[\cos(\theta/2) \psi^{20} + e^{i\phi} \sin(\theta/2) \psi^{-20} \right], \\ \mathcal{E}_i &= \xi_i^{00} \psi^{00} + \xi_i^{20} \left[e^{-i\phi} \sin(\theta/2) \psi^{20} + \cos(\theta/2) \psi^{-20} \right], \end{aligned} \quad (4.26)$$

with the mode amplitudes given by

$$\begin{aligned} \xi_s^{01} &= \frac{\eta A_{in}^{01}/\gamma}{1 - |\Lambda_{10}^0 \beta_p|^2}, & \xi_s^{20} &= \frac{\eta A_{in}^{20}/\gamma}{1 - |\Lambda_{00}^2 \beta_p|^2}, \\ \xi_i^{00} &= i \beta_p \Lambda_{10}^{0*} (\xi_s^{01})^*, & \xi_i^{20} &= i \beta_p \Lambda_{00}^{2*} (\xi_s^{20})^*. \end{aligned} \quad (4.27)$$

Note that no special symmetry can be realized in the zero OAM subspace, only the usual conjugation relation between signal and idler amplitudes. However, as shown in Fig. 50, the $l = \pm 2$ subspace displays the same kind of Poincaré sphere symmetry as the first order case, with the signal and idler coordinates related by

$$\begin{aligned}\theta^i &= \pi - \theta^s, \\ \phi^i &= \phi^s.\end{aligned}\tag{4.28}$$

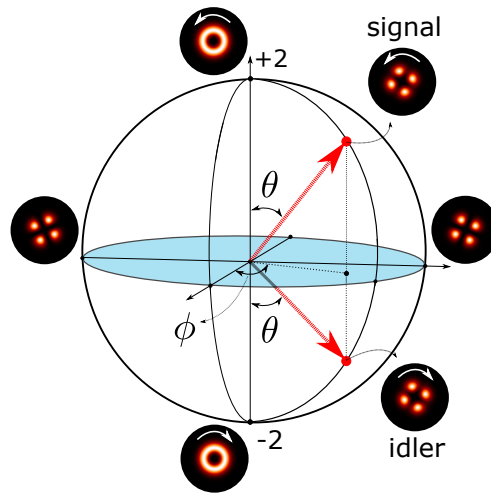


Figure 50 – Signal and idler symmetry in the Poincaré sphere for 2nd order OAM ($l = \pm 2$).

From our numerical integration, which will be presented in the next section, we can simulate the transverse profile for both signal and idler. The coefficients of the superposition, as well as the transverse structure of the down-converted modes, are displayed in the Fig.51. The results are in good agreement with the analytical expression for the coordinates angle in (4.28). A sketch of a second-order injected OPO is illustrated in the Fig.52.

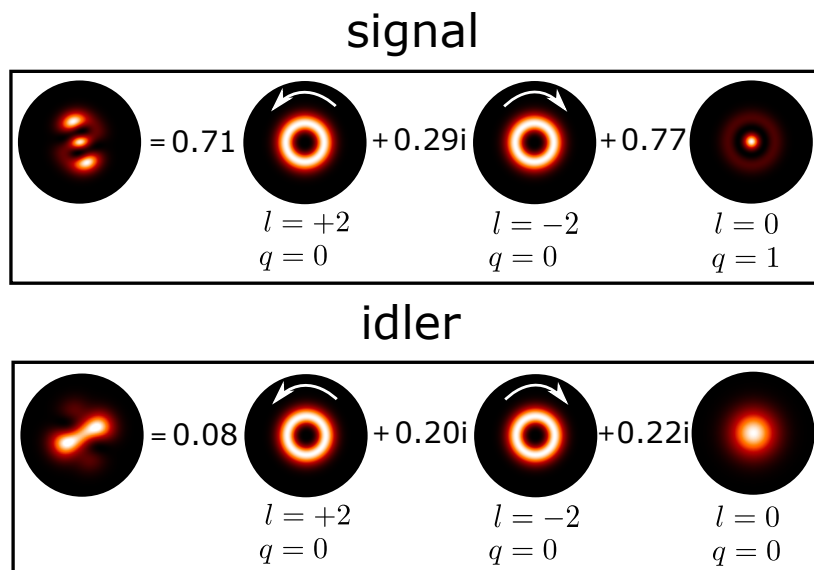


Figure 51 – Down-converted modes given the second-order injection in Fig.48. The coefficients were obtained from our numerical integration. The coordinate angles are $\theta^s = 0.78$ rad, $\theta^i = 2.36$ rad and $\phi^s = \phi^i = 1.57$ rad.

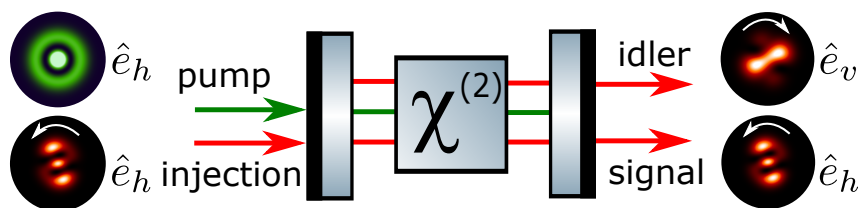


Figure 52 – Sketch of the optical parametric oscillator with type-II phase-matching and second-order structured light injection. \hat{e}_h and \hat{e}_v are the horizontal and vertical polarization unit vectors, respectively. The pump is radially structured ($l = 0$, $q = 1$) to optimize the spatial overlap with signal and idler.

4.2.3 Symmetry for Third-Order Seed: Two-Spheres

The simplest case with more than one Poincaré sphere symmetry is realized by a third-order seed beam. As before, the pump is assumed to carry zero OAM and optimal overlap is attained with $q_p = 2$. In Fig. 53 we show the overlap integrals for different OAM values. As we can see, the largest coupling between signal and idler modes with $l = \pm 1$ and ± 3 occurs for the idler radial index $q_i = 0$. Therefore, the $l = \pm 3$ sphere represents signal and idler modes with $q_s = q_i = 0$. However, the $l = \pm 1$ sphere represents signal modes with $q_s = 1$ and idler modes

with $q_i = 0$. In any case, the radial numbers are irrelevant for the Poincaré symmetry condition, which is essentially determined by OAM conservation.

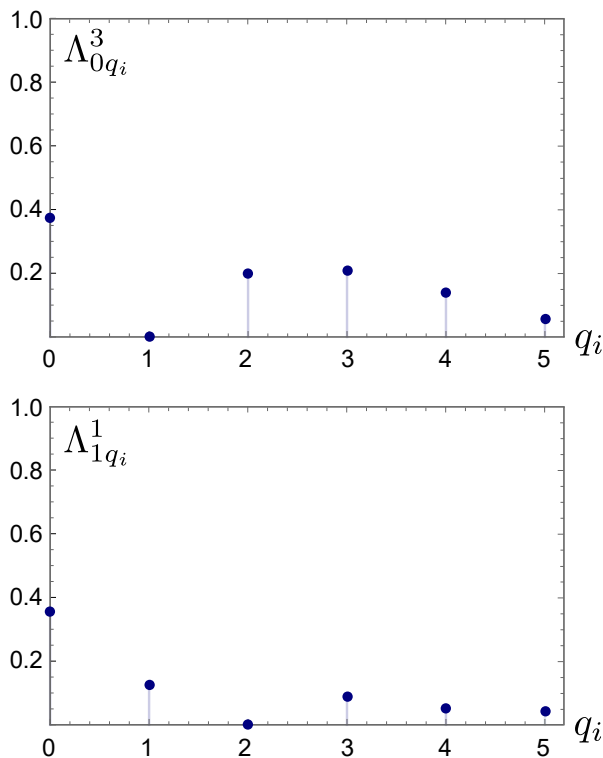


Figure 53 – Pump-signal-idler spatial overlap for $l = \pm 3$ (top) and $l = \pm 1$ (bottom) as a function of the idler radial orders, when the pump parameters are fixed at $l_p = 0$ and $q_p = 2$.

With these input modes, the source terms in the dynamical equations become

$$\begin{aligned}
 \mathcal{E}_{pin} &= \alpha_{pin} \psi^{02}, \\
 \mathcal{E}_{sin} &= A_{in}^{30} \left[\cos(\theta_3/2) \psi^{30} + e^{i\phi_3} \sin(\theta_3/2) \psi^{-30} \right] \\
 &\quad + A_{in}^{11} \left[\cos(\theta_1/2) \psi^{11} + e^{i\phi_1} \sin(\theta_1/2) \psi^{-11} \right]. \quad (4.29)
 \end{aligned}$$

Two sets of Poincaré sphere coordinates are used, (θ_1, ϕ_1) and (θ_3, ϕ_3) , associated with the $l = \pm 1$ and $l = \pm 3$ manifolds, respectively. In Fig. 54 we show an example of seed beam and its decomposition in these manifolds.

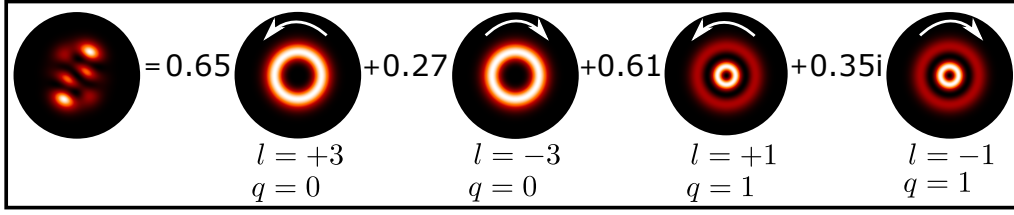


Figure 54 – Example of a third-order seed beam with $A_{in}^{11} = A_{in}^{30} = 1/\sqrt{2}$. The coordinates on the Poincaré spheres for $l = \pm 3$ and $l = \pm 1$ are $(\theta_3 = 45^\circ, \phi_3 = 0^\circ)$ and $(\theta_1 = 60^\circ, \phi_1 = 90^\circ)$, respectively.

The steady state intracavity pump amplitude is given by the solution of the quintic equation

$$\left[\gamma_r + \frac{|\Lambda_{00}^3 A_{in}^{30}|^2}{(1 - |\Lambda_{00}^3 \beta_p|^2)^2} + \frac{|\Lambda_{10}^1 A_{in}^{11}|^2}{(1 - |\Lambda_{10}^1 \beta_p|^2)^2} \right] \beta_p = \beta_{p_{in}}. \quad (4.30)$$

Once the solution of Eq. (4.30) is obtained, the intracavity signal and idler spatial structures can be readily calculated from

$$\begin{aligned} \mathcal{E}_s &= \xi_s^{30} \left[\cos(\theta_3/2) \psi^{30} + e^{i\phi_3} \sin(\theta_3/2) \psi^{-30} \right], \\ &+ \xi_s^{11} \left[\cos(\theta_1/2) \psi^{11} + e^{i\phi_1} \sin(\theta_1/2) \psi^{-11} \right], \\ \mathcal{E}_i &= \xi_i^{30} \left[e^{-i\phi_3} \sin(\theta_3/2) \psi^{30} + \cos(\theta_3/2) \psi^{-30} \right], \\ &+ \xi_i^{10} \left[e^{-i\phi_1} \sin(\theta_1/2) \psi^{10} + \cos(\theta_1/2) \psi^{-10} \right], \end{aligned} \quad (4.31)$$

with the mode amplitudes given by

$$\begin{aligned} \xi_s^{30} &= \frac{\eta A_{in}^{30}/\gamma}{1 - |\Lambda_{00}^3 \beta_p|^2}, & \xi_s^{11} &= \frac{\eta A_{in}^{11}/\gamma}{1 - |\Lambda_{10}^1 \beta_p|^2}, \\ \xi_i^{30} &= i\beta_p \Lambda_{00}^{3*} (\xi_s^{30})^*, & \xi_i^{10} &= i\beta_p \Lambda_{10}^{1*} (\xi_s^{11})^*. \end{aligned} \quad (4.32)$$

These mode superpositions are represented in the Poincaré spheres shown in Fig. 55. The signal and idler coordinates are related by

$$\begin{aligned} \theta_3^i &= \pi - \theta_3^s, & \phi_3^i &= \phi_3^s, \\ \theta_1^i &= \pi - \theta_1^s, & \phi_1^i &= \phi_1^s. \end{aligned} \quad (4.33)$$

These relations show that the signal and idler modes verify the Poincaré symmetry independently on each sphere. As before, this condition ensures both maximal intensity overlap and OAM conservation. The extension of this symmetry condition to higher orders is straightforward. The mode space can be split in two-dimensional

OAM subspaces with fixed absolute value $|l| = 1, 2, 3, \dots$, where the symmetry condition is simultaneously verified on independent Poincaré spheres. For even orders, there is an isolated component with zero OAM, where no symmetry condition can be realized other than the usual phase conjugation between signal and idler amplitudes.

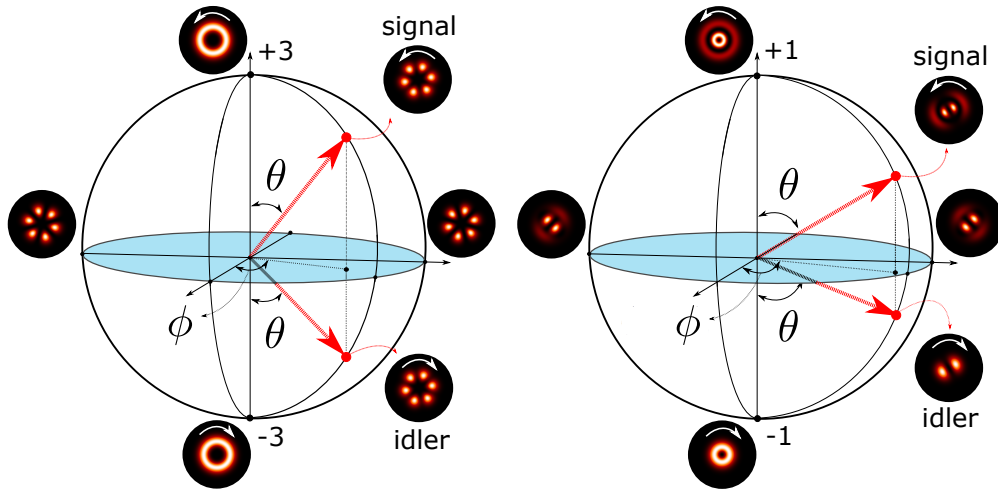


Figure 55 – Third-order OAM symmetry. On left side we can visualize the symmetry relation verified in the Poincaré sphere for $l = \pm 3$ and on the right side the same symmetry is displayed on the independent sphere for $l = \pm 1$..

From our numerical integration, which will be presented in the next section, we can simulate the transverse profile for both signal and idler. The coefficients of the superposition, as well as the transverse structure of the down-converted modes, are displayed in the Fig.56. The results are in good agreement with the analytical expression for the coordinates angle in (4.33). A sketch of a third-order injected OPO is illustrated in the Fig.42.

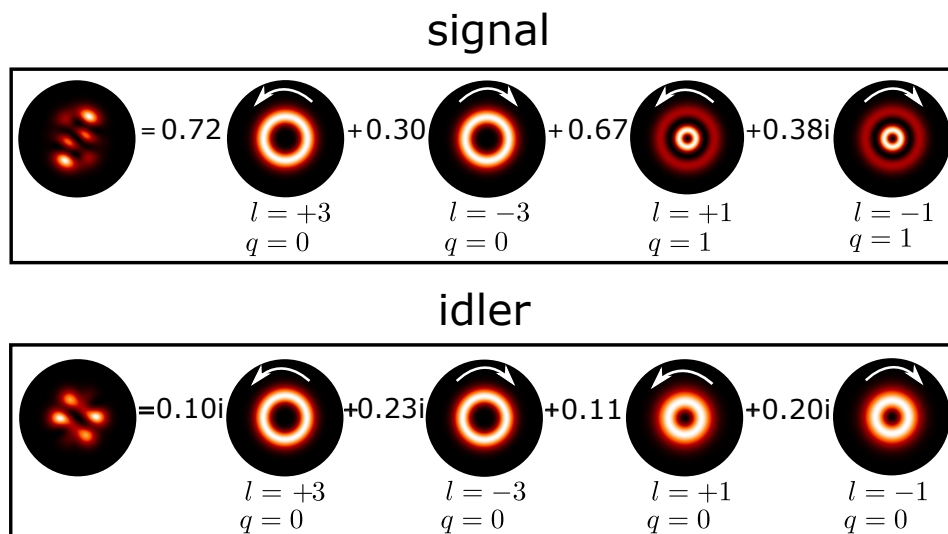


Figure 56 – Down-converted modes given the third-order injection in Fig.54. The coefficients were obtained from our numerical integration. The coordinate angles in the Poincaré sphere for $l = \pm 3$ are $\theta_3^s = 0.78$ rad, $\theta_3^i = 2.35$ rad and $\phi_3^s = \phi_3^i = 0$ rad. In the Poincaré sphere for $l = \pm 1$ we have $\theta_1^s = 1.04$ rad, $\theta_1^i = 2.09$ rad and $\phi_1^s = \phi_1^i = 1.57$ rad.

4.2.4 Symmetry for OAM-Structured Pump

It is also interesting to investigate how the Poincaré sphere symmetry between signal and idler is affected by a pump beam carrying OAM. In this case, a Poincaré representation also applies to the pump beam. For example, let us consider a pump beam prepared in a superposition of second-order modes with $l = \pm 2$ and $q_p = 0$. The seed beam is assumed to be a first-order superposition of modes with $l = \pm 1$. The pump and seed input amplitudes can be written as

$$\begin{aligned}\mathcal{E}_{p_{in}} &= A_{p_{in}} \left[\cos(\theta_p/2) \psi^{20} + e^{i\phi_p} \sin(\theta_p/2) \psi^{-20} \right], \\ \mathcal{E}_{s_{in}} &= A_{s_{in}} \left[\cos(\theta_s/2) \psi^{10} + e^{i\phi_s} \sin(\theta_s/2) \psi^{-10} \right],\end{aligned}\quad (4.34)$$

where (θ_p, ϕ_p) and (θ_s, ϕ_s) are the Poincaré sphere coordinates of the input pump and seed beams, respectively. In Fig. 57, we display the Poincaré representation of the pump (left) and seed (right) input modes. The idler modes with optimal intensity overlap and OAM conservation with the seed are also first order LG modes with $l = \pm 1$ and $q_i = 0$.

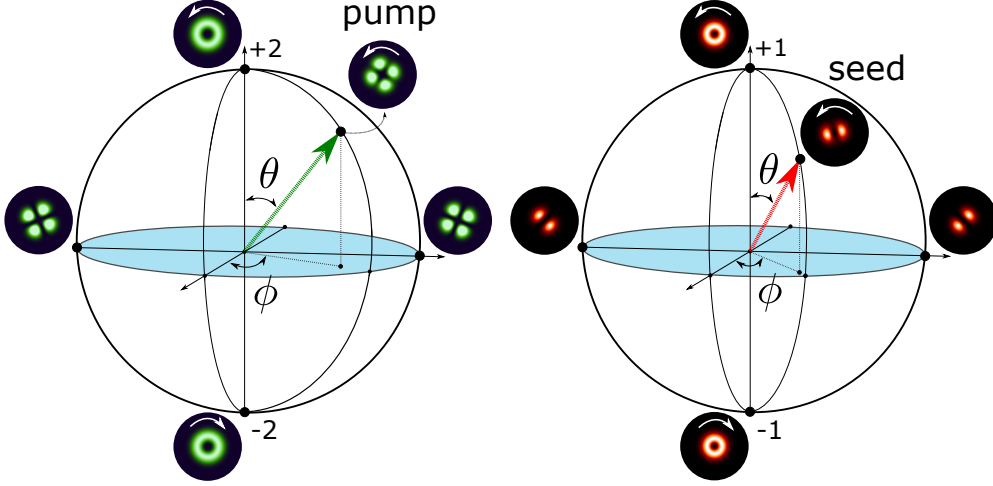


Figure 57 – Poincaré sphere representations of the pump ($l = \pm 2$) and seed ($l = \pm 1$) beams.

The time evolution of the pump, signal and idler intracavity amplitudes is governed by the following dynamical equations

$$\begin{aligned}
 \dot{\beta}_p^+ &= -\gamma_r \beta_p^+ + i\Lambda \beta_s^+ \beta_i^+ + \beta_{pin} \cos(\theta_p/2), \\
 \dot{\beta}_p^- &= -\gamma_r \beta_p^- + i\Lambda \beta_s^- \beta_i^- + \beta_{pin} e^{i\phi_p} \sin(\theta_p/2), \\
 \dot{\beta}_s^+ &= -\beta_s^+ + i\Lambda^* \beta_p^+ \beta_i^{+*} + \beta_{sin} \cos(\theta_s/2), \\
 \dot{\beta}_s^- &= -\beta_s^- + i\Lambda^* \beta_p^- \beta_i^{-*} + \beta_{sin} e^{i\phi_s} \sin(\theta_s/2), \\
 \dot{\beta}_i^\pm &= -\beta_i^\pm + i\Lambda^* \beta_p^\pm (\beta_s^\pm)^*,
 \end{aligned} \tag{4.35}$$

where β_p^\pm are the normalized pump amplitudes for $l = \pm 2$, $\beta_{s(i)}^\pm$ are the normalized seed (idler) amplitudes for $l = \pm 1$, and the time derivatives in the left-hand-side are taken with respect to the dimensionless parameter $\tau = \gamma t$. The mode coupling is mediated by the three-mode overlap

$$\Lambda = \int [\psi_p^{\pm 20}(\mathbf{r})]^* \psi_s^{\pm 10}(\mathbf{r}) \psi_i^{\pm 10}(\mathbf{r}) d^2\mathbf{r}. \tag{4.36}$$

The steady state solutions are obtained by setting the time derivatives equal to zero in the left-hand-side of Eqs.(4.35) and solving the resulting algebraic equations. From the last three equations in (4.35), we have

$$\begin{aligned}
 \beta_s^+ &= \xi_s^+ \cos(\theta_s/2), & \beta_s^- &= \xi_s^- e^{i\phi_s} \sin(\theta_s/2), \\
 \beta_i^+ &= \xi_i^+ \cos(\theta_s/2), & \beta_i^- &= \xi_i^- e^{-i\phi_s} \sin(\theta_s/2),
 \end{aligned} \tag{4.37}$$

where we defined

$$\begin{aligned}\xi_s^\pm &= \frac{\eta A_{sin}/\gamma}{1 - |\Lambda \beta_p^\pm|^2}, \\ \xi_i^\pm &= i\beta_p^\pm \Lambda^* (\xi_s^\pm)^*\end{aligned}\quad (4.38)$$

The steady state intracavity pump amplitudes are given by the solutions of two independent quintic equations

$$\begin{aligned}\left[\gamma_r + \frac{|\Lambda A_{sin}|^2 \cos^2\left(\frac{\theta_s}{2}\right)}{\left(1 - |\Lambda \beta_p^+|^2\right)^2} \right] \beta_p^+ &= \beta_{pin} \cos\left(\frac{\theta_p}{2}\right), \\ \left[\gamma_r + \frac{|\Lambda A_{sin}|^2 \sin^2\left(\frac{\theta_s}{2}\right)}{\left(1 - |\Lambda \beta_p^-|^2\right)^2} \right] \beta_p^- &= \beta_{pin} e^{i\phi_p} \sin\left(\frac{\theta_p}{2}\right).\end{aligned}\quad (4.39)$$

From Eqs. (4.37) we immediately obtain the complete structure of the intracavity signal and idler fields as

$$\begin{aligned}\mathcal{E}_s &= \xi_s^+ \cos(\theta_s/2) \psi^{10} + \xi_s^- e^{i\phi_s} \sin(\theta_s/2) \psi^{-10}, \\ \mathcal{E}_i &= \xi_i^+ \cos(\theta_s/2) \psi^{10} + \xi_i^- e^{-i\phi_s} \sin(\theta_s/2) \psi^{-10}.\end{aligned}\quad (4.40)$$

The Poincaré sphere representation of signal and idler depends on both the seed and pump parameters. While the seed parameters are explicit in the expressions above, the dependence on the pump is implicit through $\xi_{s,i}^\pm$.

Assuming weak pump and seed powers, the pump is not significantly depleted by the parametric interaction and the intracavity pump is essentially driven by the external input, leading to

$$\begin{aligned}\beta_p^+ &\approx \frac{\beta_{pin}}{\gamma_r} \cos(\theta_p/2), \\ \beta_p^- &\approx \frac{\beta_{pin}}{\gamma_r} e^{i\phi_p} \sin(\theta_p/2).\end{aligned}\quad (4.41)$$

In this case, we can write the analytical solutions for signal and idler as

$$\mathcal{E}_s = \xi_s^+ \cos\left(\frac{\theta_s}{2}\right) \psi^{+10} + \xi_s^- e^{i\phi_s} \sin\left(\frac{\theta_s}{2}\right) \psi^{-10}, \quad (4.42)$$

$$\mathcal{E}_i = \xi_i^+ \cos\left(\frac{\theta_s}{2}\right) \cos\left(\frac{\theta_p}{2}\right) \psi^{+10} + \xi_i^- e^{i(\phi_p - \phi_s)} \sin\left(\frac{\theta_s}{2}\right) \sin\left(\frac{\theta_p}{2}\right) \psi^{-10}, \quad (4.43)$$

where the amplitudes can be explicitly written in terms of the pump parameters as

$$\begin{aligned}\xi_s^\pm &= \frac{\eta A_{s_{in}}/\gamma}{1 - \frac{|\Lambda\beta_{pin}|^2}{2\gamma^2}(1 \pm \cos\theta_p)}, \\ \xi_i^\pm &= i\beta_p^\pm \Lambda^* (\xi_s^\pm)^*\end{aligned}\quad (4.44)$$

In this regime, the Poincaré symmetry becomes more evident for special values of the pump and seed parameters. First, for $\theta_p = \pi/2$ and arbitrary ϕ_p , we easily obtain that $\theta_i = \theta_s$ and $\phi_i = \phi_p - \phi_s$. This symmetry is displayed in Fig. 58 for $\phi_p = 0$ and in Fig.59 we illustrate a OPO sketch of this situation. The idler spatial structure is represented by the specular image of the signal with respect to the great circle $\phi = 0$.

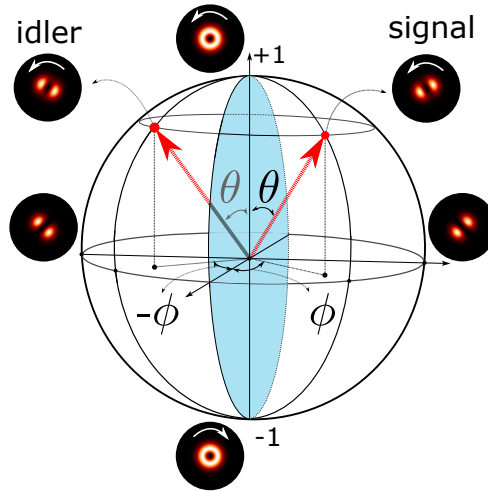


Figure 58 – Poincaré sphere representation of the intracavity signal and idler structures when $\theta_p = \pi/2$ and $\phi_p = 0$.

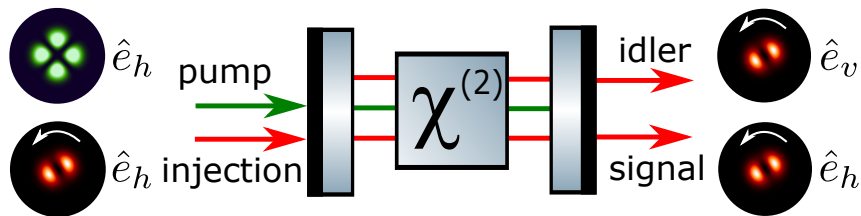


Figure 59 – Sketch of the optical parametric oscillator with type-II phase-matching, first-order structured light injection and second-order balanced pump ($\theta_p = \pi/2$ and $\phi_p = 0$). \hat{e}_h and \hat{e}_v are the horizontal and vertical polarization unit vectors.

Moreover, restricting the input pump power to values well below the free-running oscillation threshold, such that

$$\frac{|\Lambda\beta_{pin}|^2}{2\gamma_r^2} \ll 1, \quad (4.45)$$

one can take $\xi_s^+ \approx \xi_s^-$ and $\xi_i^+ \approx \xi_i^-$. From Eqs. (4.42) and (4.43), it is easy to see that the idler parameters are related to the pump and seed parameters as

$$\phi_i = \phi_p - \phi_s, \quad (4.46)$$

$$\tan\left(\frac{\theta_i}{2}\right) = \tan\left(\frac{\theta_p}{2}\right)\tan\left(\frac{\theta_s}{2}\right). \quad (4.47)$$

Therefore, the seed and idler beams are azimuthally symmetric in the first order Poincaré sphere with respect to the angle $\phi_p/2$, while the idler polar location follows a nontrivial relation with the pump and seed polar parameters. Another interesting condition within this regime occurs for $\theta_s = \pi/2$ and $\phi_s = 0$. In this case, the idler parameters become equal to those of the pump, $\theta_i = \theta_p$ and $\phi_i = \phi_p$. Therefore, the idler spatial structure can be actively controlled by fixing either the pump or the seed parameters and varying the others. In a real experimental situation, this active control can be challenged by the astigmatic effects caused by the crystal birefringence [42]. However, this effect can be compensated for with a two-crystal setup, which we will represent in the experimental proposal section, as the one used in Ref. [52, 53]. Active control of signal and idler spatial structures exploring symmetry conditions can be useful for shaping spatial quantum correlations generated in parametric amplification.

4.3 Numerical Simulations Results

In this section, we are going to expose and discuss the results of our numerical simulations. All simulations were made in the software *Wolfram Mathematica*¹. We are interested in exploring the numerical values of the complex amplitudes $\beta_j^{\pm lq}$ ($j = p, s, i$), where l is the OAM value and q is the radial order, evolving in time according to Equations (4.6), (4.7) and (4.8). With those values, we can verify the coordinates angles in the Poincaré sphere, which means, verify the symmetry properties discussed. As we previously have shown, we are taking all the time derivatives in terms of the dimensionless time $\tau = \gamma t$. For simplicity, we choose $\gamma = 1$ (a.u) in all graphs. In that way, the time scale is in units of τ .

¹ Developer: Wolfram Research.

Let's begin by discussing the results for first-order modes. The numerical solution for the complex coefficients are shown in Fig.60. In this case, we considered an injection mode, represented on Fig. 43, on the angles $\theta = 45^\circ$ and $\phi = 90^\circ$ on the Poincaré sphere. After achieving the stationary condition we obtained from the coefficients the spherical coordinates for signal and idler on the first-order Poincaré sphere. The values are $\theta_1 = 0.7854$ rad and $\phi_1 = 1.571$ rad. Those values are in perfect agreement with the analytical prediction.

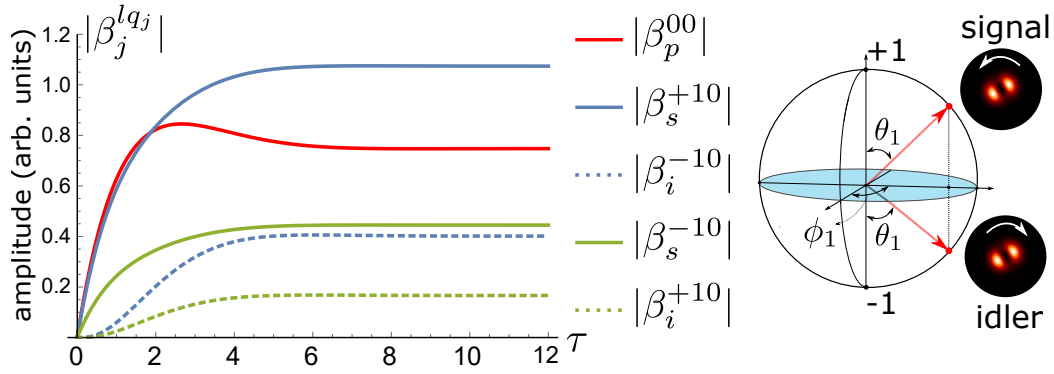


Figure 60 – Symmetry for the numerical simulation of the OPO dynamics under first-order injection (Fig.43). The spherical coordinates for $l = \pm 1$ are $\theta_1 = 0.7854$ rad and $\phi_1 = 1.571$ rad. The pump, seed and decay parameters were set to $\beta_{pin} = 1$, $A_{in}^{10} = 1$ and $\gamma_r = 1$, respectively. The free-running oscillation threshold is $\beta_{pth} \approx 2.0$.

For the second-order injected OPO the numerical solutions for the complex coefficients are shown in Fig.61. In this case, we considered an injection mode, represented on Fig. 48, on the angles $\theta = 45^\circ$ and $\phi = 90^\circ$ on the Poincaré sphere. After achieving the stationary condition we obtained from the coefficients the spherical coordinates for signal and idler on the second-order Poincaré sphere. The values are $\theta_1 = 0.7854$ rad and $\phi_1 = 1.571$ rad.

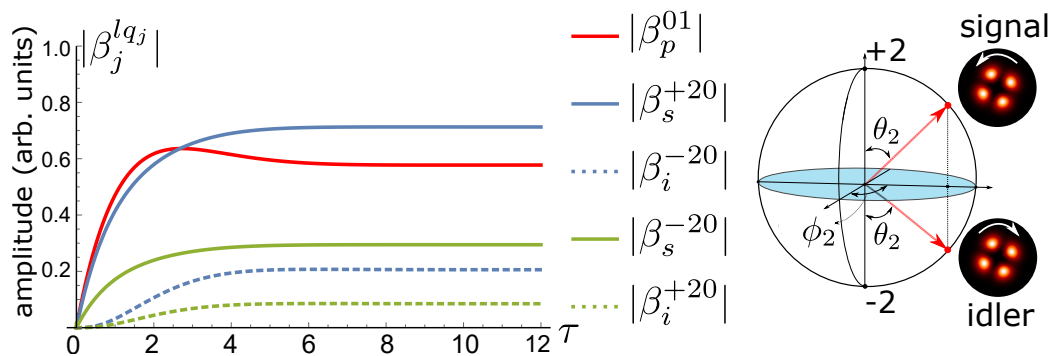


Figure 61 – Symmetry for the numerical simulation of the OPO dynamics under second-order injection (Fig.48). The spherical coordinates for $l = \pm 2$ are $\theta_2 = 0.7854$ rad and $\phi_2 = 1.571$ rad. The pump, seed and decay parameters were set to $\beta_{pin} = 0.75$, $A_{in}^{20} = 1/\sqrt{2}$ and $\gamma_r = 1$, respectively. The free-running oscillation threshold is $\beta_{pth} \approx 2.0$.

The tests for the symmetry condition for third-order injection were also performed. In this case, we considered an injection mode, represented on Fig. 54, on the angles $\theta = 45^\circ$ and $\phi = 0^\circ$ for $l = \pm 3$ Poincaré sphere and $\theta = 60^\circ$ and $\phi = 90^\circ$ for the $l = \pm 1$ Poincaré sphere. The numerical results for the signal and idler mode amplitudes are displayed in Fig. 62, along with the resulting two-sphere representation. The spherical coordinates are evaluated from the numerical results, confirming the two-sphere symmetry condition. The spherical coordinates are $\theta_3 = 0.7343$ rad and $\phi_3 = 0$ for $l = \pm 3$. For $l = \pm 1$, we got the spherical coordinates $\theta_1 = 1.042$ rad and $\phi_1 = 1.571$ rad.

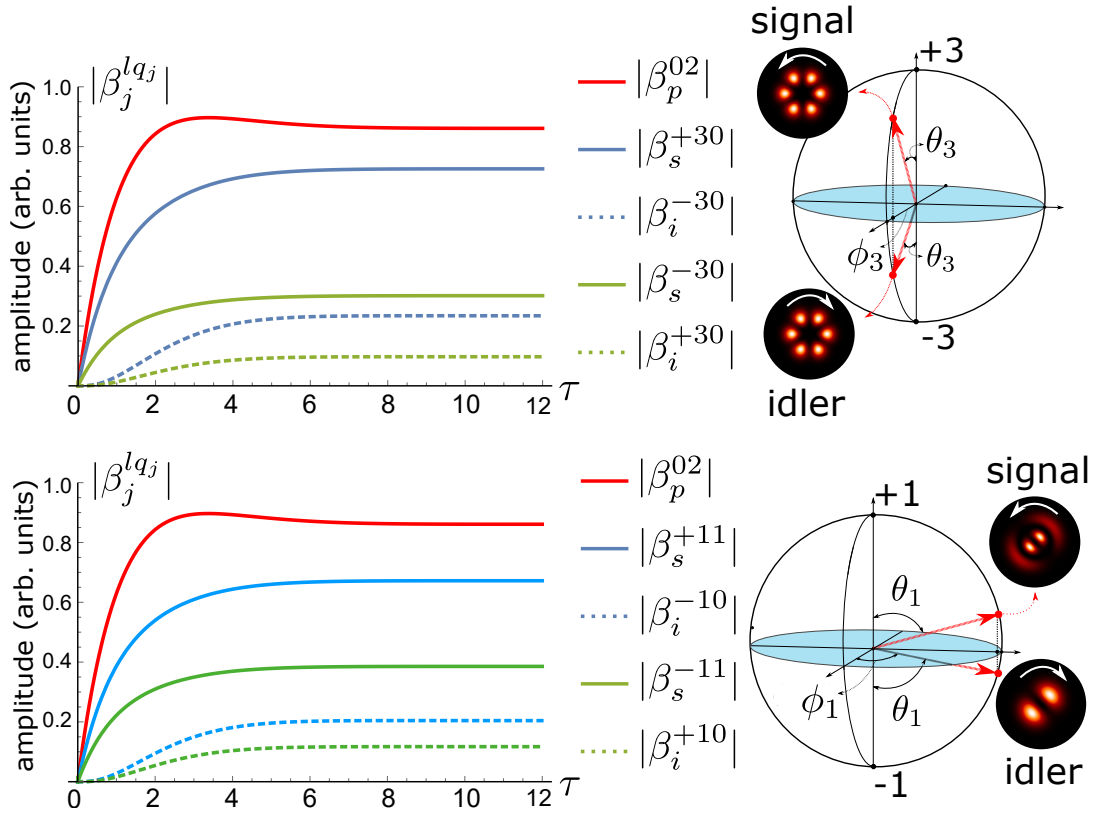


Figure 62 – Two-sphere symmetry for the numerical simulation of the OPO dynamics under third-order injection (Fig.54). The spherical coordinates for $l = \pm 3$ are $\theta_3 = 0.7343$ rad and $\phi_3 = 0$. For $l = \pm 1$ the coordinates are $\theta_1 = 1.042$ rad and $\phi_1 = 1.571$ rad. The pump, seed and decay parameters were set to $\beta_{pin} = 1$, $A_{in}^{30} = A_{in}^{11} = 1/\sqrt{2}$ and $\gamma_r = 1$, respectively. The free-running oscillation threshold is $\beta_{pth} \approx 2.7$.

Another interesting case is when we structure the pump. In this case, we also considered a first-order injection mode, represented on Fig. 43, on the angles $\theta = 45^\circ$ and $\phi = 90^\circ$ on the Poincaré sphere. The pump, on the other hand, is a balanced second-order mode. Its spherical coordinates on the second-order Poincaré sphere are $\theta = 90^\circ$ and $\phi = 0^\circ$. Let's recall that from our theoretical predictions that we are assuming weak pump and seed power (4.41). This condition will lead signal and idler to have spherical coordinates $\theta_s = \theta_i$ and $\phi_s = \phi_i$. This physical situation is geometrically represented on Fig.63 and is in agreement with our theoretical predictions.

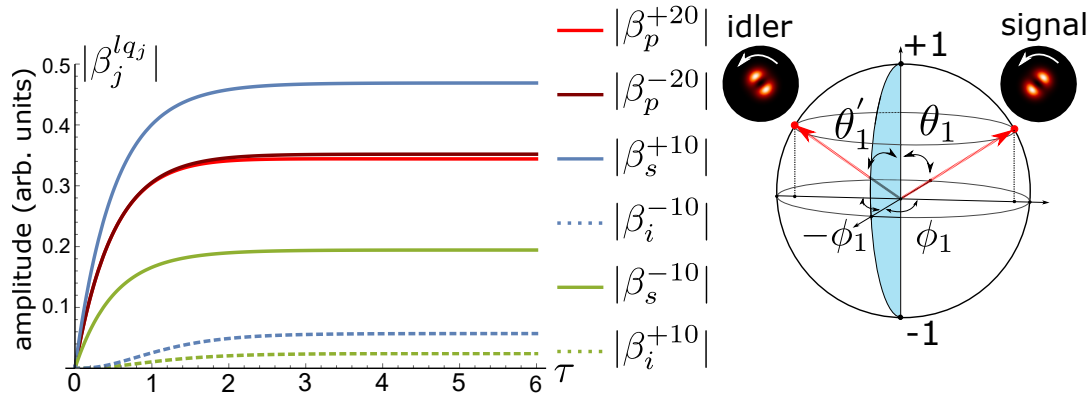


Figure 63 – Symmetry for the numerical simulation of the OPO dynamics under first-order injection (Fig.43) and second-order balanced pump ($\theta_p = 90^\circ$ and $\phi_p = 0^\circ$). The spherical coordinates for $l = \pm 1$ are $\theta_1 = 0.7859$ rad, $\theta'_1 = 0.8019$ rad and $\phi_1 = 1.571$ rad. The pump, seed and decay parameters were set to $\beta_{pin}^+ = \beta_{pin}^- = 0.707$, $A_{in}^{10} = 1$ and $\gamma_r = 1$, respectively. The free-running oscillation threshold is $\beta_{pth} \approx 5.7$.

The last counterintuitive situation we numerically explored is when we also considered a first-order injection mode, but fixed in the equatorial plane ($\theta = 90^\circ$ and $\phi = 0^\circ$). The pump, on the other hand, is a second-order mode with spherical coordinates on the second-order Poincaré sphere $\theta = 45^\circ$ and $\phi = 90^\circ$. Recalling our theoretical predictions we are assuming a well below threshold condition (4.45) and the spherical coordinates for signal and idler are represented in Equations (4.46) and (4.47). It is also important to mention that the results have converged without the need for a weak pump input "well-below" threshold. Quantitatively speaking, the pump complex amplitudes was fixed as $\beta_{pin}^+ = 0.924$ and $\beta_{pin}^- = 0.383i$, while the threshold was set to $\beta_{pth} \approx 5.7$. In a real-world experiment, this is a very reasonable condition to attend. The numerical integration of this case is represented on Fig.64

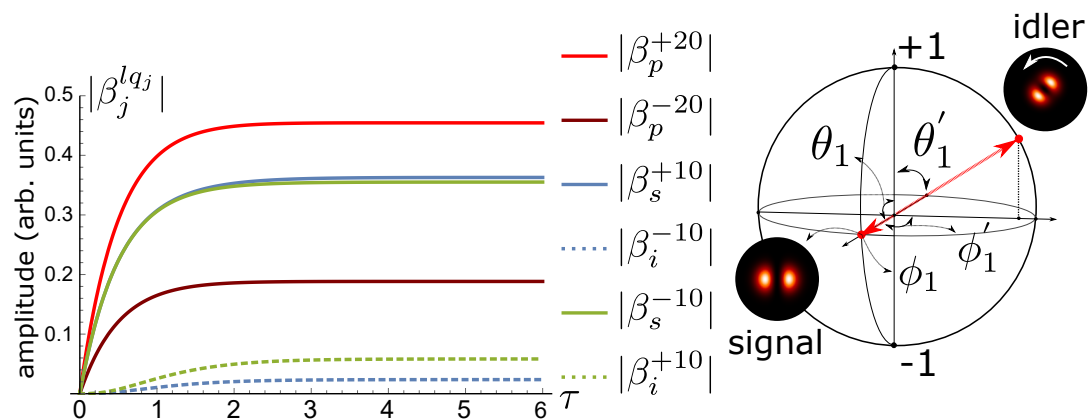


Figure 64 – Symmetry for the numerical simulation of the OPO dynamics under first-order injection (Fig.43) and second-order pump ($\theta_p = 45^\circ$ and $\phi_p = 90^\circ$). The spherical coordinates for $l = \pm 1$ are $\theta_1 = 1.549$ rad, $\theta'_1 = 0.7706$ rad, $\phi_1 = 0$ rad and $\phi'_1 = 1.571$ rad. The pump, seed and decay parameters were set to $\beta_{pin}^+ = 0.924$, $\beta_{pin}^- = 0.383i$, $A_{in}^{10} = 1$ and $\gamma_r = 1$, respectively. The free-running oscillation threshold is $\beta_{pth} \approx 5.7$.

4.4 Experimental Proposal

In this section, we are going to make a proposal of a experimental setup to implement the theory proposed in this thesis. This experimental setup is already being built at the laboratório de óptica quântica (LOQ) of UFF, in Niterói city, but the final results aren't obtained until the moment of this thesis writing. The complete version of the setup is summarized in Fig. 65. In this section, our goal is to explain each part of this setup and describe some important concepts of the experimentalist approach.

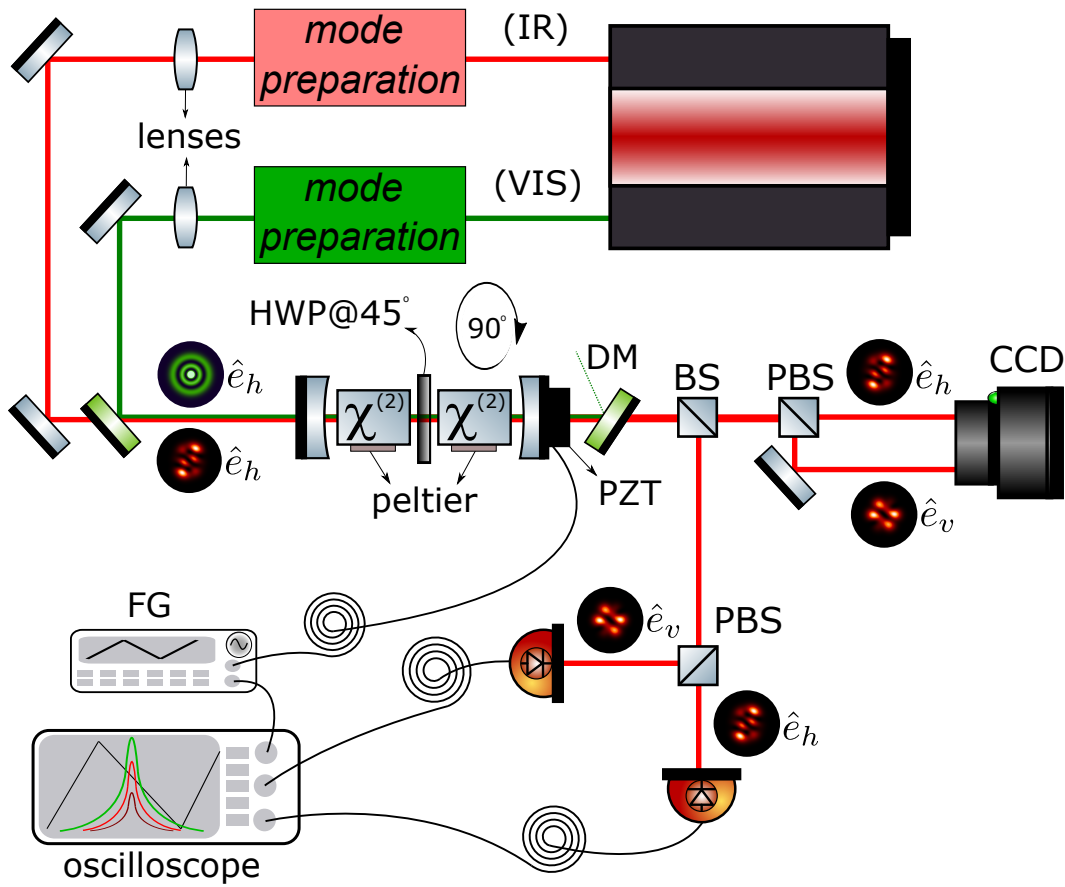


Figure 65 – Basic experimental setup built at LOQ-UFF to investigate OAM symmetry.

In our lab, we are utilizing a Nd:YAG laser² ($\lambda = 1064 \text{ nm}$) with a doubling crystal inside of it. The nonlinear crystal produces, therefore, laser at $\lambda = 532 \text{ nm}$. Since most laser transverse structures are in a Gaussian mode, we must utilize some device in order to structure the light. The device we are utilizing to produce such structures is the SLM, briefly presented in chapter 1. The SLM is represented in the *mode preparation* box, for both wavelength, in our setup.

The next step is the incidence of the modes in the OPO cavity. As previously discussed, the cavity geometry imposes the Rayleigh length of the intracavity beam, according to Equation (3.37). To achieve this condition we must measure the beam waist. This can be done with the "knife method" presented with more details in appendix C. Essentially, by slicing the laser beam in the transverse direction we can measure the beam waist, as well as its position in the longitudinal position. The proper waist value can be achieved using regular

² InnoLight GmbH laser, Diabolo product line.

spherical lenses. It is important to remember that we are impinging two different wavelengths ($\lambda = 1064 \text{ nm}$ and $\lambda = 532 \text{ nm}$) in the OPO cavity. Since the Rayleigh length is $z_R = \pi\omega_0^2/\lambda$ we must guarantee that the beam waist for the Infrared light is $\omega_{0_{1064}} = \sqrt{2}\omega_{0_{532}}$ in order to have the same z_R for both wavelengths and, therefore, stable oscillation.

Once we have the right waists values we can start to monitor the resonance peaks or Airy function, as we previously theoretically discussed. To do so, we must plug in the output mirror a Piezoelectric (PZT) ceramic. This ceramic expands in a controlled manner when receiving an electrical voltage signal. This expansions movement allows us to go through lots of FSR and, therefore, monitor the resonance peaks through the diode detectors plugged in the oscilloscope, as illustrated in our setup. Usually, we apply a ramp signal in the PZT produced by a function generator, which can be monitored in an oscilloscope, as we show in our setup. The green light coming from the cavity can be filtered by a dichroic mirror (DM)

Once we start observing the Airy peaks in the oscilloscope we can make a more refined alignment by moving the cavity mirrors and the mirrors before the OPO cavity. An experimental example of a alignment cavity is shown in the top part of Fig.67, which is the resonance peak of the injected signal mode with a Gaussian transverse structure. At this beginning stage, we recommend, for simplicity, starting using a one crystal configuration with a Gaussian mode before structuring the laser beam.

Our one crystal OPO is in a semi monolithic configuration, according to Fig.66. The input face of the crystal is coated to act as the OPO input coupler (HR at 1064 nm and $R = 92\%$ at 532 nm), while the other face is AR coated to both operation wavelengths. The concave mirror is mounted on a PZT and plays the role of the output coupler (HR at 532 nm and $R = 95\%$ at 1064 nm). The OPO is set in a near-concentric configuration, with a Rayleigh length $z_R = 12 \text{ mm}$. Its measured oscillation threshold is typically around 40 mW. The measured finesse of the OPO cavity was 20 for the pump and 100 for the down-converted modes.

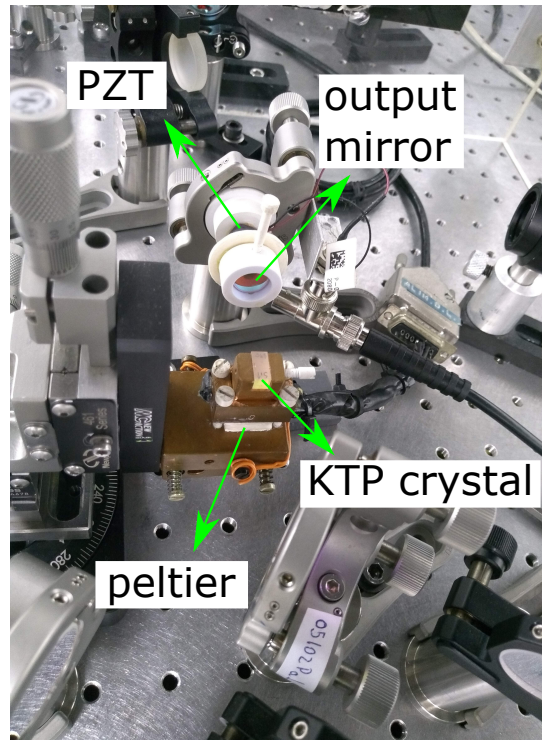


Figure 66 – Semi monolithic OPO. The input face of the crystal is coated to act as the OPO input coupler (HR at 1064 nm and $R = 92\%$ at 532 nm). The concave mirror (HR at 532 nm and $R = 95\%$ at 1064 nm) is mounted on a PZT.

After achieving a good alignment with a Gaussian mode we can start trying to implement the OPA process. The OPA process occurs when we guarantee the triple resonance ($\Delta_p = \Delta_s = \Delta_i = 0$), which means that the Airy peaks for the 3 modes occur in the same positions. The positions of the pump Airy peaks relative to those of signal and idler can be adjusted by controlling the crystal temperature with a peltier, illustrated in Fig.66. At this point, it might be useful to keep the environment quiet and calm in order to guarantee a stable crystal temperature.³

³ Tip: make sure every lab colleague went home and you are alone.

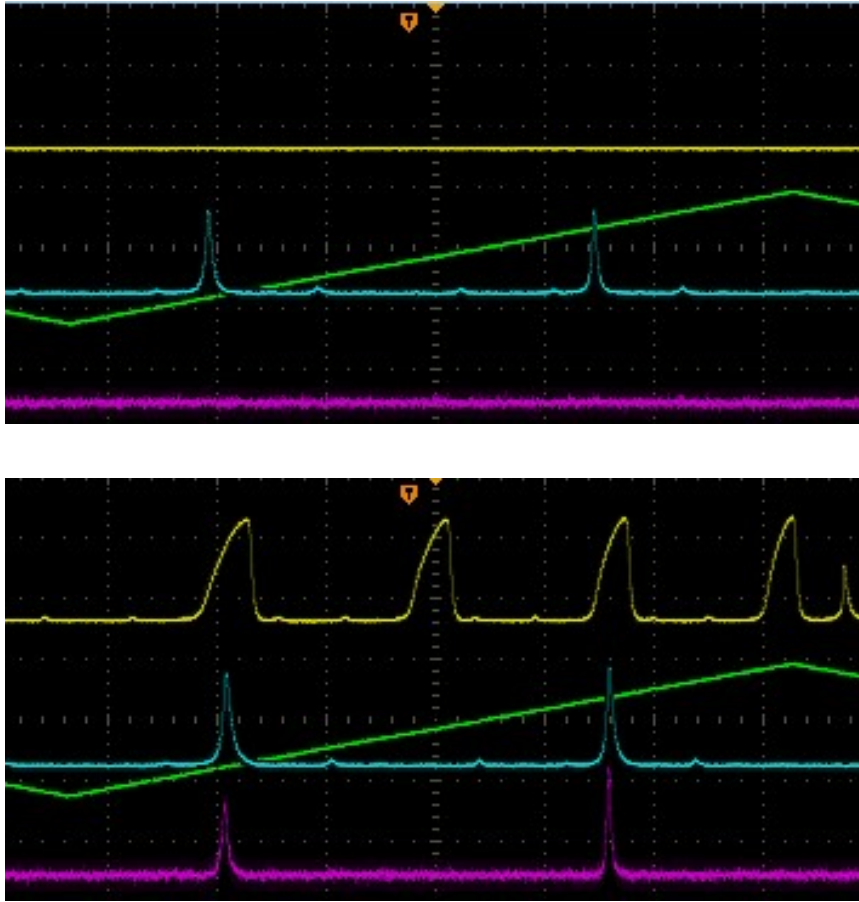


Figure 67 – OPA process for Gaussian modes using one crystal. At the top, we have the Airy peaks for the injected mode (Blue) which will be amplified at signal mode. Once we match the resonance peaks, by controlling crystal temperature, for pump (Yellow), signal (Blue) and the stimulated idler (Purple) we have OPA process (bottom).

After dominating the OPA process with Gaussian modes we can finally start to implement the process with structured light. Let's recall that we have already implemented it for first-order modes [26]. Our goal is to implement the OPA with superior order modes and, therefore, explore the OAM symmetry proposed in this thesis. Let's recall that for superior order modes the astigmatism effect, which is related to the Gouy phase (2.14), is more evident. This optical aberration, however, can be compensated with a second rotated crystal placed in front of the first one.

The two crystal setup built at LOQ is shown in Fig.68. As we can see, we are utilizing an HWP at 45° placed between the crystals. This last one is placed to change the horizontal polarization (extraordinary wave) to vertical polarization

(ordinary wave), and vice-versa. As we have discussed, the ordinary wave suffers astigmatism when passing through the first crystal, but when its polarization is changed and passes through the second crystal rotated crystal we can correct astigmatism. This second rotated crystal was proposed in [52, 53].

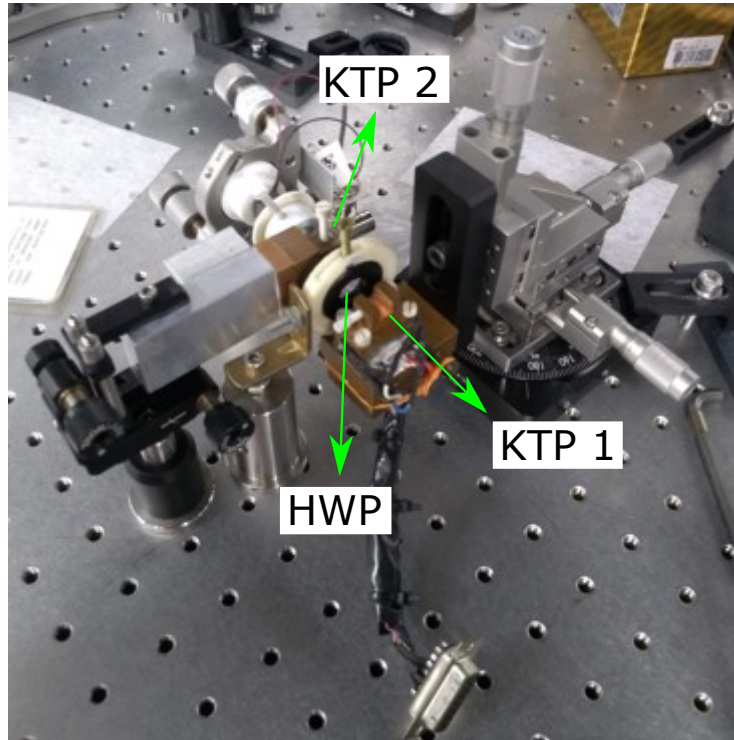


Figure 68 – Two crystals semi monolithic OPO. Same coatings as the previous setup in Fig.66 for the "KTP 1" and output mirror. The "KTP 2" is coated AR for both wavelengths, as well as the HWP.

In Fig.69 we show an experimental example of astigmatism correction for first-order LG mode ψ^{+10} . The experimental procedure is to inject a seed mode with linear diagonal polarization (45° in relation to the fast axis of the HWP). The horizontal component of this beam is the extraordinary wave and suffers no astigmatism (left top part of Fig.69) and will give rise to the amplified signal mode. On the other hand, the vertical component is the ordinary wave and suffer astigmatism as illustrated on the right top part of the Fig.69. As we might expect, this last one will be the polarization that the stimulated idler mode will occupy so correcting the astigmatism of this wave is a good trial to implement the correction of the stimulated mode. As we already mention for superior order modes this correction is more challenging and we are still working on this task optimistically.

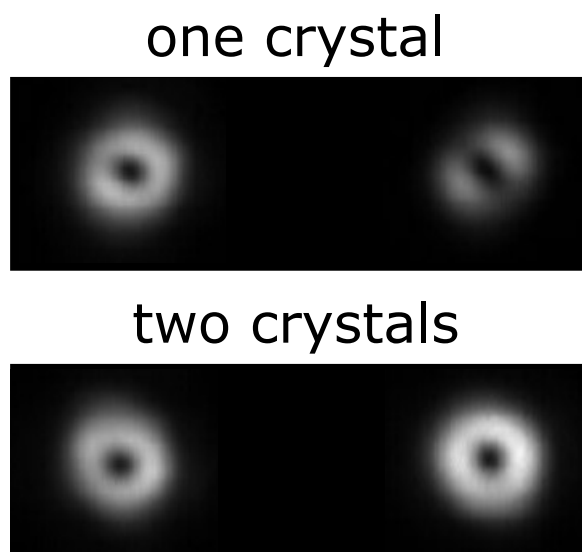


Figure 69 – Two crystals OPO configuration for astigmatism correction for first-order LG mode ψ^{+10} injection. On the right side, we have the ordinary polarization which will be occupied by the stimulated idler mode. This last one can have its astigmatism corrected by placing a second rotated crystal (right bottom part). The signal mode, at extraordinary polarization, will not suffer any optical aberration, as illustrated on the left side of both configurations.

5 Closing Remarks

The main purpose of this thesis is not only to explain in detail our contribution to the literature [25] but also to make a reader non-specialist with the theme understand the basics of our theory. This thesis contribution is the field of structured light in a device called optical parametric oscillator (OPO). We developed a theory studying interesting orbital angular momentum (OAM) symmetry properties between the down-converted beams produced by the OPO under injection, which gives rise to an optical parametric amplification process.

We show that the Poincaré sphere symmetry, previously demonstrated for first-order spatial modes [51, 26] translates to a multiple Poincaré sphere structure for higher-orders. Each one of these multiple spheres is associated with a two-dimensional subspace defined by a different value of the OAM. Therefore, the symmetry verified by first-order modes is reproduced independently in each subspace of dimension two.

In the first few chapters (2 and 3), we revised the key concepts in order to understand our theory. We began discussing structured light, especially the Laguerre-Gauss modes, which are the modes carrying OAM. We talked about their basic features, as well as how to produce and measure their OAM values. In the third chapter, we reunited the study of nonlinear optics, propagation of light in crystals, and optical cavities. Those topics are the most relevant in order to understand the OPO in the classical regime.

Finally, after discussing the basics of the OPO device, as well as the OAM of light we were capable to start studying the generalized OAM symmetry in OPA process. This was the most important topic of this thesis and was detailed in chapter 4. Besides the theory, we proposed an experiment, which is already being built at Laboratório de Óptica Quântica of UFF.

APPENDIX A – Walk-Off Angle

In this chapter we are going to deduce the equation 3.28 for the walk-off angle. To do so, we are going to use the definition [54]

$$\tan \theta_w = -\frac{1}{n(\theta)} \frac{dn(\theta)}{dt}. \quad (\text{A.1})$$

Let's begin by taking the derivative of 3.26 supposing that $n_y = n_e$ and $n_x = n_o$:

$$\frac{d}{d\theta} \left(\frac{1}{n^2(\theta)} \right) = \frac{-2}{n^3(\theta)} \frac{dn(\theta)}{d\theta} = \frac{d}{d\theta} \left(\frac{\sin^2 \theta}{n_e^2} + \frac{\cos^2 \theta}{n_o^2} \right) \quad (\text{A.2})$$

$$\frac{dn(\theta)}{d\theta} = -\frac{n^3(\theta)}{2} \frac{d}{d\theta} \left(\frac{\sin^2 \theta}{n_e^2} + \frac{\cos^2 \theta}{n_o^2} \right) \quad (\text{A.3})$$

$$= n^3(\theta) \left(\frac{1}{n_o^2} - \frac{1}{n_e^2} \right) \sin \theta \cos \theta. \quad (\text{A.4})$$

Let's replace A.4 in the definition A.1. For simplicity, we are going to use θ ($n(\theta) = n$):

$$\tan \theta_w = -\frac{1}{n} \frac{dn}{d\theta} = -n \left(\frac{\sin^2 \theta}{n_e^2} + \frac{\cos^2 \theta}{n_o^2} \right) \left(\frac{1}{n_o^2} - \frac{1}{n_e^2} \right) n^3 \sin \theta \cos \theta \quad (\text{A.5})$$

$$= -n^4 \left(\frac{\sin^2 \theta}{n_e^2} + \frac{\cos^2 \theta}{n_o^2} \right) \left(\frac{1}{n_o^2} - \frac{1}{n_e^2} \right) \sin \theta \cos \theta \quad (\text{A.6})$$

$$= -n^4 \left(\frac{n_o^2 \sin^2 \theta + n_e^2 \cos^2 \theta}{n_o^2 n_e^2} \right) \left(\frac{n_e^2 - n_o^2}{n_o^2 n_e^2} \right) \sin \theta \cos \theta. \quad (\text{A.7})$$

From 3.26, we can get $n^4 = \left[\frac{n_o^2 n_e^2}{n_o^2 \sin^2 \theta + n_e^2 \cos^2 \theta} \right]^2$. Replacing this last relation in A.7 we can obtain:

$$\tan \theta_w = \left[\frac{(n_o^2 - n_e^2) \sin \theta \cos \theta}{n_o^2 \sin^2 \theta + n_e^2 \cos^2 \theta} \right]. \quad (\text{A.8})$$

This last result can be used in the trigonometric relation $\tan^2 \theta_w + 1 = \sec^2 \theta_w$:

$$\sec^2 \theta_w = \frac{(n_o^2 - n_e^2)^2 \sin^2 \theta \cos^2 \theta + (n_o^2 \sin^2 \theta + n_e^2 \cos^2 \theta)^2}{(n_o^2 \sin^2 \theta + n_e^2 \cos^2 \theta)^2}, \quad (\text{A.9})$$

Where we can divide on the right-side of A.9 by n_o^2 and use that $\gamma = n_e/n_o$:

$$\sec^2 \theta_w = \frac{(1 - \gamma^2)^2 \sin^2 \theta \cos^2 \theta + (\sin^2 \theta + \gamma^2 \cos^2 \theta)^2}{(\sin^2 \theta + \gamma^2 \cos^2 \theta)^2}, \quad (\text{A.10})$$

$$\sec^2 \theta_w = \frac{(1 + \gamma^4 - 2\gamma^2) \sin^2 \theta \cos^2 \theta + \sin^4 \theta + \gamma^4 \cos^4 \theta + 2\gamma^2 \sin^2 \theta \cos^2 \theta}{(\sin^2 \theta + \gamma^2 \cos^2 \theta)^2} \quad (\text{A.11})$$

$$\frac{1}{\cos^2 \theta_w} = \frac{(1 + \gamma^4) \sin^2 \theta \cos^2 \theta + \sin^4 \theta + \gamma^4 \cos^4 \theta}{(\sin^2 \theta + \gamma^2 \cos^2 \theta)^2} \quad (\text{A.12})$$

$$\frac{1}{\cos^2 \theta_w} = \frac{\sin^2 \theta (\sin^2 \theta + \cos^2 \theta) + \gamma^4 \cos^2 \theta (\sin^2 \theta + \cos^2 \theta)}{(\sin^2 \theta + \gamma^2 \cos^2 \theta)^2} \quad (\text{A.13})$$

$$\frac{1}{\cos^2 \theta_w} = \frac{\sin^2 \theta + \gamma^4 \cos^2 \theta}{(\sin^2 \theta + \gamma^2 \cos^2 \theta)^2}, \quad (\text{A.14})$$

Where we finally can obtain:

$$\cos \theta_w = \frac{\sin^2 \theta + \gamma^2 \cos^2 \theta}{\sqrt{\sin^2 \theta + \gamma^4 \cos^2 \theta}} \quad (\text{A.15})$$

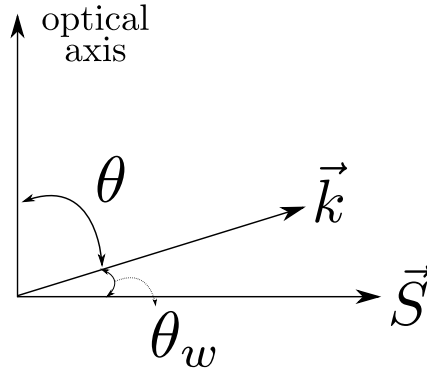


Figure 70 – Pictorial representation of walk-off angle θ_w .

APPENDIX B – Transmitted Intensity and Finesse

In this appendix we are going to demonstrate how to obtain the results 3.32 and 3.34 for the transmitted intensity of a resonator as well of it's finesse, respectively. Let's begin by taking the square modulus of the transmitted field 3.31 in order to obtain it's intensity I_T :

$$E_T = \frac{t_1 t_2 e^{\frac{i\phi}{2}}}{1 - r_1 r_2 e^{i\phi}} E_I \Rightarrow I_T = \frac{T_1 T_2}{|1 - r_1 r_2 e^{i\phi}|^2} I_I, \quad (\text{B.1})$$

where $t_j^2 = T_j$ ($j = 1, 2$). We can manipulate the denominator $|1 - r_1 r_2 e^{i\phi}|^2$ as:

$$|1 - r_1 r_2 e^{i\phi}|^2 = (1 - r_1 r_2 e^{i\phi})(1 - r_1 r_2 e^{-i\phi}) \quad (\text{B.2})$$

$$= 1 + r_1^2 r_2^2 - 2r_1 r_2 \cos \phi. \quad (\text{B.3})$$

Using the trigonometric relation $\cos \phi = 1 - 2 \sin^2 \frac{\phi}{2}$ we can obtain

$$1 + r_1^2 r_2^2 - 2r_1 r_2 \left(1 - 2 \sin^2 \frac{\phi}{2}\right) = 1 + r_1^2 r_2^2 - 2r_1 r_2 + 4r_1 r_2 \sin^2 \frac{\phi}{2} \quad (\text{B.4})$$

$$= \left(1 - \sqrt{R_1 R_2}\right)^2 + 4\sqrt{R_1 R_2} \sin^2 \frac{\phi}{2}. \quad (\text{B.5})$$

Now replacing this last result in the right-hand side of B.1:

$$I_T = \frac{I_I T_1 T_2}{\left(1 - \sqrt{R_1 R_2}\right)^2 + 4\sqrt{R_1 R_2} \sin^2 \frac{\phi}{2}}, \quad (\text{B.6})$$

which can be re-written as:

$$I_T = \frac{I_I T_1 T_2}{\left(1 - \sqrt{R_1 R_2}\right)^2} \cdot \frac{1}{1 + \zeta \sin^2 \frac{\phi}{2}}, \quad (\text{B.7})$$

the last factor is the Airy function and $\zeta = \frac{4\sqrt{R_1 R_2}}{(1 - \sqrt{R_1 R_2})^2}$.

For the calculation of the finesse (3.34) of an empty resonator let's begin using the definition 3.33 (domain in radians) and the result B.7 in a more "compact" way

$$I_T = I_{max} \cdot \frac{1}{1 + \zeta \sin^2 \frac{\phi}{2}}, \quad (\text{B.8})$$

where $I_{m\acute{a}x} = \frac{I_I T_1 T_2}{(1 - \sqrt{R_1 R_2})^2}$. In order to obtain the linewidth $\delta\nu$ (FWHM) let's calculate $I_T = I_{m\acute{a}x}/2$:

$$\frac{I_{m\acute{a}x}}{2} = I_{m\acute{a}x} \frac{1}{1 + \zeta \sin^2 \frac{\phi_L}{2}} \quad (\text{B.9})$$

$$\zeta \sin^2 \frac{\phi_L}{2} = 1 \quad (\text{B.10})$$

$$\sin \frac{\phi_L}{2} = \frac{1}{\sqrt{\zeta}} \quad (\text{B.11})$$

$$\phi_L = 2 \arcsin \left(\frac{1}{\sqrt{\zeta}} \right), \quad (\text{B.12})$$

by replacing $\zeta = \frac{4\sqrt{R_1 R_2}}{(1 - \sqrt{R_1 R_2})^2}$ we have

$$\phi_L = 2 \arcsin \left(\frac{1 - \sqrt{R_1 R_2}}{2\sqrt[4]{R_1 R_2}} \right) \quad (\text{B.13})$$

$$\phi_L = 2 \arcsin \left(\frac{1 - \sqrt{\rho}}{2\sqrt[4]{\rho}} \right), \quad (\text{B.14})$$

where $\rho = R_1 R_2$ represents the "amount" of light remaining inside the resonator after a round trip. The value ϕ_L represents how far of the resonance we are. This idea is represented on figure 71 below. Finally the finesse can be obtained as

$$F = \frac{2\pi}{2\phi_L}$$

$$F = \frac{2\pi}{2 \arcsin \left(\frac{1 - \sqrt{\rho}}{2\sqrt[4]{\rho}} \right)},$$

$$F = \frac{\pi}{2 \arcsin \left(\frac{1 - \sqrt{\rho}}{2\sqrt[4]{\rho}} \right)}. \quad (\text{B.15})$$

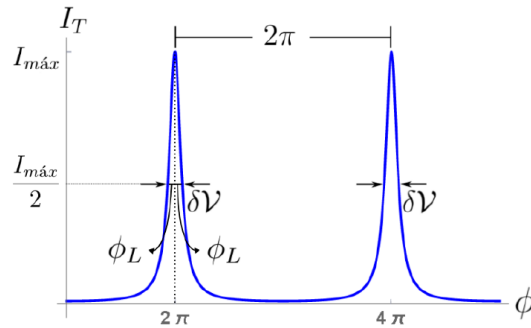


Figure 71 – The value ϕ_L represents how "far" the mode is in relation to the resonance.

APPENDIX C – Beam Waist Characterization

In this chapter, we are going to describe the mathematical details involved in an experimental method used in the lab: *the knife method*. Basically, this method consists in slicing, in a perpendicular direction, a laser beam in order to determine its waist at a given position. The perpendicular slicing distance depends on the transverse structure of the laser. In this chapter, the mathematical description will be related to the Gaussian beam, but for superior order modes is straightforward.

Let's begin calculating the power of a Gaussian mode

$$P = \int_{-\infty}^{+\infty} I(x, y) dA, \quad (\text{C.1})$$

where $I(x, y)$ is the perpendicular intensity of a laser beam and $dA = dx dy$ the element of area. Considering the Gaussian mode (2.8) we have

$$I(x, y) = |\psi^{00}(x, y)|^2 \quad (\text{C.2})$$

$$= \frac{2}{\pi} \frac{1}{\omega^2} e^{-\frac{2\rho^2}{\omega^2}}, \quad (\text{C.3})$$

where $\rho^2 = x^2 + y^2$ and $\omega = \omega(z)$ is the beam waist. Replacing (C.3) in (C.1):

$$P = \frac{2}{\pi} \frac{1}{\omega^2} \int_{-\infty}^{+\infty} \int_{-\infty}^{+x_c} e^{-\frac{2y^2}{\omega^2}} e^{-\frac{2x^2}{\omega^2}} dx dy, \quad (\text{C.4})$$

where x_c is the perpendicular position in x -direction in which we put the knife.

Using the well-known Gaussian integrals we will have

$$P = \frac{2}{\pi} \frac{1}{\omega^2} \int_{-\infty}^{+\infty} e^{-\frac{2y^2}{\omega^2}} dy \int_{-\infty}^{x_c} e^{-\frac{2x^2}{\omega^2}} dx \quad (\text{C.5})$$

$$= \frac{2}{\pi} \frac{1}{\omega^2} \left(\omega \sqrt{\frac{\pi}{2}} \right) \left(\int_{-\infty}^0 e^{-\frac{2x^2}{\omega^2}} dx + \int_0^{x_c} e^{-\frac{2x^2}{\omega^2}} dx \right) \quad (\text{C.6})$$

$$= \frac{2}{\pi} \frac{1}{\omega^2} \left(\omega \sqrt{\frac{\pi}{2}} \right) \left(\frac{\omega}{2} \sqrt{\frac{\pi}{2}} + \int_0^{x_c} e^{-\frac{2x^2}{\omega^2}} dx \right). \quad (\text{C.7})$$

Using the error function in the integral (C.7),

$$\text{erf}(x) = \frac{2}{\sqrt{\pi}} \int_0^x e^{-t^2} dt, \quad (\text{C.8})$$

where we made the variable substitution ($t^2 = 2x^2/w^2$) and rewrite (C.7) as

$$P = \frac{2}{\pi w^2} \left(\frac{\omega}{2} \sqrt{\frac{\pi}{2}} + \frac{\omega}{2} \sqrt{\frac{\pi}{2}} \operatorname{erf} \left(\frac{\sqrt{2}x_c}{w} \right) \right) \quad (\text{C.9})$$

$$P = \frac{1}{2} \left[1 + \operatorname{erf} \left(\frac{\sqrt{2}x_c}{w} \right) \right]. \quad (\text{C.10})$$

With the result (C.10) we can finally know how much we should block the beam in the perpendicular direction. We want to use $x_c = \omega/2$ e $x_c = -\omega/2$:

$$P_{\frac{w}{2}} = \frac{1}{2} \left[1 + \operatorname{erf} \left(\frac{\sqrt{2}\frac{w}{2}}{w} \right) \right] = 0.84 \quad (\text{C.11})$$

$$P_{-\frac{w}{2}} = \frac{1}{2} \left[1 + \operatorname{erf} \left(\frac{-\sqrt{2}\frac{w}{2}}{w} \right) \right] = 0.16 \quad (\text{C.12})$$

where we used $\operatorname{erf}(\sqrt{2}/2) \cong 0.68$ and $\operatorname{erf}(-\sqrt{2}/2) \cong -0.68$. This means that we should block the beam in a perpendicular distance corresponding to 84% of the full power until it gets 16% of it. The knife displacement between $x_c = w/2$ and $x_c = -w/2$ correspond to the beam waist. An experimental apparatus is pictorially, as well as a experimental result, shown in Fig. 72.

The mathematical description for superior modes is analogous. For a first-order LG mode ψ_{LG}^{10} the values are $P_{\frac{w}{2}} = 0.72$ and $P_{-\frac{w}{2}} = 0.28$.

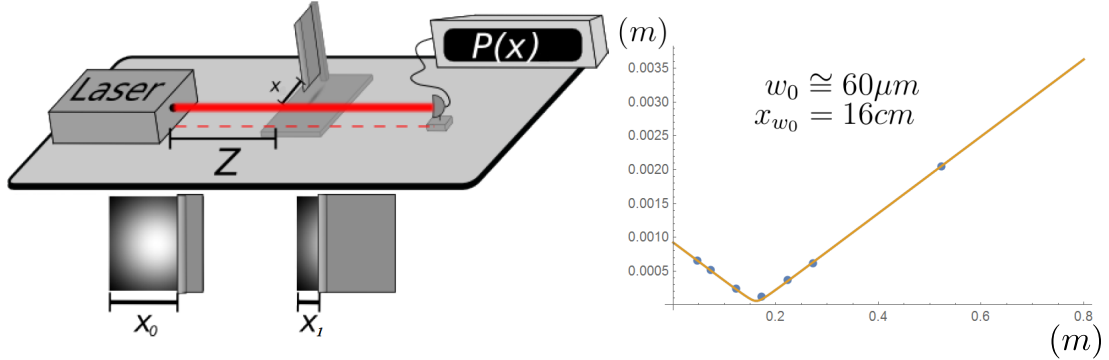


Figure 72 – Knife-method apparatus (left) and experimental result of it (right).

APPENDIX D – Dynamical Equations - Resonator and OPO

In this appendix B we want to show the calculations to obtain the results (3.48), from equation (3.47). To do so we are going to use the approximations $e^{-2\alpha l} \cong 1 - 2\alpha l$ and $r_1 r_2 \cong 1 - \left(\frac{T_1 + T_2}{2}\right)$. Those approximations represent a low loss of the material and low transmission coefficients of the mirrors. Beside that let's replace (3.46a) and (3.46b) in (3.47). Given those considerations we can write (3.47) as:

$$A_p(t + \tau) e^{-i\omega t} e^{-i\omega\tau} = A_p(t) e^{-i\omega t} \left[1 - \left(\frac{T_1 + T_2}{2}\right) \right] (1 - 2\alpha l) + A_{in}(t + \tau) e^{-i\omega t} e^{-i\omega\tau}$$

$$A_p(t + \tau) = A_p(t) e^{i\omega\tau} \left[1 - \left(\frac{T_1 + T_2}{2}\right) \right] (1 - 2\alpha l) + t_1 A_{in}(t + \tau). \quad (\text{D.1})$$

In resonance we have $\omega\tau = 2m\pi$. However is reasonable to consider a detuning of $\Delta\tau = (\omega - \omega_m)\tau$. In that case we can write $\omega\tau = 2m\pi + \Delta\tau$, which allow us to get $e^{i\omega\tau} = e^{i(2m\pi) + i\Delta\tau} \cong 1 + i\Delta\tau$, where we considered the detuning $\Delta\tau$ to be small. Given those considerations we have:

$$A_p(t + \tau) = A_p(t) (1 + i\Delta\tau) \left[1 - \left(\frac{T_1 + T_2}{2}\right) \right] (1 - 2\alpha l) + t_1 A_{in}(t + \tau),$$

where we can neglect a few terms that come from the product and assume that $A_{in}(t + \tau) = A_{in}(t)$ because in a round trip time τ the envelope $A(t)$ is almost unchanged. Therefore:

$$A_p(t + \tau) = A_p(t) - (\tau\gamma - i\Delta\tau) A_p(t) + t_1 A_{in}(t), \quad (\text{D.2})$$

onde $\gamma = \frac{2\alpha l}{\tau} + \frac{T_1 + T_2}{2\tau}$. The next step is to divide both sides of (D.2) by τ and use the coarse grain approximation

$$\frac{dA}{dt} \cong \frac{A(t + \tau) - A(t)}{\tau}. \quad (\text{D.3})$$

By doing so we can obtain the result (3.48) where we are not writing the indice p anymore:

$$\frac{dA(t)}{dt} \cong -(\gamma - i\Delta) A(t) + \frac{\sqrt{T_1}}{\tau} A_{in}(t). \quad (\text{D.4})$$

Now our goal is show the steps to obtain the OPO equations ((3.50a), (3.50b) e (3.50c)). Let 's begin assuming that after a double passage on the crystal we can can write the electric field envelope as

$$A_j'(2l) \cong A_j(0) + 2l \frac{\partial A_j}{\partial z}, \quad (\text{D.5})$$

($j = p, s, i$) where the terms on right-hand side $\frac{\partial A_j}{\partial z}$ are the nonlinear equations discussed on chapter 2. In the OPO we have three waves (pump, signal, idler) so:

$$\frac{\partial A_p}{\partial z} = - \frac{i\chi\omega_p}{2n_p c} A_s A_i, \quad (\text{D.6})$$

$$\frac{\partial A_s}{\partial z} = \frac{i\chi\omega_s}{2n_s c} A_p A_i^*, \quad (\text{D.7})$$

$$\frac{\partial A_i}{\partial z} = \frac{i\chi\omega_i}{2n_i c} A_p A_s^*. \quad (\text{D.8})$$

Now let 's substitute the above results in 3.49:

$$A_p'(2l) = A_p(0) - \frac{i\chi\omega_p}{2n_p c} A_s A_i, \quad (\text{D.9})$$

$$A_s'(2l) = A_s(0) + \frac{i\chi\omega_s}{2n_s c} A_p A_i^*, \quad (\text{D.10})$$

$$A_i'(2l) = A_i(0) + \frac{i\chi\omega_i}{2n_i c} A_p A_s^*. \quad (\text{D.11})$$

The fields after a double passage on crystal $A_j'(2l)$ ($j = p, s, i$) can be compared to $A_p(t + \tau)$ ((D.2)) since the round trip time is equivalently to a double passage on the crystal. The idea is to map the equations (D.9), (D.10) and (D.11) in D.2. So we have:

$$\frac{dA_p}{dt} \cong -(\gamma_p - i\Delta_p) - \frac{i\chi\omega_p l}{n_p c} A_s A_i + \frac{\sqrt{T_{1p}}}{\tau} A_{pin}, \quad (\text{D.12})$$

$$\frac{dA_s}{dt} \cong -(\gamma_s - i\Delta_s) + \frac{i\chi\omega_s l}{n_s c} A_p A_i^* + \frac{\sqrt{T_{1s}}}{\tau} A_{sin}, \quad (\text{D.13})$$

$$\frac{dA_i}{dt} \cong -(\gamma_i - i\Delta_i) + \frac{i\chi\omega_i l}{n_i c} A_p A_s^* + \frac{\sqrt{T_{1i}}}{\tau} A_{iin}, \quad (\text{D.14})$$

where we have used the coarse grain approximation (3.49). Finally, by making the substitution shown in chapter 2 we can obtain:

$$\dot{\alpha}_p = (-\gamma_p + i\Delta_p) + i\chi\alpha_s\alpha_i + \eta_p\alpha_{pin}; \quad (\text{D.15a})$$

$$\dot{\alpha}_s = (-\gamma_s + i\Delta_s) + i\chi\alpha_p\alpha_i^* + \eta_s\alpha_{sin}; \quad (\text{D.15b})$$

$$\dot{\alpha}_i = (-\gamma_i + i\Delta_i) + i\chi\alpha_p\alpha_s^* + \eta_i\alpha_{iin}. \quad (\text{D.15c})$$

Bibliography

- 1 MAIMAN, T. H. et al. Stimulated optical radiation in ruby. 1960.
- 2 FRANKEN, e. P. et al. Generation of optical harmonics. *Physical Review Letters*, APS, v. 7, n. 4, p. 118, 1961.
- 3 LOUISELL, W.; YARIV, A.; SIEGMAN, A. Quantum fluctuations and noise in parametric processes. i. *Physical Review*, APS, v. 124, n. 6, p. 1646, 1961.
- 4 BURNHAM, D. C.; WEINBERG, D. L. Observation of simultaneity in parametric production of optical photon pairs. *Physical Review Letters*, APS, v. 25, n. 2, p. 84, 1970.
- 5 COUTEAU, C. Spontaneous parametric down-conversion. *Contemporary Physics*, Taylor & Francis, v. 59, n. 3, p. 291–304, 2018.
- 6 GIORDMAINE, J. A.; MILLER, R. C. Tunable coherent parametric oscillation in linb o 3 at optical frequencies. *Physical Review Letters*, APS, v. 14, n. 24, p. 973, 1965.
- 7 KWIAT, P. G. Hyper-entangled states. *Journal of Modern Optics*, Taylor & Francis, v. 44, n. 11-12, p. 2173–2184, 1997. Disponível em: <<https://www.tandfonline.com/doi/abs/10.1080/09500349708231877>>.
- 8 MONKEN, C. H.; RIBEIRO, P. H. S.; PÁDUA, S. Transfer of angular spectrum and image formation in spontaneous parametric down-conversion. *Phys. Rev. A*, American Physical Society, v. 57, p. 3123–3126, Apr 1998. Disponível em: <<https://link.aps.org/doi/10.1103/PhysRevA.57.3123>>.
- 9 SANTOS, M. F. et al. Measurement of the degree of polarization entanglement through position interference. *Phys. Rev. A*, American Physical Society, v. 64, p. 023804, Jul 2001. Disponível em: <<https://link.aps.org/doi/10.1103/PhysRevA.64.023804>>.
- 10 BOWEN, W. P. et al. Experimental investigation of continuous-variable quantum teleportation. *Phys. Rev. A*, American Physical Society, v. 67, p. 032302, Mar 2003. Disponível em: <<https://link.aps.org/doi/10.1103/PhysRevA.67.032302>>.
- 11 TREPS, N. et al. A quantum laser pointer. *Science*, American Association for the Advancement of Science, v. 301, n. 5635, p. 940–943, 2003. ISSN 0036-8075. Disponível em: <<https://science.sciencemag.org/content/301/5635/940>>.
- 12 PYSHER, M. et al. Parallel generation of quadripartite cluster entanglement in the optical frequency comb. *Phys. Rev. Lett.*, American

- Physical Society, v. 107, p. 030505, Jul 2011. Disponível em: <<https://link.aps.org/doi/10.1103/PhysRevLett.107.030505>>.
- 13 CHEN, M.; MENICUCCI, N. C.; PFISTER, O. Experimental realization of multipartite entanglement of 60 modes of a quantum optical frequency comb. *Phys. Rev. Lett.*, American Physical Society, v. 112, p. 120505, Mar 2014. Disponível em: <<https://link.aps.org/doi/10.1103/PhysRevLett.112.120505>>.
- 14 MAIR, A. et al. Entanglement of the orbital angular momentum states of photons. *Nature*, v. 412, n. 6844, p. 313–316, jul. 2001. ISSN 0028-0836. Disponível em: <<http://www.nature.com/doi/10.1038/35085529>>.
- 15 CAETANO, D. P. et al. Conservation of orbital angular momentum in stimulated down-conversion. *Phys. Rev. A*, American Physical Society, v. 66, p. 041801, Oct 2002. Disponível em: <<https://link.aps.org/doi/10.1103/PhysRevA.66.041801>>.
- 16 OLIVEIRA, A. G. de et al. Phase conjugation and mode conversion in stimulated parametric down-conversion with orbital angular momentum: a geometrical interpretation. *Brazilian Journal of Physics*, Springer Nature, v. 49, p. 10, Feb 2019. Disponível em: <<https://doi.org/10.1007/s13538-018-0614-4>>.
- 17 BUONO, W. T. et al. Arbitrary orbital angular momentum addition in second harmonic generation. *New Journal of Physics*, IOP Publishing, v. 16, n. 9, p. 093041, sep 2014. Disponível em: <<https://doi.org/10.1088/1367-2630/16/9/093041>>.
- 18 PEREIRA, L. J. et al. Orbital-angular-momentum mixing in type-ii second-harmonic generation. *Phys. Rev. A*, American Physical Society, v. 96, p. 053856, Nov 2017. Disponível em: <<https://link.aps.org/doi/10.1103/PhysRevA.96.053856>>.
- 19 BUONO, W. T. et al. Polarization-controlled orbital angular momentum switching in nonlinear wave mixing. *Opt. Lett.*, OSA, v. 43, n. 7, p. 1439–1442, Apr 2018. Disponível em: <<http://ol.osa.org/abstract.cfm?URI=ol-43-7-1439>>.
- 20 OFFER, R. F. et al. Gouy phase-matched angular and radial mode conversion in four-wave mixing. *Phys. Rev. A*, American Physical Society, v. 103, p. L021502, Feb 2021. Disponível em: <<https://link.aps.org/doi/10.1103/PhysRevA.103.L021502>>.
- 21 OPPO, G.-L.; BRAMBILLA, M.; LUGIATO, L. A. Formation and evolution of roll patterns in optical parametric oscillators. *Phys. Rev. A*, American Physical Society, v. 49, p. 2028–2032, Mar 1994. Disponível em: <<https://link.aps.org/doi/10.1103/PhysRevA.49.2028>>.
- 22 MARTE, M. et al. Spatial patterns in optical parametric oscillators with spherical mirrors: classical and quantum effects: errata. *Opt.*

- Express*, OSA, v. 3, n. 11, p. 476–476, Nov 1998. Disponível em: <<http://www.opticsexpress.org/abstract.cfm?URI=oe-3-11-476>>.
- 23 SCHWOB, C. et al. Transverse effects and mode couplings in opos. *Applied Physics B*, v. 66, n. 6, p. 685–699, Jun 1998. ISSN 1432-0649. Disponível em: <<https://doi.org/10.1007/s003400050455>>.
- 24 BARROS, R. F.; ALVES, G. B.; KHOURY, A. Z. Gouy-phase effects in the frequency combs of an optical parametric oscillator. *Phys. Rev. A*, American Physical Society, v. 103, p. 023511, Feb 2021. Disponível em: <<https://link.aps.org/doi/10.1103/PhysRevA.103.023511>>.
- 25 RODRIGUES, R. B. et al. Generalized orbital angular momentum symmetry in parametric amplification. *Phys. Rev. A*, American Physical Society, v. 105, p. 013510, Jan 2022. Disponível em: <<https://link.aps.org/doi/10.1103/PhysRevA.105.013510>>.
- 26 RODRIGUES, R. et al. Orbital angular momentum symmetry in a driven optical parametric oscillator. *Optics Letters*, Optical Society of America, v. 43, n. 11, p. 2486–2489, 2018.
- 27 SANTOS, B. C. C. dos. *Dinâmica de vórtices em osciladores paramétricos ópticos*. Dissertação (Mestrado) — Universidade Federal Fluminense, Brazil, 2004.
- 28 ALLEN, L.; PADGETT, M.; BABIKER, M. Iv the orbital angular momentum of light. *Progress in optics*, Elsevier, v. 39, p. 291–372, 1999.
- 29 WILLNER, A. E. et al. Optical communications using orbital angular momentum beams. *Advances in Optics and Photonics*, Optical Society of America, v. 7, n. 1, p. 66–106, 2015.
- 30 SOUZA, C. *Aplicações do Momento Angular Orbital da luz Computação e Informação Quântica*. Tese (Doutorado) — PhD thesis, Instituto de Física-UFF, 2010. 20, 2010.
- 31 BEIJERSBERGEN, M. W. et al. Astigmatic laser mode converters and transfer of orbital angular momentum. *Optics Communications*, Elsevier, v. 96, n. 1-3, p. 123–132, 1993.
- 32 JEKRARD, H. Transmission of light through birefringent and optically active media: the poincaré sphere. *JOSA*, Optical Society of America, v. 44, n. 8, p. 634–640, 1954.
- 33 PADGETT, M. J.; COURTIAL, J. Poincaré-sphere equivalent for light beams containing orbital angular momentum. *Optics letters*, Optical Society of America, v. 24, n. 7, p. 430–432, 1999.
- 34 BUONO, W. *Second Harmonic Generation with Optical Phase Vortices*. Tese (Doutorado) — PhD thesis, Instituto de Física-UFF, 2019. 20, 2019.

- 35 VAITY, P.; BANERJI, J.; SINGH, R. Measuring the topological charge of an optical vortex by using a tilted convex lens. *Physics letters a*, Elsevier, v. 377, n. 15, p. 1154/1156, 2013.
- 36 BOYD, R. W. *Nonlinear Optics, Third Edition*. 3rd. ed. [S.l.]: Academic Press, 2008. ISBN 0123694701, 9780123694706.
- 37 A.Z.KHOURY. *CURSO DE ÓPTICA QUÂNTICA*. [S.l.]: UFF, 2017.
- 38 FOWLES, G. *Introduction to Modern Optics*. 2nd. ed. [S.l.]: Longman, 1987.
- 39 YARIV, A. *Quantum electronics*. Wiley, 1989. ISBN 9780471609971. Disponível em: <<https://books.google.com.br/books?id=UTWg1VIkNuMC>>.
- 40 ARAUJO, R. M. de. *Génération et manipulation de peignes de fréquences quantiques multimodes*. Tese (Doutorado) — Université Pierre et Marie Curie-Paris VI, 2012.
- 41 MARTINELLI, M. *Compressão de ruído quântico e efeitos transversos em osciladores paramétricos óticos*. Tese (Doutorado) — Universidade de São Paulo, 2002.
- 42 MARTINELLI, M. et al. Orbital angular momentum exchange in an optical parametric oscillator. *Physical Review A*, APS, v. 70, n. 1, p. 013812, 2004.
- 43 ALVES, G. et al. Conditions for optical parametric oscillation with a structured light pump. *Physical Review A*, APS, v. 98, n. 6, p. 063825, 2018.
- 44 PADGETT, M.; ALLEN, L. Light with a twist in its tail. *Contemporary Physics*, Taylor & Francis, v. 41, n. 5, p. 275–285, 2000.
- 45 MELO, B. et al. Optical trapping in a dark focus. *Physical Review Applied*, APS, v. 14, n. 3, p. 034069, 2020.
- 46 EFRON, U. *Spatial light modulator technology: materials, devices, and applications*. [S.l.]: CRC press, 1994. v. 47.
- 47 SIEGMAN, A. E. Lasers university science books. *Mill Valley, CA*, v. 37, n. 208, p. 169, 1986.
- 48 SCHWOB, C. et al. Transverse effects and mode couplings in opo. *Applied Physics B*, Springer, v. 66, n. 6, p. 685–699, 1998.
- 49 GRIFFITHS, D. J. *Introduction to electrodynamics*. [S.l.]: American Association of Physics Teachers, 2005.
- 50 STOLZENBERGER, R. A. Nonlinear optical properties of flux growth ktiopo 4. *Applied optics*, Optical Society of America, v. 27, n. 18, p. 3883–3886, 1988.

- 51 SANTOS, B. C. dos et al. Phase conjugation and adiabatic mode conversion in a driven optical parametric oscillator with orbital angular momentum. *Physical Review A*, APS, v. 76, n. 5, p. 053821, 2007.
- 52 LIU, K. et al. Experimental generation of continuous-variable hyperentanglement in an optical parametric oscillator. *Phys. Rev. Lett.*, American Physical Society, v. 113, p. 170501, Oct 2014. Disponível em: <<https://link.aps.org/doi/10.1103/PhysRevLett.113.170501>>.
- 53 CAI, C. et al. Experimental characterization of continuous-variable orbital angular momentum entanglement using stokes-operator basis. *Opt. Express*, OSA, v. 26, n. 5, p. 5724–5732, Mar 2018. Disponível em: <<http://www.opticsexpress.org/abstract.cfm?URI=oe-26-5-5724>>.
- 54 PASCHOTTA, D. R. *RP Photonics Consulting GmbH*. 2004. <https://www.rp-photonics.com/spatial_walk_off.html>. [Online; accessed 04-FEV-2018].